IDENTIFICATION OF SOUND TRANSMISSION PATHS WITHIN A HERMETIC RECIPROCATING REFRIGERATION COMPRESSOR VIA MULTIPLE-INPUT/SINGLE-OUTPUT MODELING

by

Matthew Ashby Craun

Thesis submitted to the Faculty of the
Virginia Polytechnic Institute and State University
in partial fulfillment of the requirements for the degree of

MASTER OF SCIENCE

in

Mechanical Engineering

APPROVED:

Larry D. Mitchell
L. D. Mitchell, Chairman

R G Mitchiner
R. G. Mitchiner

C. E Knight
C. E. Knight

May, 1994
Blacksburg, Virginia

IDENTIFICATION OF SOUND TRANSMISSION PATHS WITHIN A HERMETIC RECIPROCATING REFRIGERATION COMPRESSOR VIA MULTIPLE-INPUT/SINGLE-OUTPUT MODELING

by

Matthew A. Craun

Committee Chairman: L. D. Mitchell
Mechanical Engineering

(ABSTRACT)

Through the use of multiple-input/single-output (MISO) modeling, the propagation paths of sound within a reciprocating refrigeration compressor have been investigated and ranked. By investigating the nature of sound propagation within reciprocating compressors, it is hoped that compressor manufacturers can effectively formulate strategies for compressor sound reduction.

From experimental data of compressor far-field sound output, suspension spring forces, and internal pressure fluctuations, a MISO model has been developed. From this model, the importance of the suspension system to the compressor far-field sound spectrum has been identified. In the frequency range above 800 Hz, forces passing through the suspension system appear to be the dominant contributor to shell excitation and sound radiation.

Based upon this finding, it is recommended that modified suspension systems be considered as an avenue for compressor sound reduction efforts in the future.

ACKNOWLEDGMENTS

The author would like to acknowledge the financial support provided to this project by Bristol Compressors, the Center for Innovative Technology, and Virginia Tech.

For technical support and guidance, I would like to acknowledge Professor L. D. Mitchell. In addition, I would like to thank Professors R. G. Mitchiner and C. E. Knight of Virginia Tech for their technical assistance.

For invaluable advice and assistance, I would like to thank David Gilliam of Bristol Compressors. In addition, I would like to thank Ted Boyd and David Sheets of Bristol Compressors for their technical support

For further technical help, I would like to thank Billy Shepherd and David Montgomery of Virginia Tech.

For personal support and assistance, I would like to thank my research peers on this project: Jay Rose, Ramakant Arcot, and Anand Ramani.

For personal support, I would like to thank Mary and Gunther Craun, Michael and Raven Craun, Karl Tu, and Shirley Liu.

TABLE OF CONTENTS

LIST OF FIGURES

LIST OF TABLES

NOMENCLATURE

Symbol	Definition
G_{yy}	One-Sided Auto Spectrum of y
$G_{yy.1}$	Auto Spectrum of y with Effects Input One Removed
G_{xy}	Cross Spectrum Between x and y
H_x	Linear Frequency Response Function (FRF) of x
$x(t)$	Input as a Function of Time
X	Frequency Transform of $x(t)$
$x_{2.1}$	Conditioned Input
$y(t)$	Output as a Function of Time
Y	Frequency Transform of $y(t)$
γ^2_{xy}	Ordinary Coherence between x and y
$\gamma^2_{y:x}$	Multiple Coherence of y due to all x's
$\gamma^2_{xy.z}$	Partial coherence between x and y with effect of z removed
{ }	Vector Quantity
[ ]	Matrix Quantity
*	Complex Conjugate
T	Transpose of Matrix
h	Hermetian Transpose of Matrix

CHAPTER 1.
INTRODUCTION

Consumer demand has dictated the development of reduced-noise products. For many products, the latest challenge for mechanical designers involves the reduction of sound and vibration. One such product is the hermetically sealed refrigeration compressor, present in commercial and residential air-conditioning systems. The desire by manufacturers to provide quieter compressors has made necessary the study of compressor sound transmission paths as part of a total program to understand and minimize compressor sound output.

1.1. PROJECT OVERVIEW

The following thesis is part of a series of studies initiated by the Bristol Compressor Company to more fully understand the phenomenon of sound propagation within refrigeration compressors, more specifically their model H25A reciprocating hermetically sealed model. The H25A project is comprised of several teams, each addressing different aspects of the compressor's dynamic behavior. These teams include an analytical modeling team for constructing a finite element and solid model of the compressor, an experimental modal analysis team for experimentally verifying the compressor mode shapes given by the finite element model, a team to analytically predict the dynamic forces and accelerations of subassemblies within the compressor, and a team for determining the transmission paths of sound within the compressor. From the information gathered by these efforts, understanding of the compressor dynamics can be gained, and through the finite element model design change ideas can be inexpensively implemented in the model to observe their effect.

The work presented in this thesis details the efforts of the sound transmission path study. The goal of this effort is to gather experimental data from an operating Bristol H25A compressor and use it to (a) verify the analytical dynamic model mentioned above, and (b) to construct a multiple-input/single-output model to identify and rank the transmission paths of sound within the compressor. The information presented within this

thesis hopefully will be used to guide redesign efforts towards the important paths of sound propagation within the compressor, and away from redesigns which attack the wrong problems. As will be seen later in this chapter, the complicated geometry and operation of this compressor make it difficult to guess which processes and hardware of the compressor contribute the most to the sound that ultimately reaches the customer's ear.

The remainder of chapter 1 will introduce the Bristol H25A reciprocating hermetically sealed refrigeration compressor and discuss some current theories as to what causes compressors of this type to emit acoustic sound. Chapter 2 introduces the theories of multiple-input/single-output systems, which were used in this study to mathematically investigate the sound sources and propagation paths from experimental data. Chapter 3 extends the basic theories introduced in chapter 2 into the more specific realm of sound source prediction, including some experimental concerns and the results of some earlier applications of these theories to industrial noise reduction problems. Chapter 4 discusses the process of instrumenting the H25A compressor and collecting useful data for the model. Chapter 5 then presents some samples of collected data and the results of the multiple-input/single-output modeling. Finally, chapter 6 summarizes the project by providing conclusion based upon the results gathered, and provides recommendations.

1.2. THE BRISTOL H25A COMPRESSOR

1.2.1. GENERAL DESCRIPTION

The Bristol model H25A compressor is a two-cylinder, reciprocating, hermetically sealed refrigerant compressor used in commercial and residential settings. It provides 61,000 BTU/hr (17.9 kW) cooling capacity, at an efficiency of 11.2 BTU/hr/Watt (3.28 W/W). The version studied here is driven by a 5 HP (3730 W) General Electric three-phase AC electric motor, although single phase versions also exist. Figure 1.1 shows the compressor as viewed from the outside.

Figure 1.2 shows the internal parts of the H25A compressor. Although it is not possible to fully describe every part of the compressor, it is worthwhile to explain some

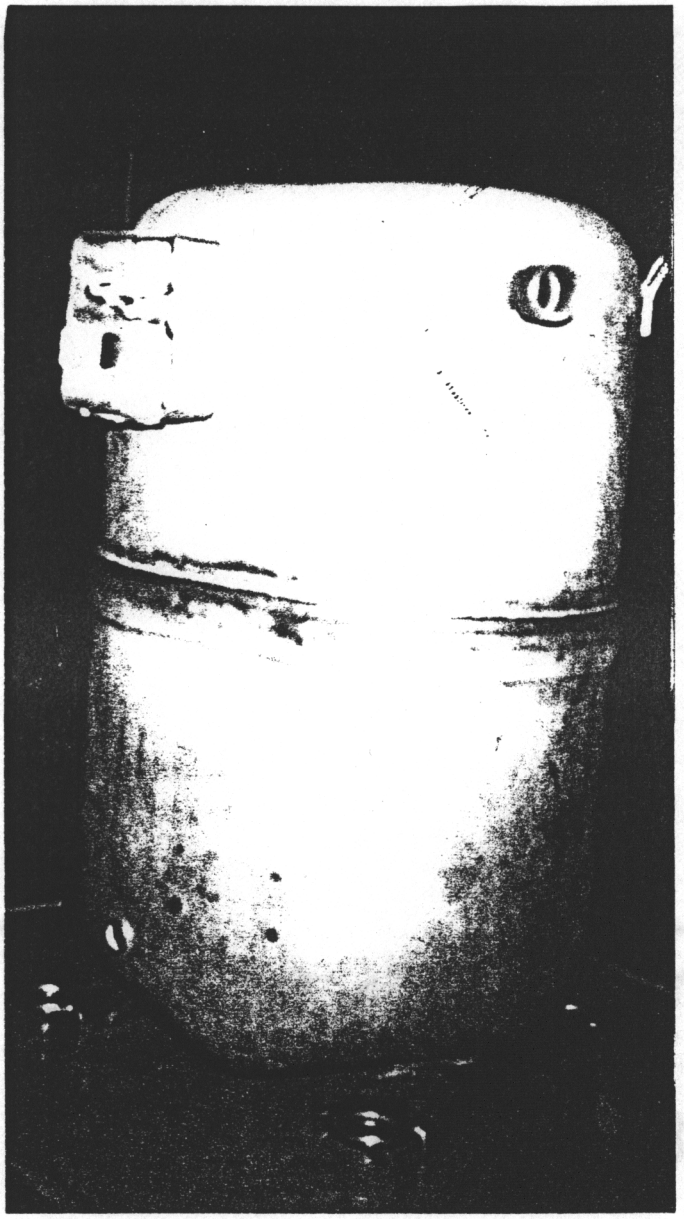

FIGURE 1.1. The Bristol H25A Compressor

1	Compressor Shell
2	Electrical Hook-Up Box
3	Exhaust Tube
4	Suction Tube
5	Muffler
6	Cylinder Head
7	Suspension Springs
8	Crankcase
9	Top Piston & Cylinder
10	Bottom Piston & Cylinder
11	Crankshaft
12	AC Electric Motor
13	Motor Cap

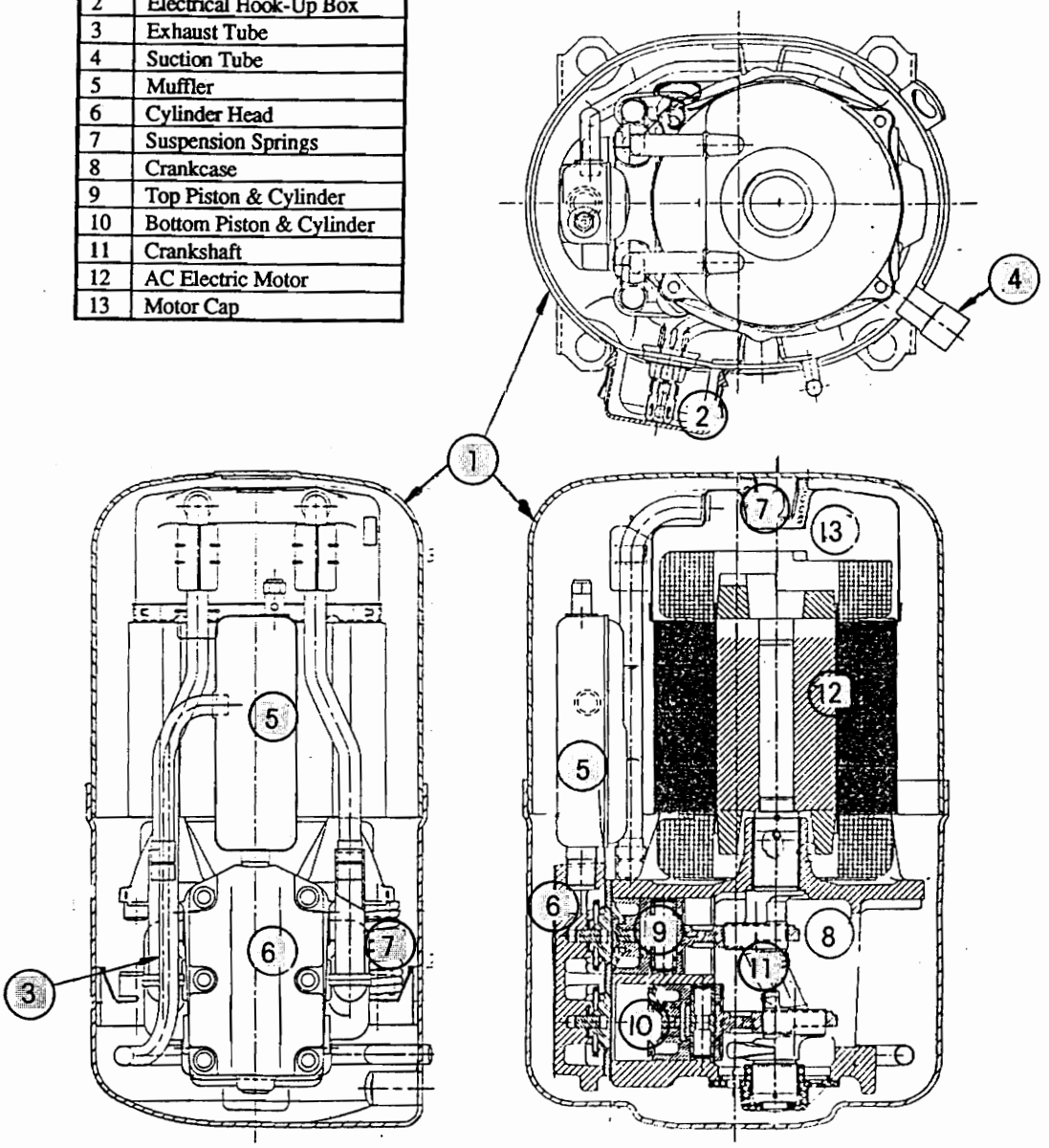

FIGURE 1.2. Internal Components of the Bristol H25A Compressor
(Drawing Courtesy Bristol Compressors)

basic hardware which will be referred to throughout this thesis. The most notable part of this compressor is the shell or housing (1), which is the casing surrounding the internal compressor parts. This part is important to compressor sound output because all sounds heard outside the compressor must ultimately pass through this shell. The shell has an oval shape when viewed from the top, giving rise to the terms "long side" and "short side" to differentiate between the two vertical faces of the compressor. Also, one of the long sides has an electrical connection box (2) and the exhaust tube (3) passing through it, while the other has no external features. This gives rise to the terminology "clean" and "dirty" long sides. Similarly, one of the short sides is "clean", while the other has the suction tube (4) on it. As can be seen in Fig. 1.1, the shell is formed by an upper and lower half, joined together by a weld joint sometimes referred to as the "belt line" weld.

Two tubes pass through this shell to allow for gas flow into and out of the compressor. The short tube at the compressor top is the suction tube (4), which draws in the refrigerant prior to compression. Note that this tube terminates at the compressor shell, thus allowing the incoming gas to circulate within the shell. The exhaust tube (3), also known as the shock-loop tube for its shape, enters the shell at the bottom and connects to a muffler (5) and the compressor cylinder head (6). This tube ports the high pressure exhaust refrigerant to the rest of the air-conditioning system.

Other notable parts include the three suspension springs (7) which support the compressor assembly within the shell. Two of these are located on the lower half of the shell long sides. For the sake of discussion, the "right" and "left" suspensions springs will follow the convention of right and left as viewed in Fig. 1.2. The third suspension spring is located at the shell top and is called the "stabilizer spring". Note that other than the shock-loop tube, these are the only compressor parts which connect the shell to the compressor assembly. The crankcase (8) houses the two cylinders (9), (10), the crankshaft (11) which is driven by the AC motor (12), and the cylinder head (6) which caps the cylinders and contains the exhaust valves. Please see Fig. 1.2 for the relative positions of these parts with one another. Figure 1.2 also points out other compressor parts not described here.

1.2.2. SOUND SOURCES AND PROPAGATION PATHS

Although the goal of this project is identify the major sound propagation paths within the Bristol H25A compressor, there is already some basic understanding of compressor sound output, based upon experience and study. Figure 1.3 is a graphic presented by Price[1] in an earlier study of compressor noise. This graphic conforms to the generally accepted model of compressor sound output as it is understood today.

At the top of the hierarchy of sound generation is the compression process itself; that is, the action of the cylinders compressing and releasing the refrigerant. This compression process is complicated in terms of sound propagation because it causes many effects to occur. These can be divided into pressure fluctuations and mechanical vibrations. The pressure fluctuations are the result of the cyclic nature of the compression process. As the cylinders compress the gas, the pressure within the shell or housing fluctuates dynamically, as does the gas in the shock-loop and suction lines. These fluctuations are rich in harmonic content as will be shown later.

The mechanical vibrations result from the valves opening and shutting, the dynamic forces exerted on the piston face, the rattling of clearances between parts, and the effect of reciprocating masses causing dynamic motion of the compressor sub-assemblies. As seen in Fig. 1.3, these vibrations only have a finite number of paths to reach the compressor shell. These include the shock-loop tube, the suspension springs, and the oil puddle which rests in the lower portion of the compressor.

Whether the acoustic energy emanates from the compression process as a pressure fluctuation or a mechanical vibration, it must ultimately pass through the shell to be heard. Once the shell begins to vibrate, the sound easily finds a path to the ear. The emphasis here is most concerned with what is happening between the compression process and the compressor housing in Fig. 1.3. If the sound propagation paths could be ranked in order of importance to external sound output, the effort of compressor sound reduction could be focused on the major contributors to the compressor sound output.

Based upon the information contained in Fig. 1.3, it was decided in this particular study to investigate the forces passing through the springs, the motion of the shock-loop

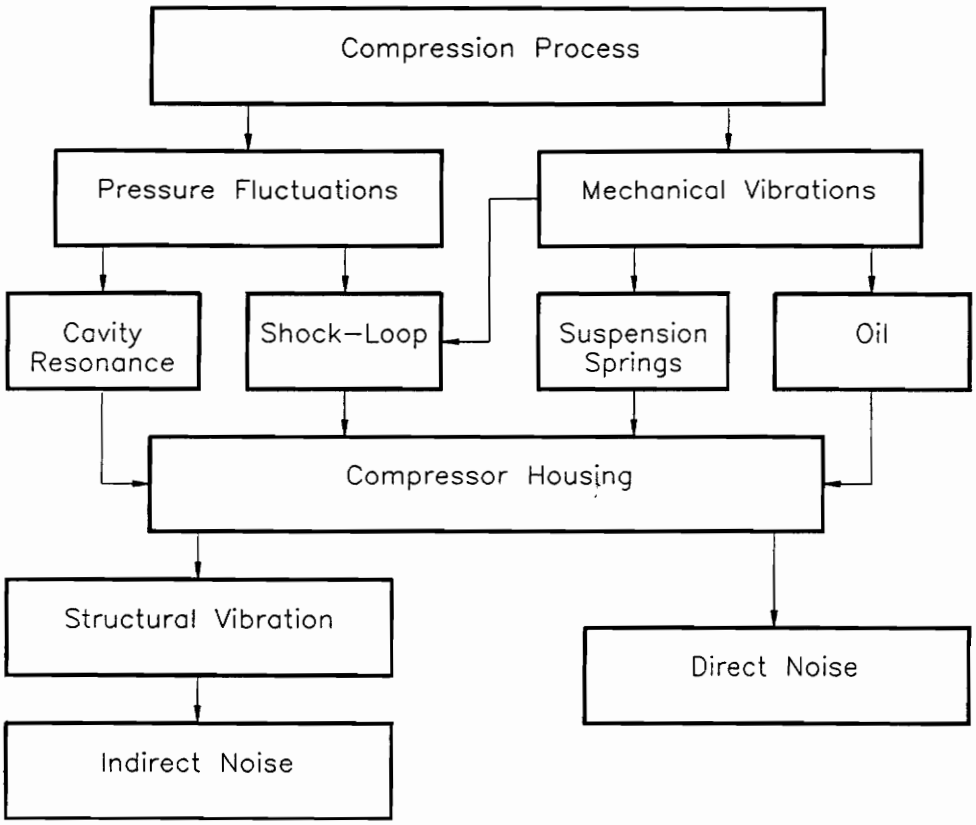

FIGURE 1.3. Model of Reciprocating Compressor Noise (From Price[1])

tube, the pressure fluctuations within the exhaust tube prior to the muffler, the housing cavity pressure fluctuation, and the suction pressure fluctuation. In addition, the cylinder pressure fluctuations and the compressor motion would be measured to provide information to the dynamic modeling team mentioned above. The oil path was not investigated for several reasons. First of all, the shell bottom was not believed to be a major radiating surface of the compressor shell, although the shell bottom does have some active mode shapes[2]. Also, limitations in the maximum number of channels limited the number of transducers which could be installed and monitored. Chapter 4 discusses in depth the process of instrumenting the H25A compressor to measure the effects described here.

Sound studies conducted by Bristol Compressors have characterized the sound output of the H25A compressor, as well as set targets for sound reduction goals. The following information about the H25A sound characteristics were related by David Gilliam of Bristol Compressors. By averaging sound pressure level data from various microphone locations around the compressor, Bristol has determined that the H25A operates at around 77 dBA re 2.9×10^{-9} psi (20×10^{-6} Pa). Although this method of sound level measurement is dependent upon microphone location, these locations have been standardized by Bristol and are useful when comparing different compressor models or certain compressors before and after modification. The microphone locations used by Bristol in their sound pressure level averaging method include microphones 2 ft (.61 m) away from each face as well as microphones positioned at the corners between the compressor faces.

From this sound data, certain frequencies of compressor sound output have been identified as major targets for sound output reduction. The most dominant frequencies present in the Bristol H25A sound spectrum are located between the 1000 Hz and 1600 Hz one-third octave bands. Also of note are contributions around the 250 Hz and 4000 Hz one-third octave bands. Although any sound output reduction of the H25A compressor is desirable, particular interest is paid to these frequencies, especially those between 1000 Hz and 5000 Hz which contribute heavily to the overall A-weighted average of the compressor.

1.3. PREVIOUS RESULTS FROM COMPRESSOR SOUND STUDIES

The literature contains several examples of research done on compressors of this type, including some previous work at Virginia Tech on earlier models of Bristol compressors[3]. Most notable of these is the multiple-input/single-output study of the Bristol H23A compressor conducted by Young[4]. Young's work was the forerunner to the research done here, as it used the method of multiple-input/single-output (MISO) modeling to rank the propagation paths of sound within a similar compressor, the Bristol H23A. It was hoped that the conclusions found on the H23A could help guide the research on the H25A, the current compressor line. In addition, it was hoped that the study presented here could confirm some of the conclusions found by Young, or perhaps supplement the conclusions with new information.

The most notable conclusion of the H23A multiple-input/single-output study was that the spring mechanical path was the dominant sound propagation path, as contrasted to the housing pressure. Among the springs, the top spring was particularly important as it drove a vibrational mode on the top of the compressor which contributed heavily to the overall compressor sound output. Attempts to investigate the shock-loop tube were unsuccessful because the shock-loop data caused problems with the mathematical model, for reasons not entirely understood. Also, it was found that a significant drop in compressor sound output was achieved after instrumentation of the compressor, raising questions about which path was most significantly altered in the instrumentation process[4].

Another important study which was consulted was the work of Price[1]. Price's work was conducted on the Tecumsah AB compressor, used in window-unit air conditioning systems. Through both modeling techniques and experiments, Price postulated that the majority of compressor sound output was the result of one vibration mode of the compressor top and also one side mode. The motion of the compressor top was due, in his opinion, to broad-band excitation by both the suction pressure fluctuation and the top suspension spring. The side mode was attributed to spring path propagation. Attempts to modify the springs to reduce sound output resulted in only partially successful results[1].

The study undertaken here used the results of these studies to guide the process of investigating sound propagation paths within the Bristol H25A compressor. It was hoped that the additional information provided from this work could add to the general understanding of compressor sound propagation, and aid the designer of compressors in the quest for producing quieter products in the future.

CHAPTER 2.
MULTIPLE-INPUT/SINGLE-OUTPUT (MISO) SYSTEMS

This chapter will describe the formulation and solution of the multiple-input/single-output model, which was used as the primary method of ranking the sound propagation paths within the Bristol H25A compressor. Several approaches to the multiple-input problem will be presented and briefly discussed. The following chapter will then describe the limitations and merits of each approach as they relate to noise source identification and the task at hand.

2.1. OVERVIEW OF LITERATURE: MISO THEORY

The derivations and discussion presented here are adapted from a variety of sources available on multiple-input theory. Bendat and Piersol [5] provide an overview of multiple-input theory, along with a rather complete discussion of its signal processing basics. For terminology and basic definitions not given here, this reference should be consulted. Bendat and Piersol present more detail and examples in their *Engineering Application of Correlation and Spectral Analysis* [6] which is taken from a series of Bendat articles [7], [8], [9] that were published prior to reference [6]. Topics covered by Bendat and Piersol here include the development of both single- and multiple-input/output models, optimum frequency response function and conditioned spectrum solutions, computational algorithms, and extensions of multiple-input/output theory into noise-path identification problems.

The material on partial coherence is based on the work of Dodds and Robson [10] who are credited with first presenting this theory. The section presented on the optimum frequency response function approach follows closely the development presented by Trethewey [11], who used this method in his research on forge hammer noise identification. A less detailed discussion of his work can be found in his articles with Evensen [12], [13], and with Evensen and Shapton [14] as well. The information on priority ranking comes from Park and Kim [15], and is the most recent development in multiple-input modeling.

Bernhard and Ufford [16], Price [1], and Lueridan, Roesems, and Otte [17] were consulted for the presentation on virtual coherence/principal component methods. Literature is available on principal components in the time-domain, but since the methods presented here are all frequency-domain procedures, these methods are not presented.

The computational methods presented by Bendat and Piersol [6] are extensions of work initially investigated by Romburg [18]. These methods are not presented here due to the extensive use of IDEAS software in this project precluding the need for writing original computational algorithms. Trethewey [11] also includes a discussion of numerical methods, but for the same reason this is not included here.

2.2. FORMULATION OF THE MISO MODEL

The standard representation of the multiple-input/single-output (MISO) model is shown in Fig. 2.1. This model consists of k inputs $(x_1(t),x_2(t),...,x_k(t))$ passing through k linear frequency response functions (FRF's) denoted by $H_1,H_2,...,H_k$. The outputs of these FRF's $(y_1(t), y_2(t), ...,y_k(t))$ sum with each other to produce the single-output of the model, $y(t)$. In the most general model, an uncorrelated contribution of unknown origin is also included in the summation and can be called the noise input, denoted by $n(t)$.

The traditional method of analysis for MISO systems is frequency-domain based. This convention is especially suitable for stationary, ergodic processes and will be adopted for this discussion. For convenience, all spectra will be considered single sided and a capital letter will be used to denote a function of frequency. For example, Y will be used to describe the Fourier transform of the model output $y(t)$, and G_{yy} will be used to denote the auto spectrum of $y(t)$.

All of the methods of analysis used to describe the MISO model will assume some level of coherence between the inputs, but no coherence between $n(t)$ and any of the inputs or the output. The ordinary coherence between inputs will be assumed somewhere between zero and unity, excluding the cases of zero or total coherence. The case of totally uncorrelated inputs can be solved with the methods presented, but no special effort

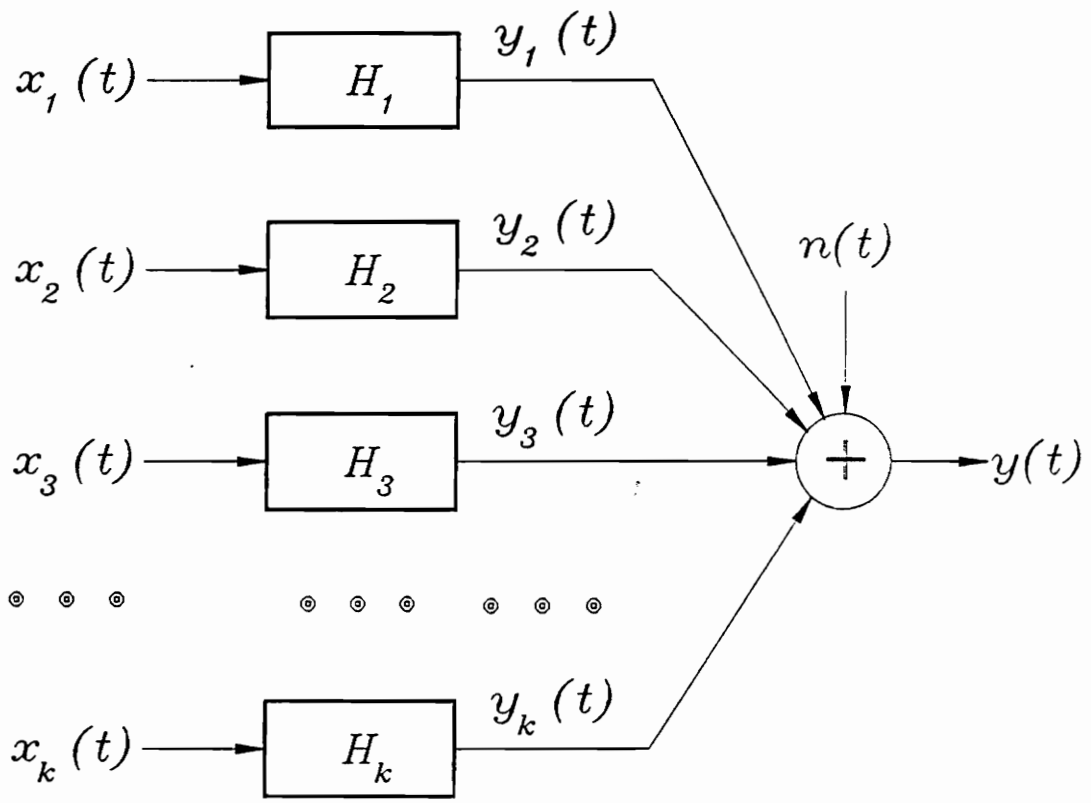

FIGURE 2.1. Multiple-Input/Single-Output (MISO) Model

will be made to point out the special results of such a case due to the rarity of such models in true physical systems. The special case where the coherence function between any two inputs or any input and the output is unity describes a faulty model. This is because the model provides redundant information necessary to describe the output. The number of inputs should be reduced until only partially coherent inputs are present.

2.3. THE OPTIMUM FRF SOLUTION OF THE MISO MODEL

One approach to the MISO model solution is to mathematically solve for the FRF's between each individual input and its corresponding output prior to summation. This is done in the frequency-domain with auto and cross spectral quantities as follows.

2.3.1 BASIC FREQUENCY RESPONSE FORMULATION

Temporarily ignoring the noise term $n(t)$, the time-domain summation of the FRF outputs can be described as

$$y(t)=\sum_{i=1}^{k} y_i(t) \tag{2.1}$$

The frequency-domain equivalent of this is

$$Y=\sum_{i=1}^{k} H_i X_i \tag{2.2}$$

To form an auto spectrum from the frequency-domain output, the output requires multiplication by its complex conjugate Y^*. Also, it must be multiplied by $2/T$ (recall these are one-sided spectra) and the expectation in the limit as T approaches infinity must be taken. Performing these operations yields the output auto spectrum

$$G_{yy} = \sum_{i=1}^{k} H_i G_{yi} \tag{2.3}$$

In a similar fashion, cross spectra between the output and each input can be found. This requires multiplying Eq. (2.2) by $X_i^*(2/T)$, swapping i for j, and taking the expectation in the limit, yielding

$$G_{iy} = \sum_{j=1}^{k} H_j G_{ij} \tag{2.4}$$

Substituting Eq. (2.4) into Eq. (2.3) (note $G_{ij}=G^*_{ji}$) yields the result

$$G_{yy} = \sum_{i=1}^{k}\sum_{j=1}^{k} H_i^* G_{ij} H_j \tag{2.5}$$

Equation (2.5) is very important because it describes the output auto spectrum of the MISO model solely in terms of input spectra and the FRF's between each input and the output. These FRF's can be solved from Eq. (2.4) in real systems because both the G_{yy} term and the G_{ij} terms can be found experimentally through the use of transducers and a machine capable of averaging data in the frequency domain.

The method of solution can better be seen and understood with Eqs. (2.4) and (2.5) in matrix form. To convert these equations, let us define matrices of the known quantities of the MISO model. These will be the FRF and output vectors,

$$\{H\} = \begin{vmatrix} H_1 \\ H_2 \\ . \\ . \\ H_k \end{vmatrix} \qquad \{G_y\} = \begin{vmatrix} G_{1y} \\ G_{2y} \\ . \\ . \\ G_{ky} \end{vmatrix} \tag{2.6}$$

and the input spectral matrix,

$$[G]=\begin{bmatrix} G_{11} & G_{12} & G_{13} & \dots & G_{1k} \\ G_{21} & & & & \cdot \\ \cdot & & & & \cdot \\ \cdot & & & & \cdot \\ G_{k1} & & & & G_{kk} \end{bmatrix} \tag{2.7}$$

With these matrices defined, it is possible to rewrite Eq. (2.4) as

$$\{G_y\} = [G]\{H\} \tag{2.8}$$

and Eq. (2.5) as

$$G_{yy} = \{H^*\}^T [G]\{H\} \tag{2.9}$$

It can now be clearly seen that by solving matrix Eq. (2.8), the FRF vector can be determined. It then follows that all the H blocks depicted in Fig. 2.1 can be accounted for. Then, matrix Eq. (2.9) can be used to generate the output auto spectrum in terms of the known inputs and the computed FRF's.

2.3.2. OPTIMUM FREQUENCY RESPONSE FORMULATION

When a MISO model is used to describe an actual system, it is nearly impossible to account for all effects producing the output $y(t)$ with a finite number of inputs. For this reason, the noise term $n(t)$ is included in the model to account for uncorrelated effects which provide a small contribution to the system output. The frequency-domain description of this noise term is

$$N = Y - \sum_{i=1}^{k} H_i X_i \tag{2.10}$$

The auto spectrum of the noise is found by multiplying the expected value of Eq. (2.10) times its complex conjugate by $2/T$ and is

$$G_{nn} = G_{yy} - \sum_{i=1}^{k} H_i G_{yi} - \sum_{j=1}^{k} H_j^* G_{jy} + \sum_{i=1}^{k}\sum_{j=1}^{k} H_j^* H_i X_j^* X_i \tag{2.11}$$

This equation yields the noise auto spectrum as a function of any H vector. To minimize the noise term, this equation can be differentiated with respect to H^* and the result set to zero as shown

$$\frac{\partial G_{nn}}{\partial H_j^*} = -G_{jy} + \sum_{i=1}^{k} H_i G_{ji} = 0 \tag{2.12}$$

or,

$$G_{jy} = \sum_{i=1}^{k} H_i G_{ji} \tag{2.13}$$

As can be easily seen, this results in the same formulation as Eq. (2.4). This means that when a MISO model is used to describe an actual system, the analysis should be carried out as if no noise is present at all. The matrix equation will provide the best fit to G_{yy} using the inputs specified. The amount of noise present can then be found by

$$G_{nn} = G_{yy} - G'_{yy} \tag{2.14}$$

where G'_{yy} is the computed output auto spectrum and G_{yy} is the actual system output as measured. If the noise auto spectrum G_{nn} is deemed unacceptably high, there is no way to achieve a lower amount of noise with the inputs specified. The only way to decrease G_{nn} is by increasing the number of inputs or by replacing some or all of the original inputs with a more complete input set.

2.3.3. MULTIPLE COHERENCE

Rather than judging the adequacy of a model by the magnitude of G_{nn}, it is standard practice in MISO analysis to rate models of actual systems by their multiple coherence functions. This follows from the practice of employing ordinary coherence functions to describe input/output relation in single-input/single-output frequency-domain analysis. Multiple coherence is the same concept as ordinary coherence, only extended to MISO systems. Using the nomenclature of Eq. (2.14), multiple coherence can be defined as

$$\gamma^2_{y:x} = \frac{G'_{yy}}{G_{yy}} = 1 - \frac{G_{nn}}{G_{yy}} \tag{2.15}$$

where the subscript $y:x$ can be read "*the portion of y which is directly due to all x's*".

Since $G'_{yy} < G_{yy}$ for all cases, it is evident that for all frequencies

$$0 \le \gamma^2_{y:x} \le 1 \tag{2.16}$$

which is akin to ordinary coherence. As in the case of ordinary coherence, values of $\gamma_{y:x}^2$ close to one indicate a satisfactory model. Values of $\gamma_{y:x}^2$ close to zero either indicate a poor model, or near zero output at the frequency exhibiting low coherence.

2.4. CONDITIONED SPECTRAL ANALYSIS

A more sophisticated approach to MISO models involves the use of conditioned inputs. This approach replaces the model in Fig. 2.1 with the model of Fig. 2.2. The notation of Fig. 2.2 is as follows:

$x_{2.1}$ reads *"input two with the linear effects of input one removed"*, or *"conditioned out"*

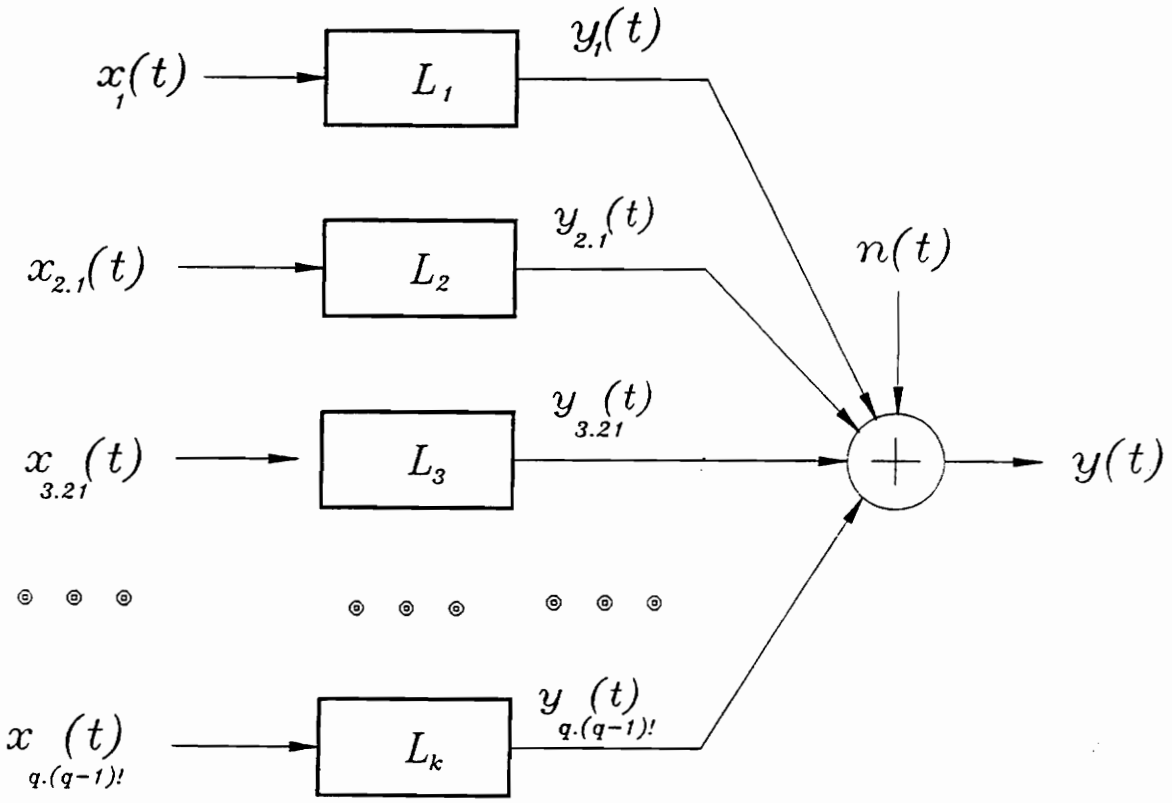

FIGURE 2.2. Conditioned Spectral MISO Model

$y_{3.21}$ reads *"the output caused by input three with the linear effects of inputs two and one removed"*

and so on. This terminology can be extended into the frequency domain as follows:

$G_{22.1}$ reads "*the auto spectrum of input two with the linear effects of input one removed*"

$G_{33.12}$ reads "*the auto spectrum of input three with the linear effects of inputs one and two removed*"

$G_{2y.1}$ reads "*the cross spectrum of input two and the output with the linear effects of input one removed*"

and so on.

As can be seen, the aim of this method is to replace the original inputs (which may be correlated with other inputs) with a new set of inputs which have the linear effects of the other inputs removed. Notice, however, that this method requires a ranking of the inputs. In Fig. 2.2, the effects of input one are removed from input two but not vice versa. This is because it is assumed that causality exists between the inputs. If instead it is assumed that there is no causality and a model as in Fig. 2.3 is attempted, the mathematics of this technique will not represent the output of the system truthfully. This ranking, or prioritizing, of inputs must be kept in mind when interpreting physical systems and will be discussed in more detail in section 2.4.4.

This treatment of conditioned records is presented due to its insight into the nature of physical systems, not its simplicity of calculation. Although several methods of derivation are available, this development follows from Bendat [7] and Dodds and Robson [10] most closely. Much has been left out of the full derivation due to the complexity of the full treatment. Bendat [8] also presents an independent proof of these results. For more detailed derivations of the concepts introduced here, see these references.

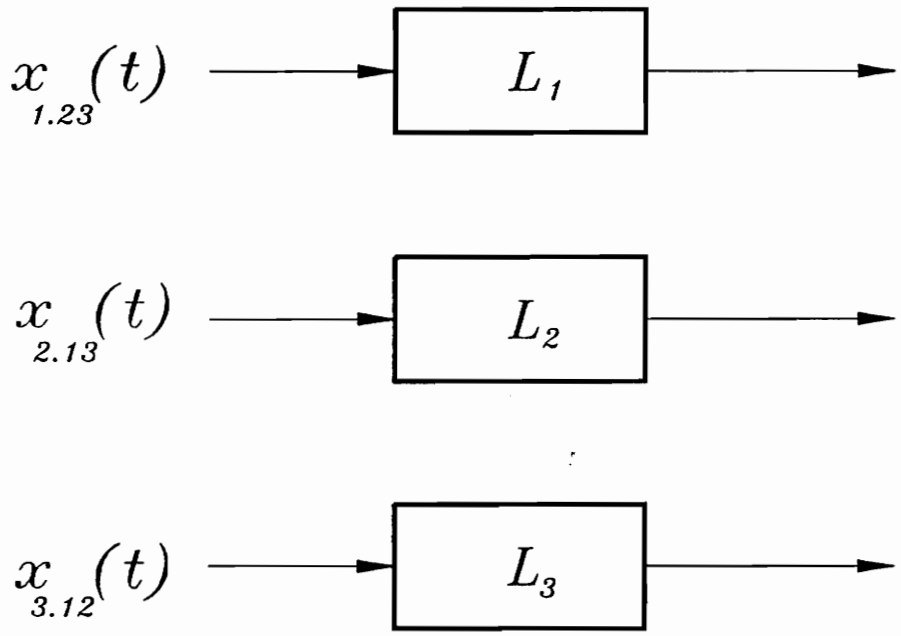

FIGURE 2.3. Incorrect Conditioning of MISO Inputs

2.4.1. DERIVATION OF CONDITIONED SPECTRAL DENSITY FUNCTIONS

The first step in solving for the conditioned spectral density functions involves creating a new matrix which we can call the ξ matrix. This is a triangular matrix defined as follows:

$$[\xi]=\begin{vmatrix} \xi_{11} & 0 & 0 & \cdots & 0 \\ \xi_{21} & \xi_{22} & 0 & \cdots & 0 \\ \xi_{31} & \xi_{32} & \xi_{33} & \cdots & 0 \\ \cdots & \cdots & \cdots & \cdots & \cdot \\ \xi_{k1} & \xi_{k2} & \xi_{k3} & \cdots & \xi_{kk} \end{vmatrix} \qquad (2.17)$$

The elements of the ξ matrix are defined so as to satisfy the following relationship with the input spectral matrix $[G]$:

$$[G]=[\xi^*][G_{ww}][\xi]^T \qquad (2.18)$$

where G_{ww} is a matrix of incoherent white noise sources. This ξ matrix redescribes the k input system as $k+1$ incoherent white noise sources as shown in Fig. 2.4. For a three input system for example, four incoherent white noise systems could be operated by Eq. (2.18) to return the three original inputs and the output of the model. Note that the white noise matrix G_{ww} can be replaced by the identity matrix if the magnitudes of the white noise sources are considered unity. Doing this yields the simpler equation relating the ξ matrix to the input spectral matrix

$$[G] = [\xi^*][\xi]^T \qquad (2.19)$$

The equation which relates general terms of the ξ matrix to terms of input spectral matrix is given as

$$G_{ij} = \sum_{n=1}^{i} \xi^*_{in}\xi_{jn} \qquad (2.20)$$

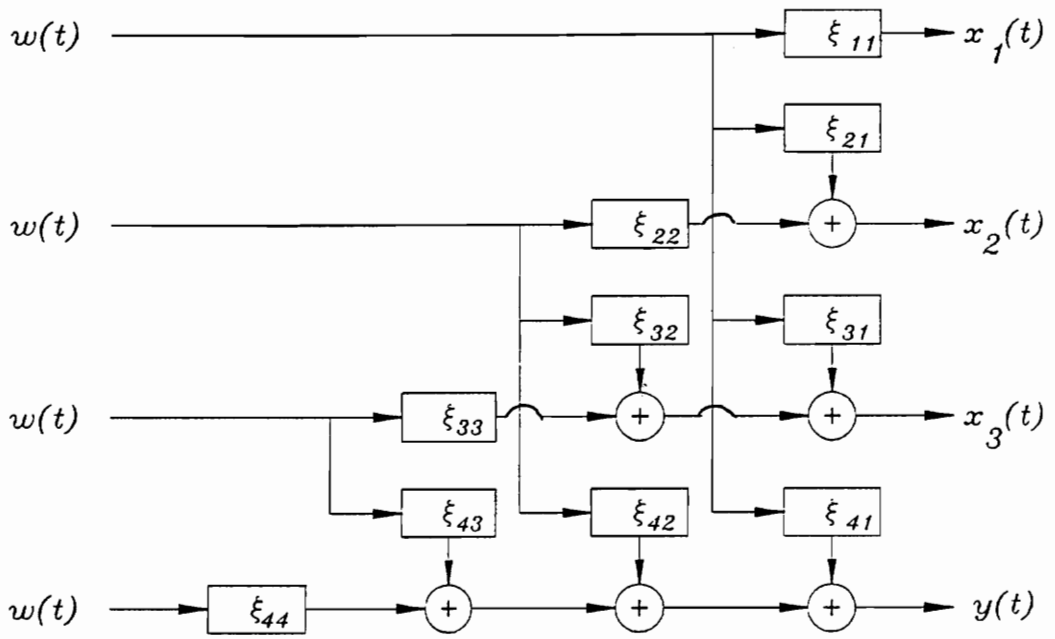

FIGURE 2.4. The ξ Matrix

For example, the cross spectrum G_{2y} could be described by ξ terms as

$$G_{2y} = \xi^*_{21}\xi_{k+1,1} + \xi_{22}\xi_{k+1,2} \tag{2.21}$$

Referring to Fig. 2.4, it can be seen that the first term of Eq. (2.21) describes the linear effects of input one so that

$$G_{2y.1} = \xi_{22}\xi_{k+1,2} = \frac{G_{11}G_{2y} - G_{21}G_{1y}}{G_{11}} \tag{2.22}$$

This process can be repeated for any other input, so (without proof)

$$G_{iy.1} = \frac{(G_{11}G_{iy} - G_{i1}G_{1y})}{G_{11}} \tag{2.23}$$

Extending this concept to higher order inputs yields

$$G_{iy.12} = \frac{G_{22.1}G_{iy.1} - G_{i2.1}G_{2y.1}}{G_{22.1}} \tag{2.24}$$

$$G_{iy.123} = \frac{G_{33.12}G_{iy.12} - G_{i3.12}G_{3y.12}}{G_{33.12}} \tag{2.25}$$

$$G_{iy..1234} = \frac{G_{44.123}G_{iy.123} - G_{i4.123}G_{4y.123}}{G_{44.123}} \tag{2.26}$$

and so on. In this fashion, the output cross spectrum can be found between any input and the output with the linear effects of all higher priority inputs removed. This becomes an important tool when MISO analysis is applied to noise source/path problems as discussed in the next chapter.

Note that Eqs. (2.23) to (2.26) can also be used to generate conditioned auto spectra by letting the subscript y equal i. These terms are necessary to form higher order terms as can be seen in the equations.

2.4.2. PARTIAL COHERENCE

Another powerful extension of Eq. (2.23) involves letting the subscript i equal the output y. This yields

$$G_{yy.1} = G_{yy}(1-\gamma_{1y}^2) \tag{2.27}$$

which describes the output auto spectrum of the model, with the linear effects of input one removed. Extending this concept to the higher level Eqs. (2.24), (2.25) and so on becomes simple if partial coherence terms are included as shown:

$$G_{yy.12} = G_{yy.1}(1-\gamma_{2y.1}^2) \tag{2.28}$$

$$G_{yy.123} = G_{yy.12}(1-\gamma_{3y.12}^2) \tag{2.29}$$

These partial coherence terms are extensions of ordinary coherence and represent the coherence between various inputs and the output when linear effects of higher priority inputs are removed. Equations for partial coherence are formed analogously to ordinary coherence. For example, the partial coherence $\gamma^2_{iy.1}$ is formed by

$$\gamma_{iy.1}^2 = \frac{|G_{iy.1}|^2}{G_{i1.1}G_{yy.1}} \tag{2.30}$$

By substituting for the conditioned spectra from Eqs. (2.23) and (2.27), this becomes

$$\gamma_{iy.1}^2 = \frac{|G_{11}G_{iy} - G_{i1}G_{1y}|^2}{G_{11}^2 G_{ii} G_{yy}(1-\gamma_{1i}^2)(1-\gamma_{1y}^2)} \tag{2.31}$$

which is purely in terms of input and output auto and cross spectra. In the same manner, higher order partial coherences are found to be

$$\gamma^2_{iy.12} = \frac{|G_{22.1}G_{iy.1} - G_{i2.1}G_{2y.1}|^2}{G^2_{22.1}G_{ii.1}G_{yy.1}(1-\gamma^2_{2i.1})(1-\gamma^2_{2y.1})} \tag{2.32}$$

$$\gamma^2_{iy.123} = \frac{|G_{33.12}G_{iy.12} - G_{i3.12}G_{3y.12}|^2}{G^2_{33.12}G_{ii.12}G_{yy.12}(1-\gamma^2_{3i.12})(1-\gamma^2_{3y.12})} \tag{2.33}$$

and so on.

Note that as a general rule with conditioned spectral analysis, the equations build upon each other. For example, Eq. (2.33) can only be solved once Eq. (2.32) is known, and so on.

2.4.3. OUTPUT POWER SPECTRAL DENSITY FUNCTIONS

The preceding conditioned spectral analysis formulae can be combined to describe the total output of a model as follows:

Take for instance, a four input ($k=4$) model, then

$$G_{yy} = \gamma^2_{1y}G_{yy} + \gamma^2_{2y.1}G_{yy.1} + \gamma^2_{3y.12}G_{yy.12} + \gamma^2_{4y.123}G_{yy.123} + G_{yy.1234} \tag{2.34}$$

The first term describes the spectral output due to input one passing through all the inputs. The second term describes the spectral output from input two with the effects of input one removed, passing through paths two, three and four. Terms three and four are interpreted similarly, with term five representing the spectral output due to the noise term $n(t)$.

2.4.4. DETERMINATION OF PRIORITY AMONG INPUTS

As mentioned earlier, the results obtained from conditioned spectral analysis will vary depending upon the assignment of priority among inputs. When modeling a physical system, engineering judgment must be used to decide which input should be considered the cause of other inputs. In some physical systems this is evident, but in other cases it is difficult to assess without a method to guide the decision. The following development introduced by Park and Kim [15] describes the use of impulse response to help assign priority among inputs.

For systems with random or near random vibrations as inputs, the input auto spectra appear as nearly flat over some frequency range. In theory, a totally flat auto spectrum over an infinite range of frequencies can only result from an Dirac delta input in the time-domain. A Dirac delta input is defined as a input of zero-time duration and infinite magnitude with a finite area under the function. Although the time response to a Dirac delta input will vary depending on the degrees of freedom of the system, there will never be any content prior to time zero because the system has no precognition of the input.

The FRF between the input and output of a system has a magnitude equal to the ratio of output to input. In the case of a Dirac delta input, the FRF will resemble the response spectrum, because the input spectrum is constant across the frequency-domain. By taking the inverse Fourier transform of the FRF, the impulse response is formed. As in the case of the system response, the impulse response will have no content present prior to time zero.

Now assume an FRF is formed between the Dirac delta input and the system output with roles reversed. That is, with the Dirac delta input serving as output and the system response serving as output. Since this view of the system is reversed, the FRF will have magnitude of the actual system input over the actual system output. This FRF will resemble neither the input or the output in shape. When the impulse response is computed from this FRF, there is no guarantee that the time region prior to time zero will be devoid of any content. In fact, there is no real physical interpretation for what has been formed.

The impulse response may have any shape and most likely will appear random prior to and after time zero.

This is the concept for assigning priority among inputs using impulse response. For two inputs in question, two different FRF's can be formed with the both possible cases of which signal is input and which is output. The combination of input and output which results in less content prior to time zero in the time-domain is most likely the correct one. Then, the signal determined to be the input is given a rank of priority higher than the signal which was found to be the output. All possible combinations of inputs can thus be examined in this manner and rank determined.

This method relies on some subjectivity, admitted by its developers[15]. Also, as the inputs stray from being true random sources and begin to resemble deterministic inputs, the method deteriorates, yielding impulse responses which become nearly impossible to interpret. This results from input spectra which are not flat, but rather exhibit line spectra in the frequency-domain. The valleys surrounding these peaks likely contain low signal to noise ratios and the FRF's will exhibit random, large magnitudes. The impulse responses formed from these FRF's will contain confusing information. To perform this method with deterministic inputs requires more investigation into this method than currently exists in the literature.

2.5. VIRTUAL COHERENCE AND RELATED TECHNIQUES

Several similar techniques exist which approach the MISO model by replacing the model of Fig. 2.1 with that of Fig. 2.5. The idea here is to replace any number of coherent sources with a fewer number of totally incoherent sources. These sources can be considered as the minimum number of independent sources which are the ultimate origin of the inputs in the model. Names for this approach include Virtual Coherence methods[1], NIS (number of incoherent sources) analysis[16], and Principal Component Analysis (PCA)[17].

The mathematical principle behind these methods involves finding the eigenvalues and vectors of the input spectral matrix [G], defined in Eq. (2.7). Each eigenvalue of this

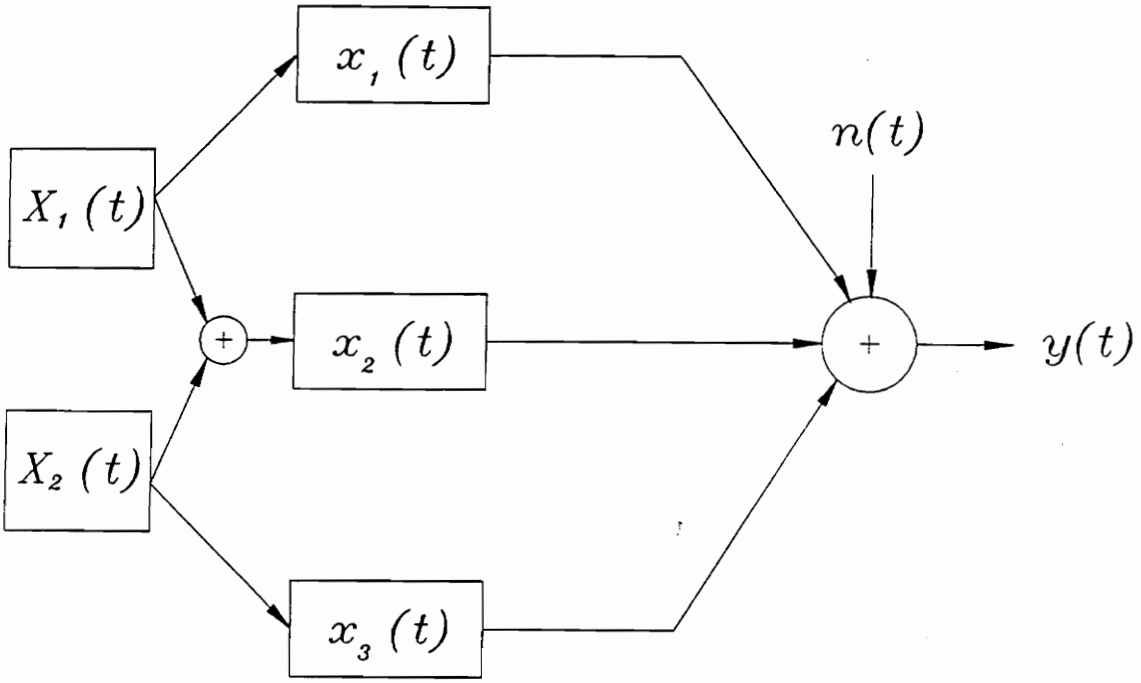

FIGURE 2.5. Virtual Source Model

matrix is a spectrum, describing the spectral input of a virtual source. Since the number of eigenvalues will equal the order of the input spectral matrix, the number of virtual sources will never exceed the number of inputs of the system. As a practical matter, the difference between the number of virtual sources and the number of system inputs will be made up by eigenvalues which are near zero, resulting in a number of "dominant" eigenvalues as well as some "insignificant" eigenvalues. Those which exhibit significant magnitudes are then dubbed the "principal components" or "virtual sources" of the system.

Let us define the diagonal matrix of the eigenvalues of $[G]$ as $[Q]$ and the unitary matrix of column-wise eigenvectors of $[G]$ as $[P]$. Then,

$$[Q] = [P]^h[G][P] \tag{2.35}$$

where superscript h denotes a Hemitian transpose. It is then possible to present the output of the MISO system in terms of virtual incoherent sources as (see [2] for further proof)

$$G_{yy} = \{H\}^h[P][Q][P]^h\{H\} \tag{2.36}$$

This method lets us replace a MISO model consisting of inputs that are somewhat coherent with one of a lesser number of incoherent inputs. This can answer the question of how many independent factors really contribute to the output of the MISO system.

It should be noted that the eigenvector solution of $[G]$ tends to group all deterministic content into the first eigenvector. This means that although two deterministic sources may be independent (i.e. two signal generators outputting the same signal), the virtual method assumes a relationship and thus attributes both signals to one virtual source. The two deterministic sources can have two entirely different paths for noise transmission, as well. One path can be far more important than the other, but this virtual coherence method lumps the two sources into one virtual source thus eliminating our capacity to determine the most important path in the noise transmission problem. This fact does nothing to diminish the validity of virtual source theory, but becomes important in the application of MISO modeling to noise-path determination, as described in the following chapter.

CHAPTER 3.
SOUND SOURCE IDENTIFICATION VIA MISO MODELS

This chapter discusses the application of MISO theory to the task of sound source and propagation path identification. The discussion will begin with physical interpretations of the MISO results presented in the previous chapter. Next, a discussion of practical aspects of the application of MISO theory to sound source identification will be presented, followed by some examples of sound source experiments from the literature. The discussion will conclude with a brief summary of which methods presented in this chapter are best suited for the analysis of the Bristol H25A compressor

3.1. PHYSICAL INTERPRETATIONS OF MISO RESULTS

This section presents the physical application of the various MISO approaches through the use of theoretical examples. The examples are composites of experiments actually performed by Trethewey [11], Price [1], Ufford and Bernhard [16] and Tweed and Branch [19] but specific results are not presented here. Rather, these experiments are used as a basis for discussion of theoretical results.

3.1.1. OPTIMUM FRF SOLUTION

Consider the physical system of Fig. 3.1. Two function generators are driving two speakers with white noise through two amplifiers. The generator labeled source one contributes to the signal of source two, thus providing a level of ordinary coherence between sources one and two (let us assume the coherence is moderate; that is, close to 0.5 over the frequency range of interest). A far-field microphone measures the output of the two speakers and the uncorrelated background noise. This output signal is fed to an FFT (Fast Fourier Transform) analyzer, capable of averaging the auto spectrum of the output G_{yy}. Likewise, the signals from the inputs are fed to the same FFT machine, enabling the input auto spectra G_{11} and G_{22}, as well as the cross spectra G_{12}, G_{21}, G_{1y}, and G_{2y} to be formed.

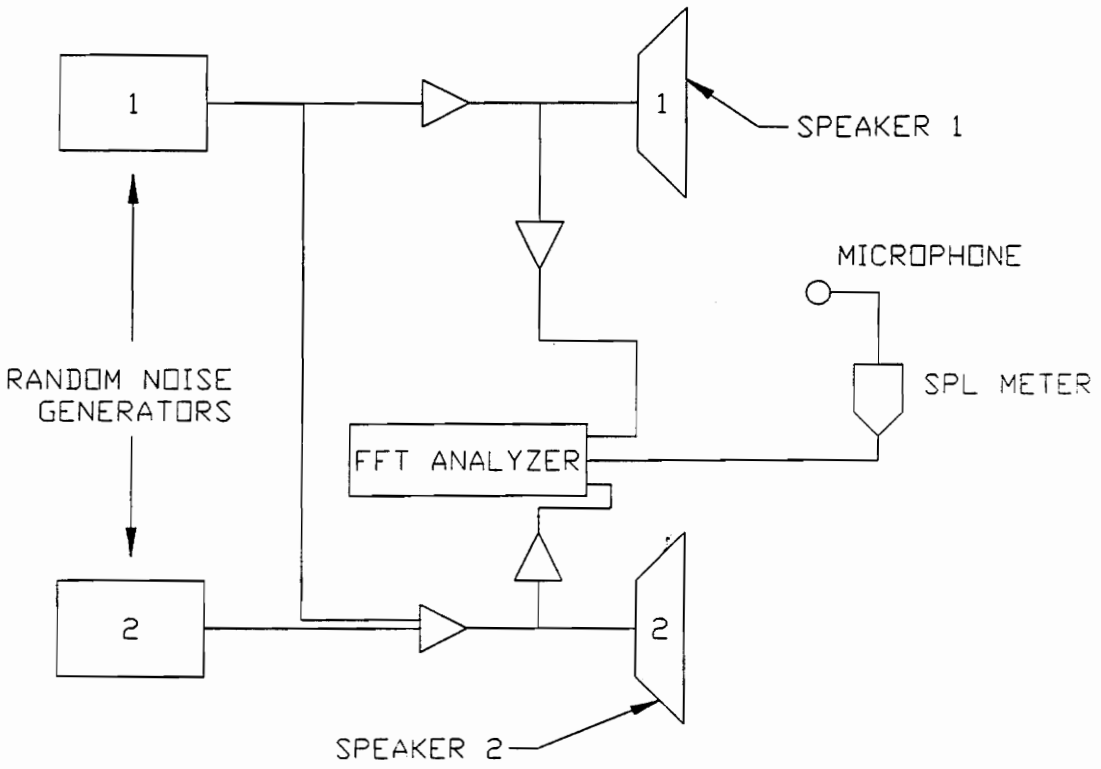

FIGURE 3.1. Example of MISO Experiment

Although quite simple, this system describes a typical sound source determination problem. The questions here are: Which source contributes the most sound to the far-field sound level in any given frequency range? What would be the result to the far-field sound level if one source were not present? Are all possible sources accounted for or does the background noise actually contain important sources as well? All these questions can obviously be answered in this case by simply turning off the sources one at a time and measuring the effect, but the power of the MISO model is that these questions can be answered without turning off either source. This allows for complicated systems to be analyzed where actual physical isolation is not possible.

The first step in the optimum FRF solution is to form the output and spectral matrices, as defined in Eq. (2.6) and Eq. (2.7). For this two input system, these are

$$\{G_y\} = \begin{vmatrix} G_{1y} \\ G_{2y} \end{vmatrix} \qquad [G] = \begin{bmatrix} G_{11} & G_{12} \\ G_{21} & G_{22} \end{bmatrix} \tag{3.1}$$

Next, from Eq. (2.8) the FRF vector is solved. For a two input model this solution is

$$\{H\} = \begin{vmatrix} H_1 \\ H_2 \end{vmatrix} = \begin{vmatrix} \dfrac{G_{22}G_{1y} - G_{12}G_{2y}}{G_{11}G_{22} - |G_{12}|^2} \\ \\ \dfrac{G_{11}G_{2y} - G_{21}G_{1y}}{G_{11}G_{22} - |G_{12}|^2} \end{vmatrix} \tag{3.2}$$

Finally, the model output is formed from Eq. (2.9) and is found to be

$$G'_{yy} = H_1{}^*H_1G_{11} + H_2{}^*H_2G_{22} + H_1{}^*H_2G_{12} + H_2{}^*H_1G_{21} \tag{3.3}$$

To form the multiple coherence function, the model output G'_{yy} is compared to the measured output G_{yy}. The difference between the two clearly depends on the amount of extraneous noise in the system. Equation (2.15) is used to form the multiple coherence function. If this function is low in the frequency range of interest, then the model should be considered inappropriate and a new set of inputs chosen. The literature [11],[6] tends

to suggest that multiple coherence values below 0.7 indicate model insufficiency, but the final decision is left to engineering judgment.

The terms of G'_{yy} in Eq. (3.3) describe the output entirely in terms of measurable spectra. The first two terms of Eq. (3.3) describe the contribution of the sources directly while the last two terms are due to the interaction of the sources. Several manipulations can be performed at this point to further understand the system. By letting H_1 equal zero in Eq. (3.3), the resulting G_{yy} would describe the output of the system with function generator one and speaker one turned off. Likewise, letting H_2 in Eq. (3.3) equal zero would describe the output of the system if function generator two and speaker two were turned off. For a system of more than two inputs, this process could be repeated for any source or combination of sources with similar physical interpretation.

Note, however, that this process does not account for all the radiated sound in the system because the sound with source one turned off, $H_2{}^*H_2G_{22}$, plus the sound with source two turned off, $H_1{}^*H_1G_{11}$, does not sum to the total sound with both sources on. This occurs because the coherence between inputs is ignored by this method. The part of source one which sums with source two is never accounted for in this model because all of the cross terms in Eq. (3.3) become zero when either FRF term is set to zero. This does not mean, however, that this approach is without merit. This process can still yield useful information about a system, even if input coherence exists in the actual system. What is found here is an upper bound of sound reduction, as if both a sound making component itself were removed from a system as well as the potential for other sources to radiate through that component. This method of modeling sound sources is presented by Trethewey [11] via results of actual generator/speaker experiments.

An important point should be mentioned here regarding the cross coherence terms in Eq. (3.3). In true physical systems, these terms may be positive or negative; their sign depending upon the phasing of the vibrating components in question. In certain physical systems this phase can be random and thus the cross terms cancel out one another almost entirely. In a case such as this, the method of the previous paragraph may, in fact, provide an excellent approximation to actual sound reduction. Trethewey [11] and Seybert and Crocker [20],[21] both note this fact, and use it to defend their exclusive use of this approach in their work.

Taking another approach, the coherent outputs could be formed. These would be

$$\gamma_{1y}^2 G_{yy} = H_1{}^* H_1 G_{11} + \gamma_{12}^2 H_2{}^* H_2 G_{22} + H_1{}^* H_2 G_{12} + H_2{}^* H_1 G_{21} \qquad (3.4)$$

and

$$\gamma_{2y}^2 G_{yy} = \gamma_{12}^2 H_1{}^* H_1 G_{11} + H_2{}^* H_2 G_{22} + H_1{}^* H_2 G_{12} + H_2{}^* H_1 G_{21} \qquad (3.5)$$

The interpretation of these terms is slightly different than the case of deleting H terms from Eq. (3.3). Here $\gamma_{1y}{}^2 G_{yy}$ represents the spectral output of source one through all possible paths. This would be interpreted as turning off generator two but leaving speaker two on for generator one to drive. $\gamma_{2y}{}^2 G_{yy}$ represents the case of speaker one turned off but generator one left on so as to still add to the output of speaker two. Note that

$$\gamma_{1y}^2 G_{yy} + \gamma_{2y}^2 G_{yy} \neq G_{yy} \qquad (3.6)$$

because this approach accounts for the cross terms of Eq. (3.3) more than once. This is shown by Bendat and Piersol [6] quantitatively. This approach to MISO models is not recommended due to the complexity of interpretation if many sources are presented. Conditioned spectral analysis is preferred if coherence between inputs is to be considered because it accounts for the cross terms only once. This will be demonstrated in the following section.

3.1.2. CONDITIONED SPECTRAL ANALYSIS

The conditioned spectral analysis approach utilizes a model of G_{yy} as shown in Eq. (2.34). Assuming that it can be correctly deduced that source one is the highest priority input, the output G_{yy} in this case would be represented as

$$G_{yy} = \gamma_{1y}^2 G_{yy} + \gamma_{2y.1}^2 G_{yy.1} \qquad (3.7)$$

where, from Eqs. (2.23) and (2.30)

$$\gamma^2_{2y.1} = \frac{|G_{2y.1}|^2}{G_{22.1}G_{yy.1}} \qquad G_{22.1} = \frac{G_{11}G_{2y} - G_{21}G_{1y}}{G_{11}}$$

$$G_{2y.1} = \frac{G_{11}G_{2y} - G_{21}G_{1y}}{G_{11}} \qquad G_{yy.1} = \frac{G_{11}G_{yy} - G_{y1}G_{1y}}{G_{11}} \tag{3.8}$$

Notice here that the first term of Eq. (3.7) is the same as Eq. (3.4). This means that the first term represents the contribution of source one through speaker one and speaker two. In other words, removing this term would yield the output of the system if function generator one were turned off. The second term describes the contribution of source two through speaker two. Deleting this term would describe the output if generator two were turned off, but speaker two left on for generator one to still drive. Tweed and Branch [19] demonstrate this via generator/speaker experiments as well as with several computer simulations.

Contrast this with the setting of H terms equal to zero in the optimal FRF model given in Eq. (3.3). The difference between these two methods can best be described in terms of our signal generator/speaker model of Fig. 3.1 as below:

Setting $H_{i} = 0$ in the optimal FRF model of a system Eq. (2.5),Eq. (2.9) represents turning off the ith function generator and the ith speaker.

Deleting $\gamma_{iy}{}^2 G_{yy}$ from the conditioned spectral model of a system Eq. (2.34) represents turning off the ith function generator only; not the ith speaker.

Note once again that the priority ranking for the use of the conditioned spectral model is of utmost importance. If the following model were used to describe the system of Fig. 3.1,

$$G_{yy} = \gamma^2_{2y} G_{yy} + \gamma^2_{1y.2} G_{yy.1} \tag{3.9}$$

then the physical interpretation of the model would produce erroneous and confusing results.

3.1.3. VIRTUAL COHERENCE/PRINCIPAL COMPONENTS

Since virtual methods address a different problem altogether, let us create a new system, as shown in Fig. 3.2. Here we have two generators driving three speakers and a three input system. For this model, let us assume source one provides a larger magnitude signal than source two. Microphones in front of each speaker will transmit the inputs to the analyzer. Since these microphones will pick up some content from each speaker, the three inputs will be coherent to some degree.

The question to be answered here is: With q coherent inputs measured, how many incoherent sources are actually present? Note that no more than q incoherent sources may be determined, so for this kind of analysis it is best to include as many possible inputs as can be reasonably found.

The first step is to form the spectral matrix Eq. (2.7). For a three input system this would be

$$[G]=\begin{bmatrix} G_{11} & G_{12} & G_{13} \\ G_{21} & G_{22} & G_{23} \\ G_{31} & G_{32} & G_{33} \end{bmatrix} \tag{3.10}$$

Next, the eigenvalues and eigenvectors of $[G]$ are determined by any one of several methods. The first eigenvalue, which will be a spectrum, should represent the spectra of the most dominant independent source, source one. The second eigenvalue should be the spectra of generator two. The third eigenvector will be the least dominant independent source, the noise present, assuming the magnitude of the noise is small compared to the magnitudes of generators one and two. The conclusion then is that two independent sources are present, with no prior knowledge of that fact. Actual physical experiments of this sort are presented by Ufford and Bernhard [16], and by Price [1].

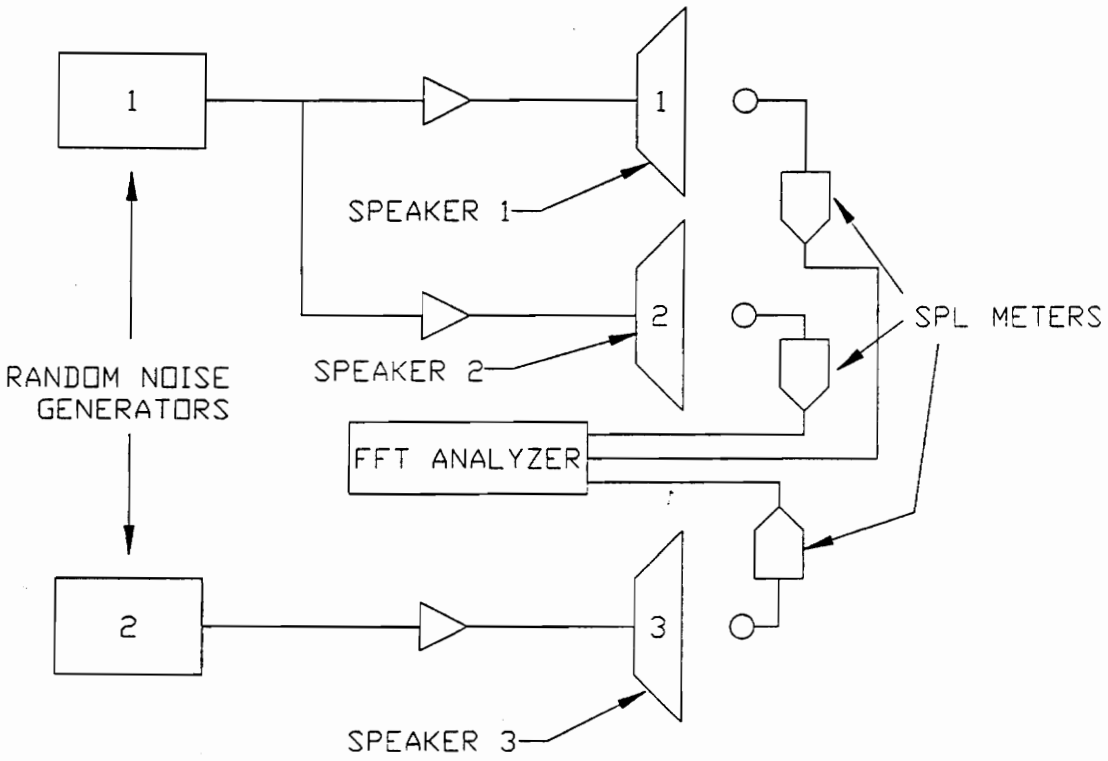

FIGURE 3.2. Example of Virtual Source Experiment

Note that if the signal generators were generating the same deterministic function, this method would fail to determine two independent generators. The first eigenvalue would contain all of the deterministic signal and the other two eigenvalues would be noise terms. Ufford and Bernhard [16] and Price [1] both demonstrate this phenomenon physically. This is an important flaw in this method, especially when it is applied to reciprocating machines such as compressors. Vibrations caused by shaft rotation, piston slap, electric motor fields, etc. are deterministic. For this reason, the virtual approach has only limited use in many engineering applications.

3.2. DATA ACQUISITION CONCERNS IN SOUND PATH IDENTIFICATION

As the previous section has stated, many experiments have verified the applicability of MISO modeling to actual physical systems. In contrast to this fact is the failure of early field applications of MISO models in industry to yield totally meaningful results [21] [22] [23] [24]. The complexity of modeling an actual machine or industrial system seems to be due mainly to the vast number of error sources present in a non-controlled test environment. A brief listing of error sources demonstrates the pitfalls awaiting the experimentalist:

1. Low signal-to-noise ratios on transducers
2. Inappropriate input selection
3. Contamination of input signals by other inputs
4. Input/Output feedback
5. Time delay/Reverberation effects
6. Quantization error
7. Resolution error
8. Leakage effects
9. FRF estimation error
10. Non-linearities and time varying properties of system
11. Insufficient averaging
12. Intrusive effects of instrumentation

Although it not possible to discuss all of these error sources in great detail, this section will discuss some of the common sources of experimental error that can possibly be avoided with some forethought. Errors which are unique to MISO systems will be covered in the most detail. Some other error sources which are common to single input systems will also be briefly discussed, but no claim is made to presenting a complete discussion of error sources in experiments. Further details can be found in the references mentioned.

3.2.1. SIGNAL NOISE

Although the MISO model accounts for uncorrelated noise at the model output, noise at the inputs can also cause low levels of multiple coherence. The result of high uncorrelated noise levels on the inputs (such as unwanted 60 Hz power line content) is an underestimation of the source contribution of the inputs to the output. If the input measurement noise is coherent with the input signals, there is a good chance that a possible source has been left out. Incoherent noise on the other hand may simply result from low output from a transducer. Hence, when low multiple coherence is encountered, it is difficult to ascertain whether or not a source is missing or whether transducer output is low. This can cause confusion when multiple coherence is consulted for evaluation of the model.

This problem can be avoided by providing as high a signal-to-noise ratio as possible in the measurement transducers. If the measuring device is an accelerometer or other surface mounted transducer, this can be done by placing the transducer away from nodal lines of the vibrating component in question. For non-surface transducers such as microphones, staying away from minimums in the directivity of radiated sound is desirable.

Another noise issue is correlated noise on the output signal. This is a symptom of unaccounted-for sources and also results in low multiple coherence. Noise of this type can only be fixed by including another input or replacing some current inputs with more suitable inputs.

3.2.2. CONTAMINATION

An error source unique to multiple-input problems is the contamination of an input signal with another input signal. This is caused by an input transducer receiving input from more than one source during data acquisition. The results of contamination depend upon the priority of the inputs involved, as demonstrated in an experiment by Tweed and Branch [19].

When contamination is "downward", that is when a higher priority signal contaminates the transducer of a lower priority signal, the effect of contamination does not produce significant error when conditioned spectral quantities are developed. This is because the contamination is in the same direction as the physical correlation and is conditioned out by the mathematical procedure.

When contamination is "upward", or against the flow of physical correlation, Tweed and Branch [19] demonstrate significant errors in the model spectra. This is because the conditioned spectral analysis technique cannot remove the effects of upward contamination while it is removing downward physical effects.

When the optimum FRF approach is used, no correlation is considered between inputs, so all contamination is considered part of the measured input. This obviously can cause serious errors in the results of the experiment. Virtual coherence methods are immune from contamination because the goal of this process is the removal of all correlation effects.

The best method of preventing contamination is the use of transducers which physically attach to mechanical surfaces (such as accelerometers) to measure acoustic radiation. Near-field microphones are extremely susceptible to contamination and thus should only be used when physical limitations demand their use.

3.2.3. CHANGE OF SYSTEM DUE TO INSTRUMENTATION

An important error source is the intrusive effect of transducers on a physical system. The aim in any experiment is to measure an event without the measurement

process interfering with the event, but this is rarely possible. As will be described in the next chapter, an attempt should be made to quantify the effect of instrumentation on a system before any instrumentation scheme is adopted. Only those schemes which minimize the altering of a system should be considered, and significant changes to a system should be accepted only when no other choices exist.

3.2.4. INAPPROPRIATE INPUT SELECTION

When constructing a multiple-input model, it is important to utilize sound engineering judgment to select which inputs will be considered as causing the system output. The following guidelines have been proposed to guide the selection of inputs in a multiple-input model[6].

1. The ordinary coherence between any two inputs should not be unity. If this occurs, redundant information is present in the input side of the model.

2. The ordinary coherence between any input and the output should not be unity. If this occurs, the output can be described by a single input system.

3. The multiple coherence between one input and the other inputs should not be unity. If this occurs, the input is a linear combination of the other inputs and should be eliminated.

4. The multiple coherence between the inputs and the output should be sufficiently close to unity. this indicates that the inputs selected adequately describe the system output.

3.3. PREVIOUS RESULTS OF EXPERIMENTS USING MISO METHODS.

As was mentioned in section 3.1, the literature contains many examples of controlled experiments which validate the application of MISO modeling to sound source/path identification [1] [19] [11] [16] [6]. Most of these experiments utilized speakers driven by white noise [1] [19] [11] [16] or computer/circuit simulations [1] [19] [11] . A few constructed controllable structures [19] [6]. What all of these experiments

shared, however, was the advantage of the controlled environment. In simulations and speaker tests it is possible to turn sources off and verify model results. In controllable structures it is simple to mount transducers and select the inputs of the model.

Contrasted to this is the application of MISO modeling to field testing for industrial situations. As will be discussed, many attempts at modeling true physical systems were deemed inconclusive or only partially conclusive by the experimenters involved [21] [22] [23] [24]. Despite these shortcomings, it is commonly felt that experimental errors arising from the complex instrumentation and numerical computation involved in such projects are the main source of poor results, not the underlying theory; an opinion echoed by Trethewey [11] and Tweed and Branch [19] among others.

This section will discuss some key applications of MISO modeling to industrial noise source identification problems from the literature. Although it is not possible to fully discuss every experiment attempted in this area, results will be discussed from examples which clarify key points regarding error sources and interpretation of results.

3.3.1. CONDITIONED SPECTRA AND OPTIMUM FRF EXPERIMENTS

An early example of a multiple-input experiment is the work of Koss and Alfredson [23] in 1974. The goal of this study was to identify the major sources of noise in a punch press machine. A three input/single output model was selected based upon engineering knowledge of punch presses. Due to the lack of inexpensive multi-channel FFT processors at the time, severe limitations (by today's standards) were put on the data collection. Five ensembles of data were averaged from accelerometers at the inputs and a microphone at the output. These ensembles were not acquired simultaneously. To combat reverberation effects, the experiment was performed in an anechoic chamber. The data processing involved computing the partial coherence between each input and the output. By comparing these coherences, it was decided which components contributed to the output noise the most. No attempt, however, was made to determine coherent output of the individual sources. This experiment was described by its performers as moderately successful. The largest error sources here appear to be the disjoint samples (which can destroy the phase information of the cross coherences), the small number of ensembles

used for averaging, and possibly the crudeness of the equipment used as compared to the equipment of today.

The work of Chung, Crocker, and Hamilton [25] in 1975 was one of many attempts at the application of MISO modeling to noise reduction for diesel engines. Their study modeling the engine with a pressure transducers at each of the six cylinders in a V6 engine. The output was measured by a far-field microphone. The results simply showed that most of the diesel engine noise at low and mid frequencies was highly coherent with the cylinder noise, as evidenced by the multiple coherence function. FRF's between the cylinders and the output sound was also found. Error sources here may have been caused by non-simultaneous data collection, and no attempt at accounting for time delay.

Further work on Diesel engines was performed by Alfredson [22], by Hayes, Seybert, and Hamilton [24] and by Seybert and Crocker [21]. Alfredson modeled the diesel engine more completely by placing near-field microphones near possible sound sources. His approach was to compute the partial coherence of sources with the far-field sound level and rank the sources based upon the magnitude of partial coherence values. His conclusions doubted the usefulness of MISO techniques as applied to sound source identification problems. The confusion in his results were most likely caused by contamination effects caused by the microphones. Seybert and Crocker [21] found some meaningful results using the FRF approach, but had some multiple coherence values greater than one, which indicates some error in the numerical methods used. Hayes, Seybert, and Hamilton [24] also experienced some numerical error evidenced by the fact that their model output exceeded the output at some frequencies.

An attempt to determine vibration sources on an ultra-high frequency antenna was attempted by Pearson and Thaller [26] in 1976. Their model was a six input/three output model utilizing both accelerometers and pressure transducers. The highlight here is the unique approach used to determine the major sources of structural vibration. Once a model was found that resulted in multiple coherence function above 0.9 in nearly all frequencies, inputs were removed from the model one at a time and the multiple coherence was re-calculated. Whichever input caused the largest drop in multiple coherence when it was removed was deemed the largest contributor to structural vibration.

An attempt was made by Trethewey [11], Trethewey and Evensen [13], and by Trethewey, Evensen, and Shapton [14] from 1981-1983 to identify the major sound sources on a forge hammer. This study combine various input/output models with modal analysis to adequately describe the transient sound caused by the impact of the forge hammer onto the anvil. Conclusions from various experiments included the importance of simultaneous data collection for all channels, the importance of avoiding signal contamination and proper placement of transducers, and the susceptibility of the Hanning window to time delay errors. Although it was determined that the optimum FRF method may cause errors by neglecting spectral cross terms, no conditioned spectral analysis was attempted. Due to the recognition and avoidance of problems encountered past experiments, this was truly a landmark study.

3.3.2. VIRTUAL COHERENCE/PRINCIPAL COMPONENTS

One experiment which relied solely on the use of virtual methods to analyze the sound sources of a machine was performed by Price [1] in 1985 on hermetically sealed compressors. After performing controlled experiments, this method was applied to a compressor with a model of four inputs: the gas path, the oil path, the spring path, and the shock loop path. The model identified four significant incoherent sources in the compressor. The interpretation of this result, however, was difficult. The first virtual source contained the deterministic signal, so the other virtual sources suggested some random content to compressor sound. The identification of what the virtual sources represented, however, was simply not possible.

3.3.3. CONCLUSIONS

Based upon the results of past experiments, it seems possible that a MISO study can successfully be completed. Some of the short-comings in the past experiments can be attributed to numerical error or limitations in older FFT analyzers [23] [24] [26]. Others were affected by errors not thought important at the time but now more clearly understood [22] [24] [25]. With technological advancements in digital computers and multi-channel FFT analyzers, and with the lessons learned from the pioneering attempts in multiple-input experiments in the past, it is felt that the experimenter of today can

successfully obtain meaningful results from sound path/source determination problems with the use of MISO modeling.

For the H25A study discussed in this thesis, the optimum FRF method described in section 3.1.1 appears to be the most useful of the analysis techniques. This is because its results are easily obtained and can be physically interpreted without confusion. This is not necessarily true of the other methods described in this chapter.

The conditioned spectral model of section 3.1.2 is not expected to provide much useful insight into the H25A compressor study because of the necessity of prioritizing the inputs when using this method. If the model of sound propagation within a compressor is assumed to behave as shown in Fig. 1.3, the propagation paths to be investigated in this study are parallel paths. That is, they both result from the same source. As a result, there is no causality expected among these propagation paths. The method of assigning priority proposed by Park and Kim[15] is not applicable because the system is not randomly excited.

The virtual coherence method of section 3.1.3 is likewise not expected to yield useful information because it also has shortcomings when applied to deterministic systems. As evidenced in the conclusions of Price[1], this method yields ambiguous results when applied to reciprocating compressors. For that reason, it was not applied in this study.

CHAPTER 4.
INSTRUMENTATION AND TESTING OF BRISTOL H25A COMPRESSOR

In order to perform the multiple-input/single-output (MISO) analysis of the Bristol H25A Compressor, it was first necessary to instrument a typical production compressor with the appropriate transducers and acquire experimental data. This task required much forethought, as evidenced by the possibilities for experimental error discussed in section 3.2. This chapter will begin with a discussion of the selection and installation procedure for the transducers used to collect experimental data from the compressor. Secondly, the effect of the instrumentation on the operational characteristics and the dynamic response of the compressor will be described and discussed. Finally, a description of the compressor test set-up and the data acquisition procedure is given.

4.1. SELECTION AND INSTALLATION OF TRANSDUCERS

Since the purpose of the MISO experiment was to determine and rank sound sources and paths inside of the H25A compressor, it was first necessary to use engineering judgment to pick the sound sources and paths to investigate. This was done with the aid of David Gilliam of Bristol Compressors whose experience with this type of compressor can be considered extensive. As was discussed in section 1.3, the primary sound transmission paths chosen for investigation were the housing cavity pressure, the suspension springs, the shock-loop tube, and the suction and exhaust pressures. The following section explains the procedure of selecting and installing the transducers to measure these sound transmission paths.

In all, 23 separate input signals were decided upon. These included 15 signals from the anticipated sound transmission paths, a trigger signal, the cylinder pressures, and 9 compressor acceleration signals needed for the dynamic model mentioned in section 1.1. Table 4.1 lists the location, type, model, and purpose of the 23 transducer signals. Figure 4.1 shows the physical locations of the transducers within the compressor.

TABLE 4.1 Summary of H25A Instrumentation

Location	Type	Model	Measurement
Right Mount: X axis	Triaxial Piezo-Electric Force	Kistler 9251D	Mechanical Transmission Path
Right Mount: Y axis	"	"	"
Right Mount: Z axis	"	"	"
Left Mount: X axis	"	"	"
Left Mount: Y axis	"	"	"
Left Mount: Z axis	"	"	"
Top Mount: X axis	"	Kistler 9251A	"
Top Mount: Y axis	"	"	"
Top Mount: Z axis	"	"	"
Shock-loop	Piezo-Accelerometer	Kistler 8122	"
Housing Cavity	Piezoelectric Pressure	PCB116A	Pressure Transmission Path
Top Cylinder	"	PCB113A22	Sound Source
Bottom Cylinder	"	"	"
Exhaust Pressure	"	PCB113A24	Pressure Transmission Path
Suction Pressure	Pressure	"	"
Crankshaft Encoder	Magnetic Pickup	N/A	Trigger/Speed Variation
Far-Field	Microphone	B&K4166	Sound Output
Crankcase X axis	Triaxial Piezo-Accelerometer	Kistler 8792A500	Dynamic Study
Crankcase Y axis	"	"	"
Crankcase Z axis	"	"	"
Motor Cap X axis	"	"	"
Motor Cap Y axis	"	"	"
Motor Cap Z axis	"	"	"

1	Right Triaxial Force Transducer
2	Left Triaxial Force Transducer
3	Top Triaxial Force Transducer
4	Shock Loop Accelerometer
5	Housing Pressure Transducer
6	Top Cylinder Pressure Transducer
7	Bottom Cylinder Pressure Transducer
8	Exhaust Pressure Transducer
9	Suction Pressure Transducer
10	Crankshaft Gear
11	Crankcase Accelerometer
12	Motor Cap Accelerometer

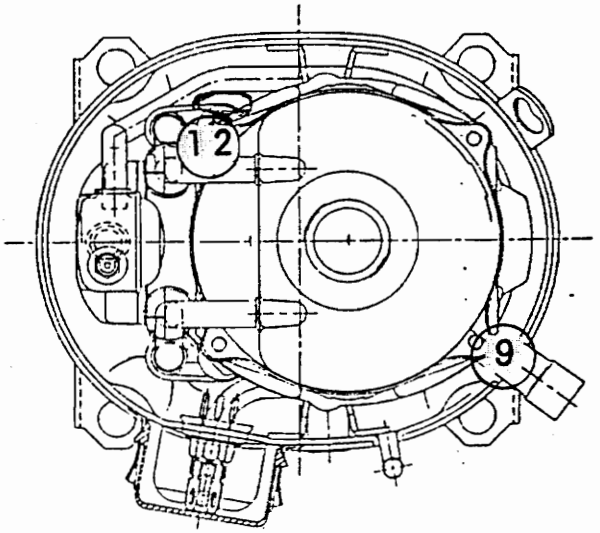

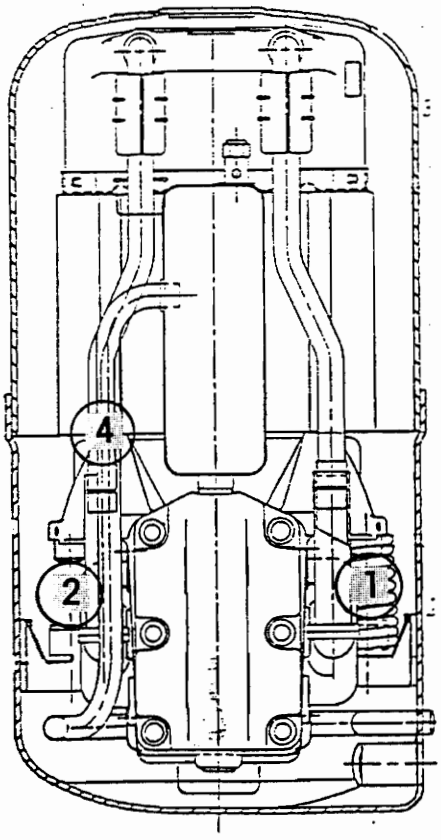

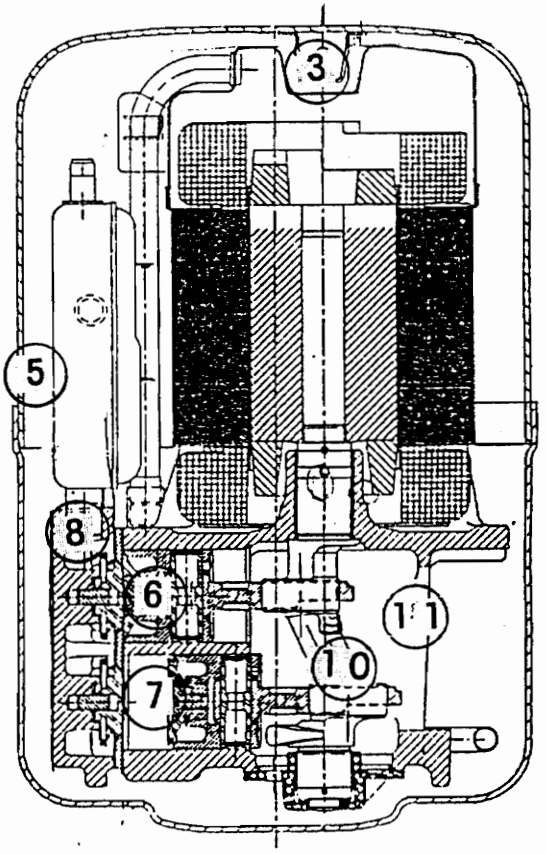

FIGURE 4.1. Instrumentation of H25A Compressor

4.1.1. GENERAL CONSIDERATIONS FOR TRANSDUCER INSTALLATION

There were several factors which guided the selection and installation of transducers, regardless of their specific type or location. Most notable of these factors was the environmental condition inside the compressor. All transducers selected were ensured to be refrigerant-proof and oil-proof, at least for a limited time. Even though some transducers were mounted away from the oil puddle in the shell bottom, this was necessary due to oil mist which circulates throughout the compressor. Special attention was made to rubber or plastic parts, which might be susceptible to decay when in contact with refrigerant or oil. In many cases, transducer vendors were able to recommend refrigerant- and oil-proof products from their product line.

Other environmental concerns were temperature and electromagnetic field problems within the compressor. To ensure the survival of all transducers, they were required to operate at a temperature of 200° F (93° C). This was the criterion for the Bristol H23A study and resulted in no transducer loss due to temperature[4]. Due to the AC electric motor driving the compressor, it was necessary to consider electromagnetic field contamination of transducer signals. This resulted in the placement of transducers as far from the motor as physically possible, as will be discussed in some of the following sections.

The next priority for transducer selection was for the installed instrumentation to change the compressor dynamics as little as possible. The H23A study indicated a reduction of compressor noise by 4 dB after instrumentation[4]. This change is significant because it indicates the results and conclusions of the study were based on a different dynamic system than the original compressor considered. For this reason, a conscience effort was made to minimize the change to compressor geometry during transducer installation.

For most of the applications, piezoelectric transducers were chosen because they are currently the industry standard for dynamic measurements. This type of transducer operates on the principle that quartz crystals emit a charge when strained. From this principle, force, acceleration, and pressure can be accurately measured. While some gages give charge directly, others are equipped with onboard circuits which convert the crystal

charge to voltage for convenience. The benefits of piezo-electronics for dynamic measurement include superior frequency response and resolution as compared to other alternatives.

As always, economics played a role in the transducer selection. Many of the transducers used were also used in the H23A study by Young[4]. This was not just beneficial economically, however, as the survival of these transducers demonstrated their ability to withstand the test conditions satisfactorily.

4.1.2. SELECTION AND INSTRUMENTATION OF TRIAXIAL FORCE GAGES

To measure the flow of sound energy through the suspension springs in the form of structure-borne vibrations, it was necessary to install transducers between the suspension system and the compressor shell. The mechanical path instrumentation which was selected included three triaxial piezoelectric force gages located at each of the compressor mounting springs. The force gages chosen were Kistler model 9251 triaxial gages, operating in charge mode. These gages were re-used from last year's experiment, where they demonstrated their ability to survive the compressor environment.

Triaxial force gages were chosen for the spring mount path transducers for several reasons. Force measurement was chosen over acceleration measurement because accelerometers mounted on the springs or mounts would measure all dynamic response of the support, not just that which passes energy from the mounts to the shell. The process of interpreting acceleration data could become very complicated once all possible motions of the spring and mount are considered. The same would be true of strain gages, which would require the conversion of spring strain data from a particular location on the spring into force data, which would be complicated computationally. Force transducers placed between the spring and mount, on the other hand, directly measure the force passing from the compressor assembly to the shell, regardless of what dynamics cause the force signal. A triaxial gage was chosen because of the triaxial nature of the forces passing through the mounts to the compressor. By treating each axis as an input to the model, it is possible to account for all three components of the mechanical path contributions to the sound output, resulting in a more complete model. Also, triaxial information would be helpful for building a dynamic model of the compressor.

The installation of the triaxial force gages required significant modification to the compressor spring mounts. Both the side-mounts and the top mount required redesign to accommodate the gages. Figures. 4.2-4.5 show the gages, the additional hardware needed, the modification to springs and mounts, and a sketch of the compressor mounts before and after installation.

The hardware required for mounting the force gages was designed to both hold the gage and interact with the spring and shell as the production mounts do. The mating surfaces of the hardware were machined smooth and plane to prevent local areas of force concentration. A small boss was included to mate the force gage and transmit lateral forces to the internal crystal. Both the top and side-mount hardware included a piece to replace the production spring retainers and ensure proper alignment of the springs. The side-mount hardware also included a threaded base for installation of a preload bolt. This was done on the top mount with a standard nut to save space. All hardware pieces were either weighed or weight-estimated, as were the weights of removed material. The net weight increase to the side-mounts was approximately .082 lbf (.36 N) each. The net weight added to the top mount was approximately .107 lbf (.48 N). Table 4.2 itemizes these weights by modification.

Vertical clearance for the side force transducers was created by removing inactive coils from the mounting spring bottoms and cutting the spring post from a production mounting bracket. This provided the necessary space for insertion of the force gage and mounting hardware without changing the static installed position of the compressor within the shell, as can be seen in Fig. 4.4. The threaded mount piece was brazed to the remaining production mounting bracket and the hardware fastened with the preload bolt as seen in Fig. 4.4(b).

Since the top stabilizer spring has no inactive coils and rests on the inside of the compressor shell top, the same approach as the side springs could not be taken. To create the necessary clearance for insertion of the gage, the well in the AC motor cap was

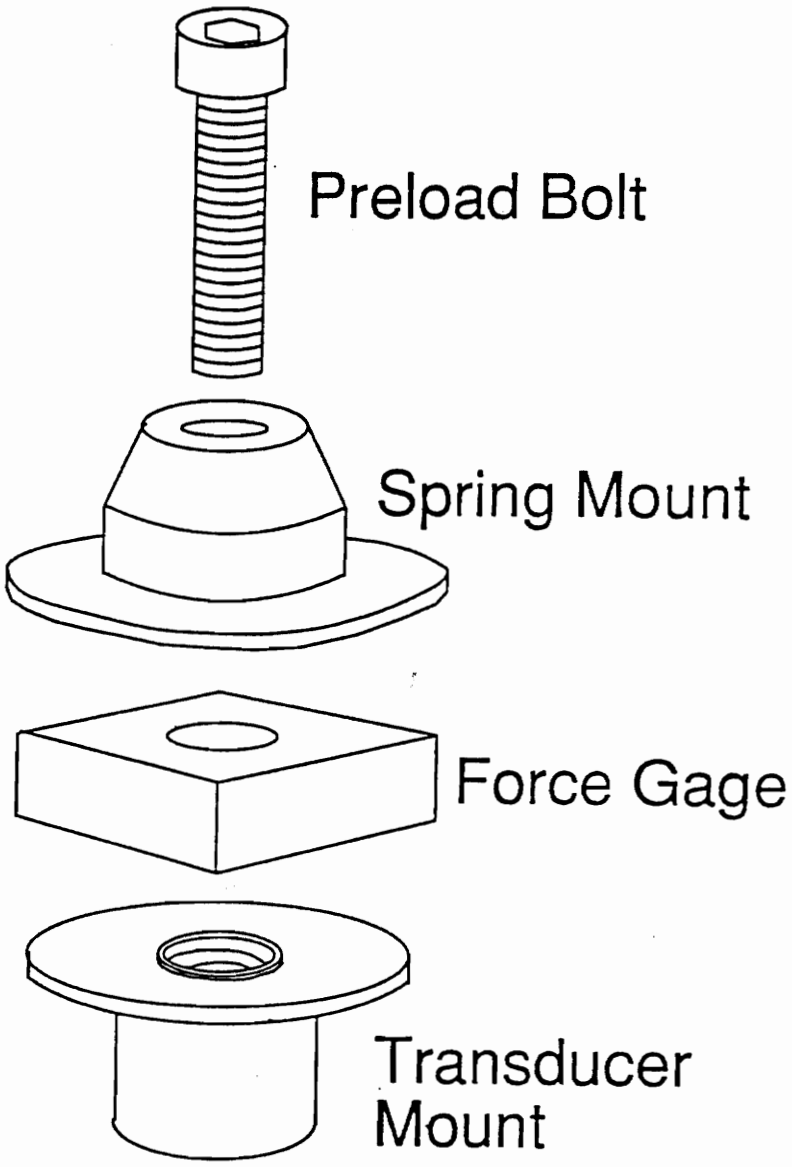

FIGURE 4.2. Hardware for Installation of Side Suspension Spring Force Gage (Adapted from Young[4])

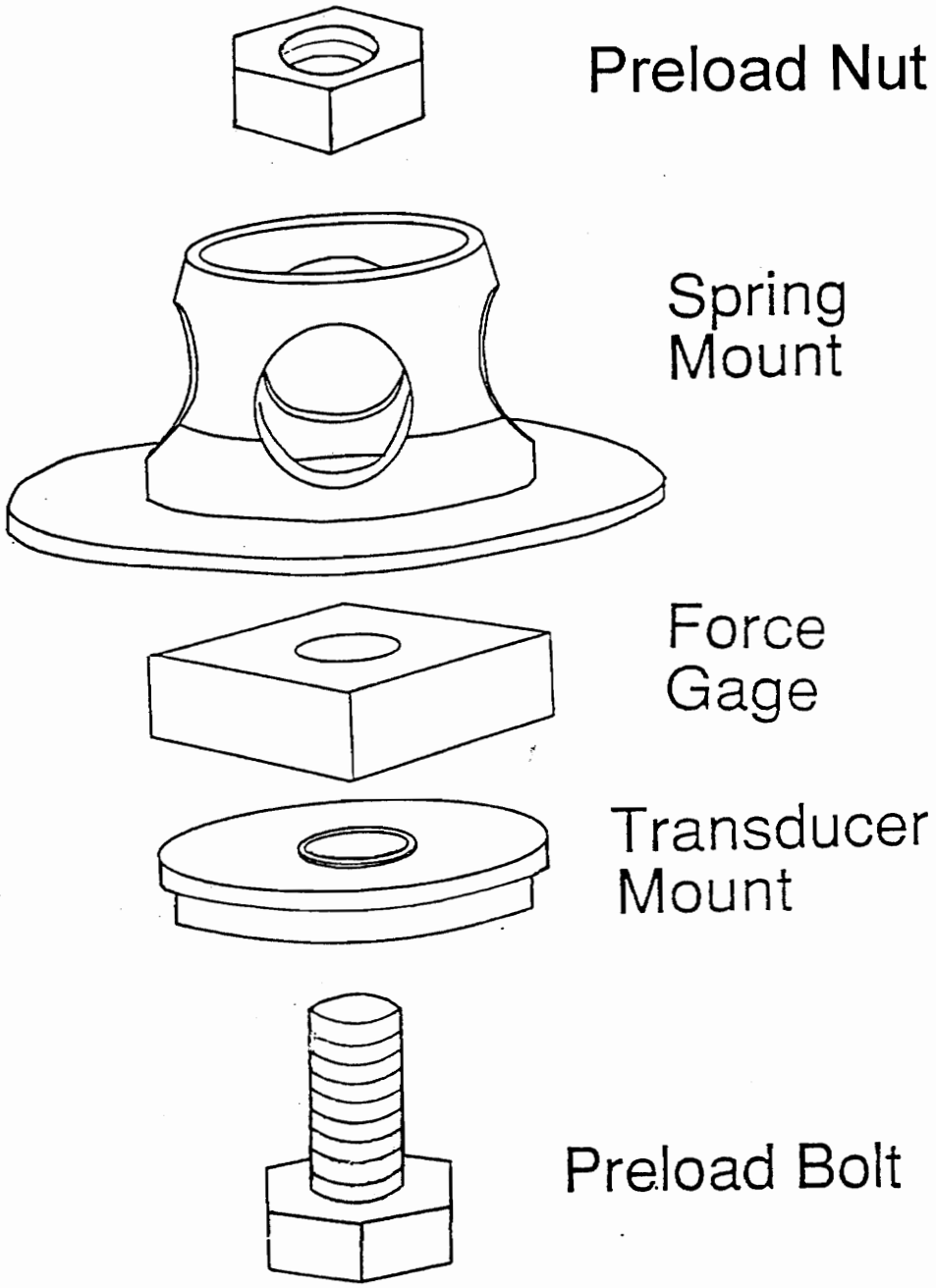

FIGURE 4.3. Hardware for Installation of Top Stabilizer Spring Force Gage (Adapted from Young[4])

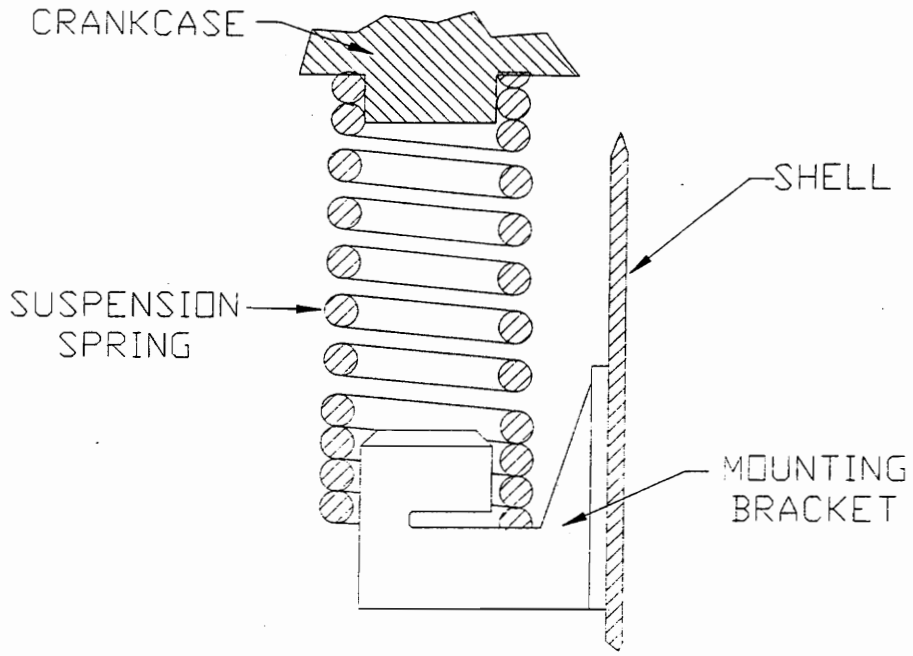

(a) Side Suspension Spring Before Insertion of Triaxial Force Gage

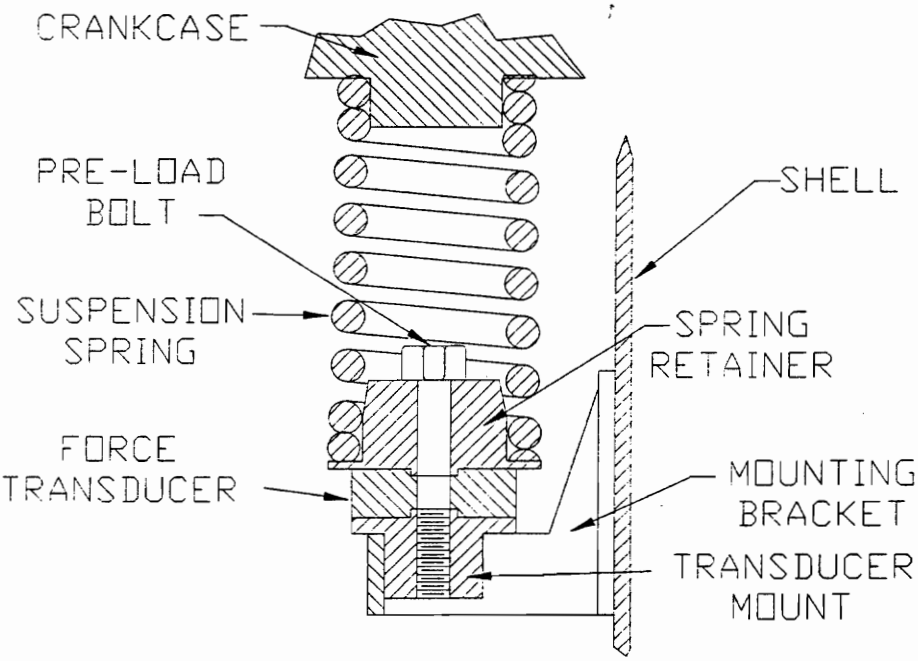

(b) Side Suspension Spring After Insertion of Triaxial Force Gage

FIGURE 4.4. Installation of Side Suspension Spring Force Gage

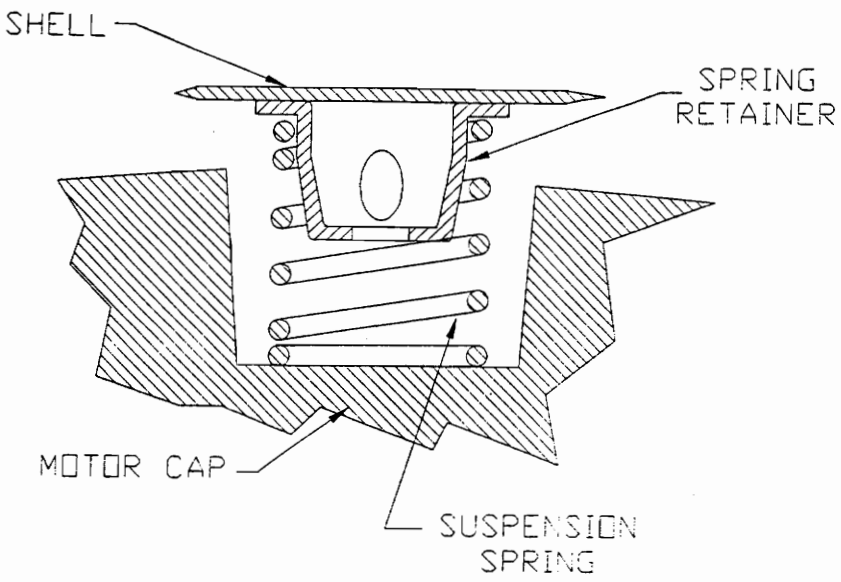

(a) Top Suspension Spring Before Insertion of Triaxial Force Gage

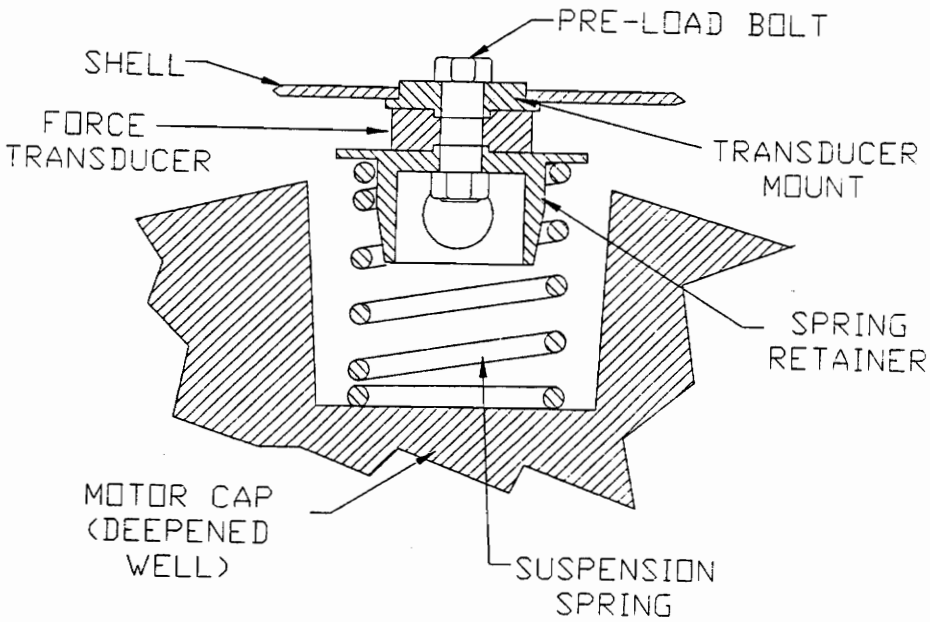

(b) Top Suspension Spring After Insertion of Triaxial Force Gage

FIGURE 4.5. Installation of Top Stabilizer Spring Force Gage

TABLE 4.2. Weight Added to Suspension System During Force Gage Installation

Side Suspension Springs: Modification or Part Added	**Weight**
Triaxial Force Gage	+0.059 lbf (.26 N)
Transducer Mount	+0.037 lbf (.17 N)
Spring Retainer	+0.092 lbf (.41 N)
Preload Bolt	+0.027 lbf (.17 N)
Removal of Inactive Spring Coils	-0.082 lbf (.36 N)
Removal of Original Spring Retainer	-0.051 lbf (.23 N)
Net Weight Added to Each Side Suspension	+0.082 lbf (.36 N)
Top Stabilizer Spring: Modification or Part Added	**Weight**
Triaxial Force Gage	+0.059 lbf (.26 N)
Transducer Mount	+0.040 lbf (.18 N)
Spring Retainer	+0.067 lbf (.30 N)
Preload Bolt	+0.027 lbf (.12 N)
Preload Nut	+0.010 lbf (.05 N)
Hole Drilled in Shell Top	-0.018 lbf (.08 N)
Removal of Original Spring Retainer	-0.078 lbf (.35 N)
Net Weight Added to Top Stabilizer	+0.107 lbf (.48 N)

deepened 0.45 in. (11.4 mm) and a hole was drilled in the shell top to accept the mounting hardware. The transducer mount piece was brazed into this hole along with the preload bolt. This allowed the remaining pieces to be assembled as shown in Fig. 4.5(b). The modifications to the motor cap resulted in a change in enclosed volume from 90.23 cu in. (1479 cu cm) to 88.14 cu in. (1444 cu cm). This reduction in motor cap enclosed volume resulted in an increase in the housing volume by the same amount.

Preload bolts were necessary to allow the piezoelectric crystal to measure tension as well as compression. The recommended preload suggested by Kistler for this model transducer is 5600 lbf (11.4 N). Since these gages are expected to see large transient forces at compressor start-up, a lesser preload was approved by Kistler, provided an in-situ calibration was performed[4]. This was done by loading the installed gages incrementally with calibrated weights and finding the weight/charge curve. Since these gages measure dynamic force, a charge amplifier with a large time constant was used to measure the static force added by the calibration weights. The results of the static calibration are presented in appendix 1. As an added safety feature against crystal damage at start up, stops or "motion-snubbers" were installed near the mounts to limit compressor rocking at start-up.

Although the X, Y, and Z axes of the gages were all parallel, the positive axes for the force gages were not consistent from gage to gage due to physical limitations within the compressor. This problem was corrected by giving some axes of the gages negative calibration factors to change the positive sense of the signal. Figure 4.6 indicates the axes for the triaxial force gages. Note that the triaxial accelerometers discussed in section 4.4.8 utilize a separate and different set of axes from those in Fig. 4.6.

The convention of positive and negative voltages for the forces gages is based upon compressor motion. When the compressor inner assembly moves in a direction corresponding to a positive axis direction as shown in Fig. 4.6, all force gages will register a positive voltage in that direction. For example, when the compressor moves downward, or in the positive Z-axis direction, all three gages will output a positive voltage in their Z-axis signal.

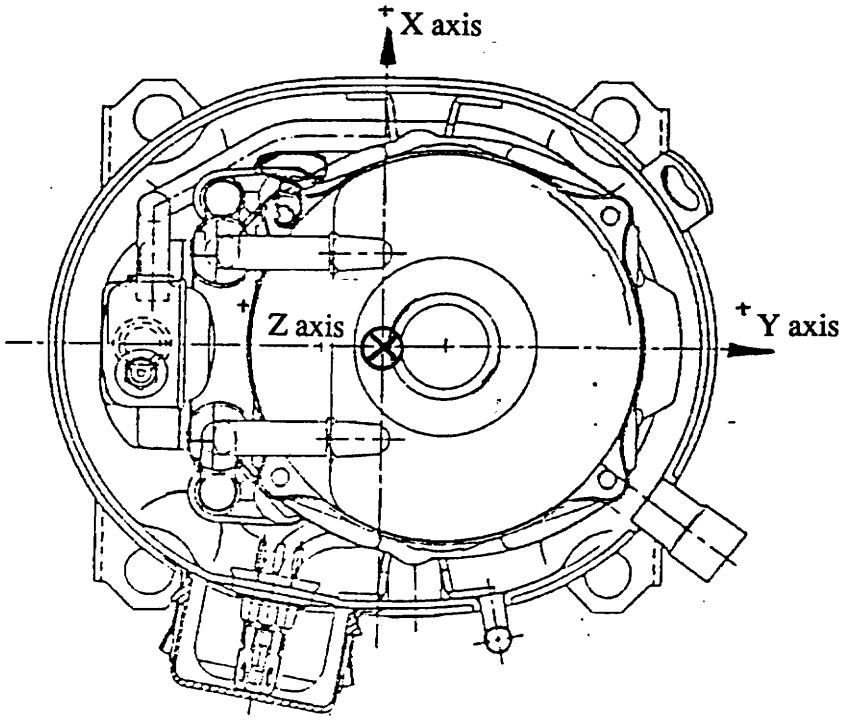

FIGURE 4.6. Triaxial Force Gage Coordinate System

4.1.3. SELECTION AND INSTALLATION OF SHOCK-LOOP ACCELEROMETER

An accelerometer was chosen to measure the transmission of sound energy transmitted through the shock-loop path because it is a tube and cannot be broken for insertion of a force gage without significant effect on compressor operation.

The installation of the shock-loop accelerometer was supervised by David Gilliam of Bristol Compressors. It was placed on the shock-loop tube approximately 3.5 in. (88.8 mm) below the point where the tube attaches to the exhaust muffler (see Fig. 4.1). It was attached via a 0.375 in. (9.53 mm) square block of steel 0.25 in. (6.35 mm) thick with a curved relief to mate the tube. This block was brazed to the tube and the accelerometer attached to the block with a small threaded fastener. The accelerometer was oriented on the side of the tube facing towards the exhaust muffler.

4.1.4. SELECTION AND INSTALLATION OF PRESSURE TRANSDUCERS

To effectively measure the pressure transmission path for correlation with the sound output of the compressor, piezoelectric pressure transducers were selected. These included a PCB113A22 mounted in each of the cylinders, PCB113A24's mounted at the suction and discharge ports and one PCB116A hung inside the shell. All of these transducers were used in the H23A study and performed satisfactorily, demonstrating their resistance to the harsh compressor conditions[4].

The installation of the pressure transducers was supervised by David Gilliam of Bristol Compressors. The cylinder pressure transducers were installed by drilling holes in the cylinders and inserting the gages so as to expose them to the pressure change over the entire piston path. The exhaust pressure transducer was installed similarly, but inserted into a hole in the cylinder head, exposed to the gas discharged by the cylinders. The housing pressure transducer was simply hung in the space between the compressor and the shell, in a location approximately indicated by Fig. 4.1. This location differs from the location in the H23A study, which was hung on the side opposite the muffler. This transducer was wrapped in mylar to protect against AC magnetic fields generated by the motor.

Although pressure transducers can be subject to contamination from secondary signals, the placement and choice of model inputs hopefully minimized any problems in this arrangement. To further protect against contamination error, the cylinder data was never used in any multiple FRF models containing the suction, exhaust, and housing pressure data, thus preventing problems as discussed in section 3.2.4. In conditioned spectral models, the cylinder pressures were always given priority over the suction, exhaust, and housing pressure, once again consistent with the guidelines explained in 3.2.4.

4.1.5. SELECTION AND INSTALLATION OF TRIGGER SIGNAL

To begin simultaneous data collection and to reference the signals to the compression process, a gear was installed on the compressor crankshaft near a stationary magnetic pickup. This arrangement was different than the proximity probe concept used in the H23A study due to it's failure early in the experiment [4]. The 72 tooth gear was selected by R. G. Mitchiner of Virginia Tech who likewise supervised its installation. Prior to installation, this gear had one tooth removed to indicate the top dead center of the piston motion. A circuit was then built by Billy Shepherd of Virginia Tech to convert this missing pulse in the square pulse train to a trigger signal. This trigger signal is shown in Fig. 4.7. As can be seen, this signal provides a positive slope once per revolution of the crankshaft, or once per the compression cycle. Appendix 2 presents the circuit which provides this signal from the gear teeth input signal.

The gear was installed by machining a flat surface on the crankshaft near the bottom of the compressor shell. The gear was cut in half and brazed to this machined surface. The shaft location was chosen near the bottom of the shell to maximize the distance from the AC motor, thus minimizing the magnetic pickup's susceptibility to electromagnetic fields. It was also at near the shell bottom that a large amount of material was present on the crankshaft for machining.

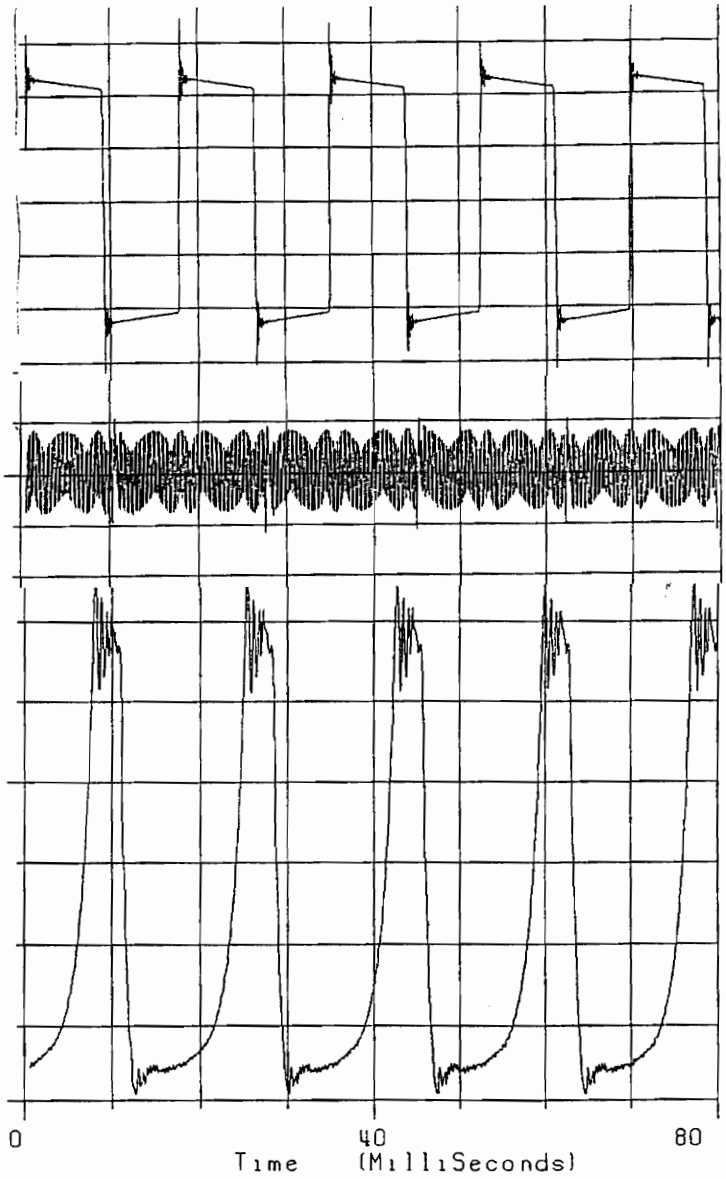

FIGURE 4.7. Trigger Signal

4.1.6. INSTALLATION OF TRANSDUCER CABLES

The hermetically sealed compressor presents a problem for installation of internal transducers. Namely, how can signals be transmitted to the outside of the compressor without losing internal pressure and/or weakening or drastically altering the shell? The cabling system devised for this experiment was designed to change the shell dynamics minimally while maintaining internal pressure and preserving shell strength.

The final design consisted of commercially available hermetically sealed cable pass-throughs; 9 located on the shell itself and the remainder located on a bulkhead attached to the shell by a braided steel tube. Figure 4.8 is a photograph of the installed cabling bulkhead. The bulkhead design was adopted to allow many cables to pass through a single hole in the shell, minimizing the affect on the dynamic response. The hole for the steel braided tubing was cut on a stiff corner of the shell, a nodal line for all modes in the frequency range of interest [2]. The pass-throughs located on the shell itself carry the signals of the triaxial force gages. These are also located on corners of the shell. These cables were not terminated at the bulkhead because they carry charge signals, which can become noisy through cables of excessive length or cables which may move during data acquisition.

The concern of additional volume added by the bulkhead was addressed by the fact that the cables themselves filled the tube and bulkhead almost to capacity. This fact also prevented the bulkhead from acting as resonator during compressor operation.

4.1.7. MICROPHONE SELECTION

The microphone chosen for the sound measurements was a Bruel & Kjer omni-directional microphone with a 0.5 in. (12.7 mm) model 4166 diaphragm, suitable for the frequency range of interest here. After testing, the microphone was calibrated via a piston phone and the calibration factor found to be 0.0138 psi/V (.0952 kPa/V). This on-site calibration factor was used in all post processing calculations and thus all data presented in the results section is based upon this calibration value.

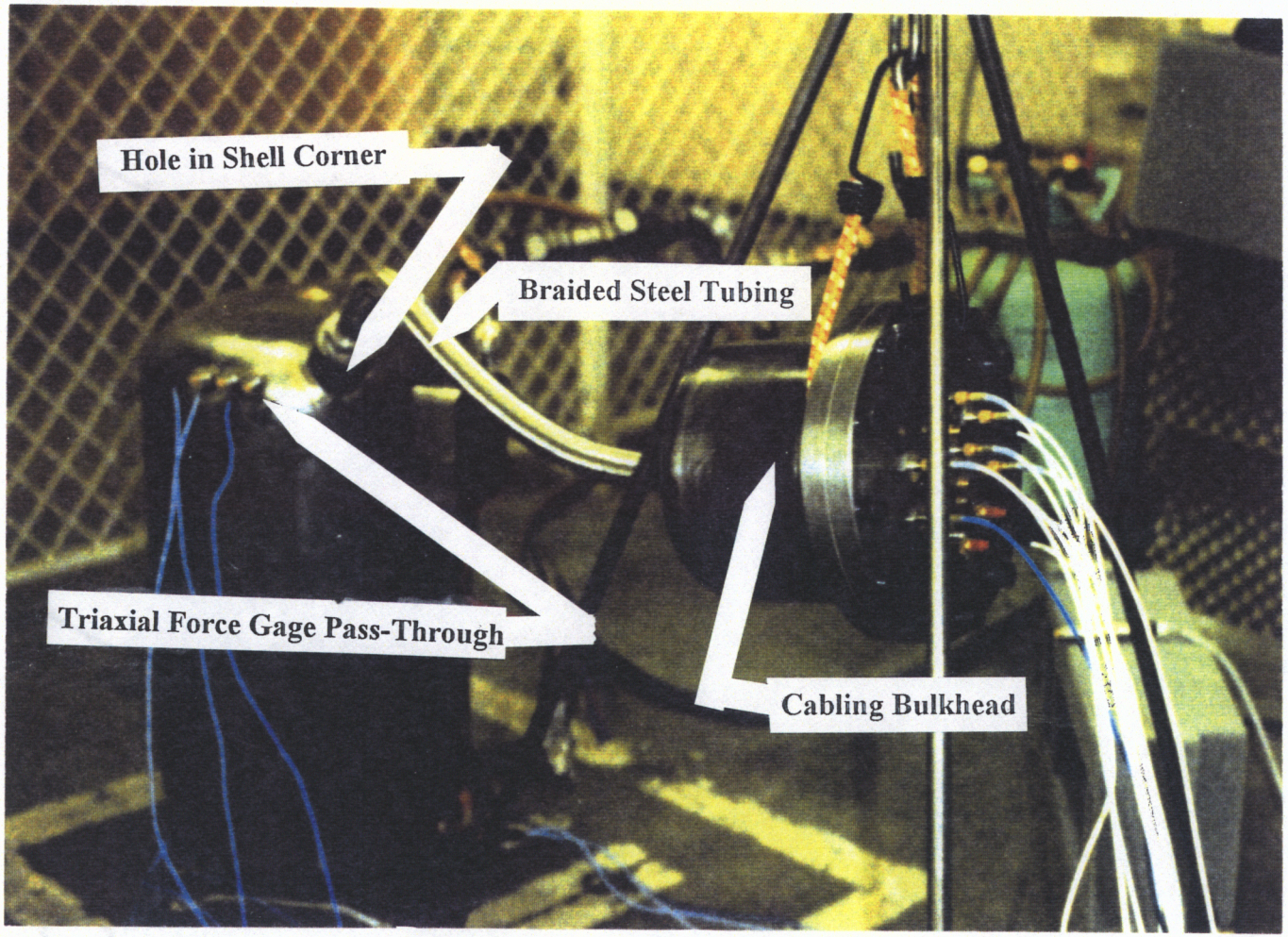

FIGURE 4.8. Cabling Bulkhead

4.1.8. SELECTION AND INSTRUMENTATION OF TRIAXIAL ACCELEROMETERS

As mentioned in section 4.1, two Kistler 8792A500 triaxial accelerometers were installed on the compressor to collect data for a dynamic model of the H25A compressor. Although no data from these accelerometers was used in the sound transmission path study, their installation is covered here for completeness.

The object in installing these accelerometers was to place them in rigid areas of the compressor as far from one another as possible and not in contact with the compressor shell. These goals were consistent with the purpose of these transducers: to measure the three-dimensional translations and rotations of the compressor assembly during compressor operation.

Figure 4.1 shows the locations of the two accelerometers within the compressor. The top accelerometer was installed on a small metal platform connected to the motor cap via the long bolt connecting the motor to the crankcase. For this installation, a longer bolt was simply used in place of the standard bolt and the a hole was drilled in the platform so the bolt could pass through it and secure the accelerometer to the compressor. The bottom accelerometer was installed to the crankcase via another steel platform, attached to the crankcase by drilling a small hole in the crankcase for a small bolt.

Since the areas where the accelerometers were attached to the compressor involved non-orthogonal surfaces, the mounting platforms were designed to compensate for this and align the accelerometers as best possible. Final alignment was done by hand and no estimate is available as to the uncertainty of the axis alignment. The axes for the accelerometers is shown in Fig. 4.9. Note that due to geometrical constraints, these are different than the axes for the triaxial force gages.

4.2. EFFECT OF INSTRUMENTATION ON H25A COMPRESSOR

In order to assess the effect of transducer installation on the dynamic response of the compressor, several separate tests were performed. The first test consisted of

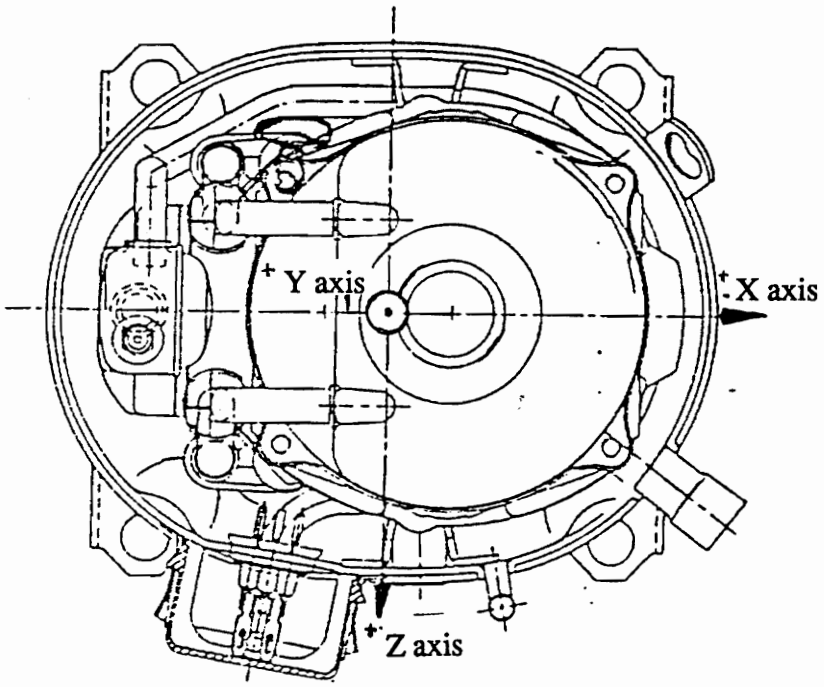

FIGURE 4.9. Triaxial Accelerometer Coordinate System

determining the frequency response function (FRF) of a compressor shell before and after installation of the cable bulkhead. The second test consisted of comparison of the FRF of the completely instrumented compressor with the FRF of a production compressor. The final test consisted of efficiency and noise emission measurements of the instrumented compressor, performed by David Gilliam of Bristol Compressors at their facilities. The results of these tests were compared to efficiency and noise emission averages for production compressors.

4.2.1. EFFECT OF CABLING BULKHEAD

To determine the effect of the cabling bulkhead described in section 4.1.6 and depicted in Fig. 4.8, a compressor shell (not the actual shell used in the multiple input experiment) was tested to determine its FRF before and after installation of the bulkhead. The FRF's were determined by exciting the shell with a modally tuned PCB impact hammer, and measuring the response of the shell at various locations. Response was investigated up to 2000 Hz with a resolution of 5 Hz. The results shown here are the result of averaging 10 blocks of data consisting of 1024 data points. In the collection of response data, an exponential window was used. The point of impact and the point of response measurement for these tests were both near the top of the compressor "short side" just below the suction tube, about four inches apart.

Figure 4.10(a) shows the FRF (mobility) prior to installation of the bulkhead. Figure 4.10(b) shows the FRF after installation. As can be seen, no frequency peak in the original FRF exceeds a shift of 5 Hz after installation of the cabling bulkhead. Although some slight changes can be seen in the FRF topography, these changes are best described as negligible.

4.2.2. EFFECT OF COMPLETE INSTRUMENTATION ON DYNAMIC RESPONSE

After completion of H25A instrumentation, several FRF's of the compressor were experimentally determined for comparison to FRF's of a production H25A compressor (not the identical compressor unit). The FRF's were acquired in the same manner as those described in the previous section, and a few typical FRF's are presented in Figs. 4.11-4.13. For Fig. 4.11, the compressor was impacted on the top of a compressor "short side" and

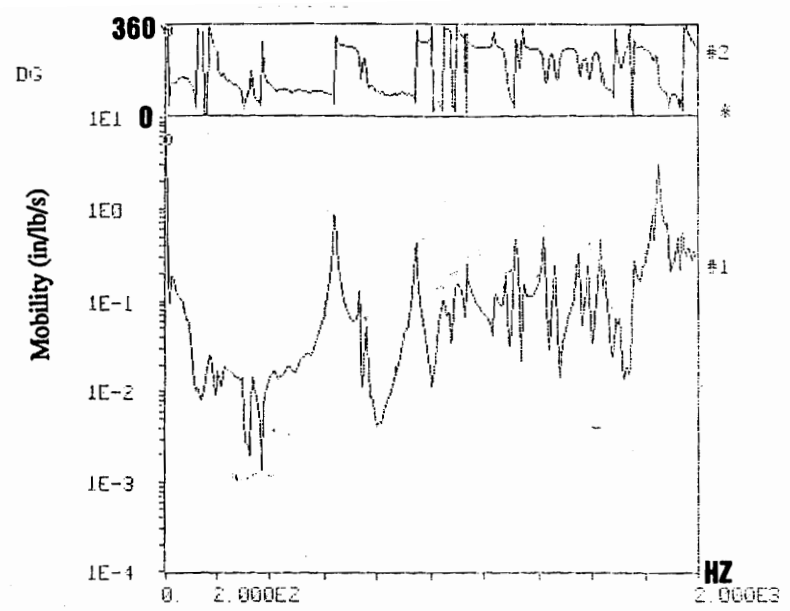

(a) Mobility FRF of Shell Before Cabling Bulkhead

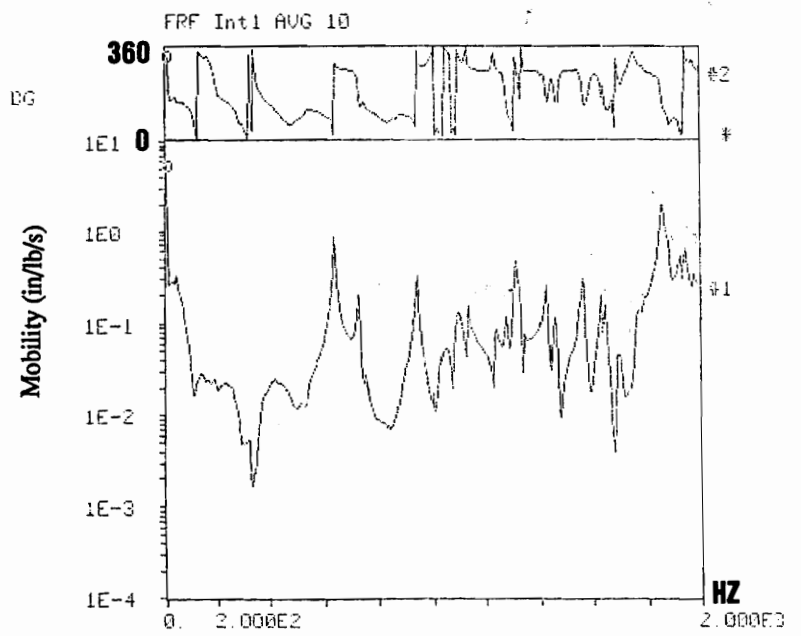

(b) Mobility FRF of Shell After Cabling Bulkhead

FIGURE 4.10. Mobility FRF of Shell (a) Before and (b) After Cabling Bulkhead (1 in/s/lb = 5.710 mm/s/N)

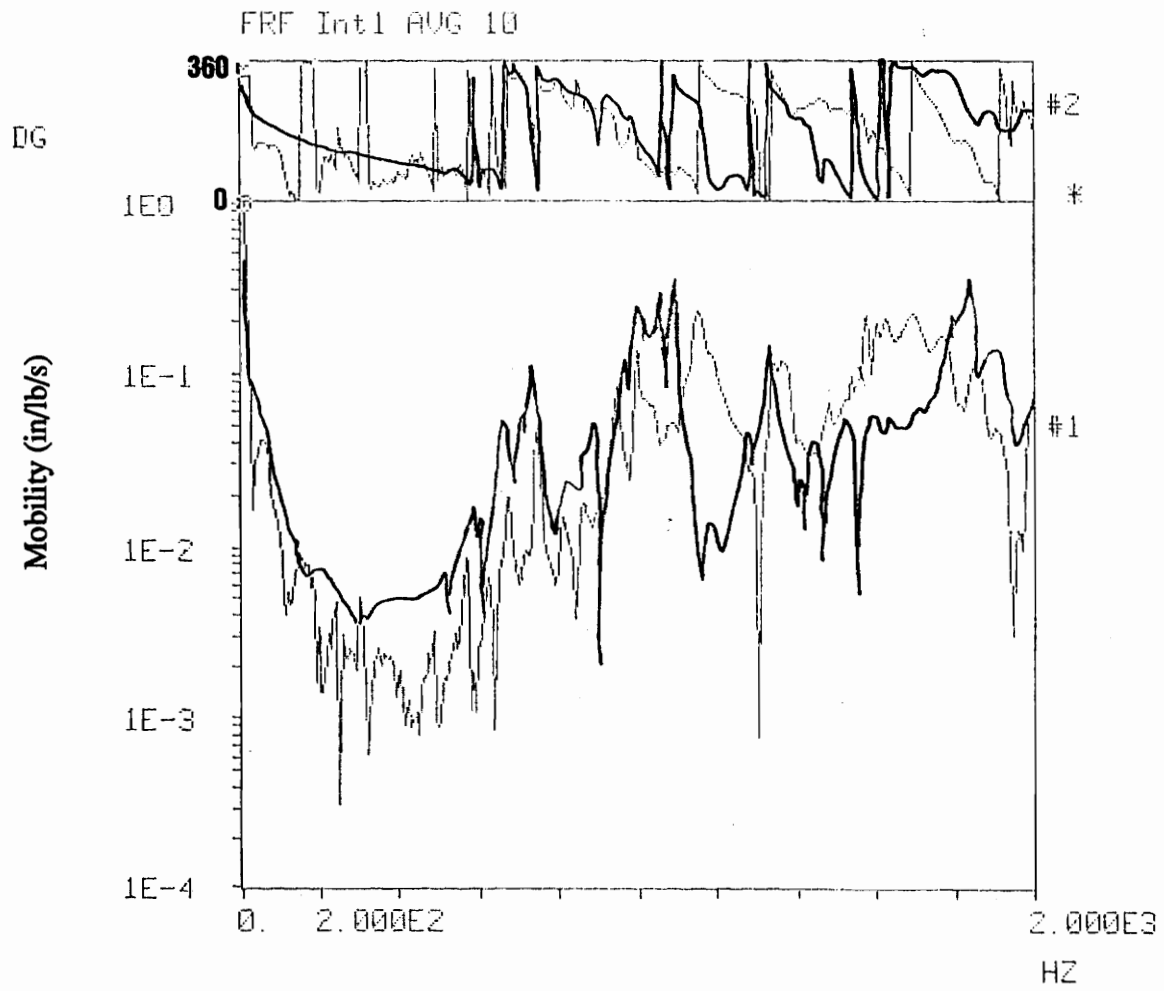

Mobility FRF Before Instrumentation **Mobility FRF After Instrumentation**

FIGURE 4.11. Mobility of Compressor After Instrumentation: Test 1
(1 in/s/lb = 5.710 mm/s/N)

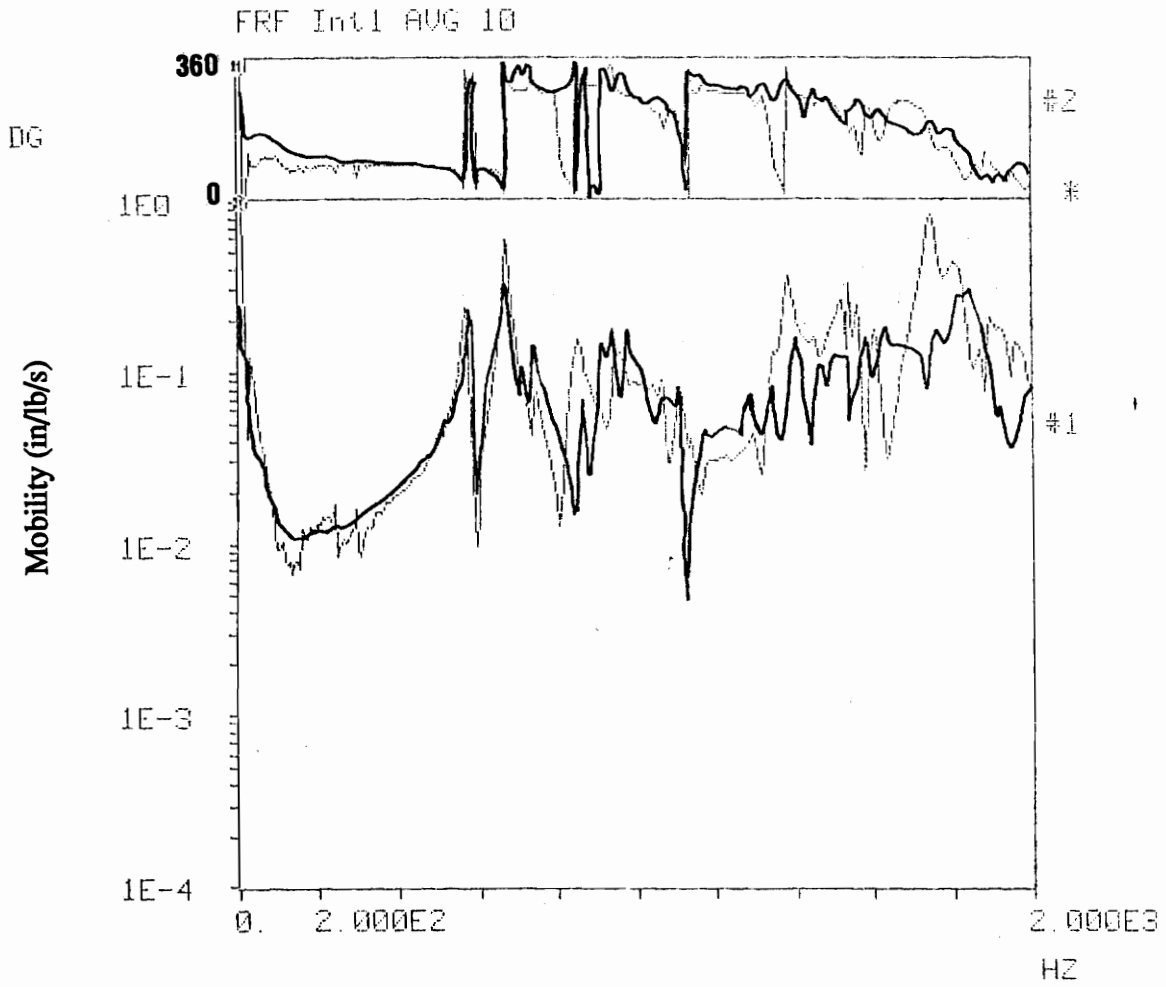

Mobility FRF Before Instrumentation **Mobility FRF After Instrumentation**

FIGURE 4.12. Mobility of Compressor After Instrumentation: Test 2
(1 in/s/lb = 5.710 mm/s/N)

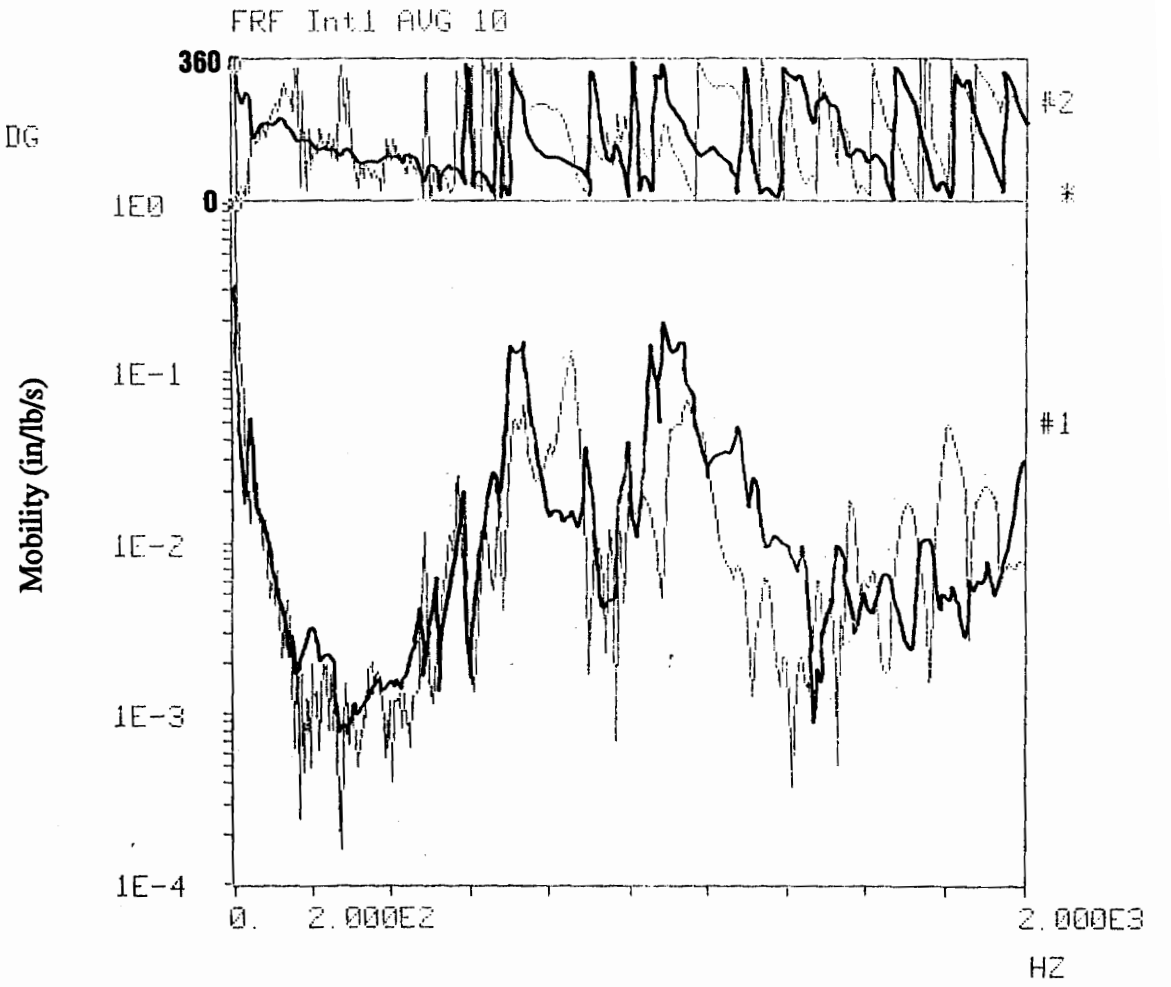

Mobility FRF Before Instrumentation **Mobility FRF After Instrumentation**

FIGURE 4.13. Mobility of Compressor After Instrumentation: Test 3
(1 in/s/lb = 5.710 mm/s/N)

the response measured on the bottom of a long side. For Fig. 4.12, the compressor was impacted at a point at the bottom of the opposite long side and the response measured on the upper half of a compressor short side. Figure 4.13 shows an FRF when the compressor was impacted near the center of the compressor top and the response measured at the bottom of a compressor short side.

As can be easily seen, the instrumentation of the H25A compressor did in fact result in a change in its dynamic response. It is difficult to draw general conclusions from these FRF's, but a few impressions can mentioned. First of all, it can be stated that the FRF's of the side of the instrumented compressor resemble a production compressor more than the FRF's of the instrumented compressor top. Secondly, the low frequency range (up to around 800 Hz) appears to be the least effected, particularly in the case of the compressor sides. In this frequency region, the natural frequencies appear to be similar to that of a production compressor and the response equal or lower than a production model. In the next frequency range, 800-1500 Hz, the FRFs generally exhibit some frequency scrambling and, in general, a lower response level after instrumentation. Lastly, in the range above 1500 Hz, most of the FRF's investigated show responses higher after instrumentation, along with a loss in frequency information.

In many ways, these conclusions match those found in the H23A project. After instrumentation, a lower response in the 900-1000 Hz region of the compressor FRF was seen after instrumentation[4]. This similarity is not surprising considering the similarity of instrumentation schemes between the H23A and H25A projects. Note that a statistical study was performed on empty, unpressurized H25A shells and it was determined that resonant frequencies from shell to shell are not identical (see appendix 3). In view of this, it is expected that the resonances of complete compressors could vary significantly from compressor to compressor as well.

4.2.3. EFFECT OF INSTRUMENTATION ON EFFICIENCY AND SOUND OUTPUT

To assess the effect of the instrumentation on the compressors operation, David Gilliam of Bristol Compressors supervised several tests of the instrumented H25A under operating conditions at their plant test facilities. These tests included anefficiency/capacity test and two sound output tests.

The efficiency/capacity test indicated a running capacity of 60,483 BTU/hr (17.7 kW) and an efficiency rating of 11.1 BTU/hr/Watt (3.25 W/W). These values, when compared to the usual values of 61,000 BTU/hr (17.9 kW) capacity and 11.2 BTU/hr/Watt efficiency rating (3.28 W/W), seem to indicate that the capacity and efficiency of the instrumented compressor were not dramatically reduced due to the installation of the test transducers.

The sound output tests were compared to sound tests of regular H25A models which typically run at 77 dBA re 2.9×10^{-9} psi (20×10^{-6} Pa) average. The first test of the instrumented compressor resulted in a dBA average of 73, indicating a rather quieter machine. A second test in another acoustic room indicated a sound level of 76 dBA average. Although the repeatability of the test process makes it difficult to exactly quantify the amount of sound reduction resulting from the instrumentation of the compressor, it seems evident that the instrumented compressor does run quieter than production models. This fact is supported by the fact that the instrumented H23A, which shared many instrumentation concepts with the H25A, ran about 4 dBA quieter than its production equivalent[4].

4.3. COMPRESSOR TEST SETUP

Figure 4.14 is a photograph of the instrumented H25A compressor as it was installed prior to data collection. The compressor was set on its standard rubber mounting grommets and placed on a hard concrete floor. Its suction and discharge lines were attached to a compressor test bench (or "load bank") which was provided by Bristol Compressors. This bench (covered by an acoustically treated box in the figure) provides the proper electrical power to the unit (three phase in this case), provides a load for the compressor to work against, and provides gages and valves for monitoring and controlling suction and exhaust pressures. The compressor/test bench system was charged with refrigerant (R-22) to its standard load. As can be seen in the figure, the instrumentation cables from the compressor were routed to their amplifiers and then into a Zonic System 7000 data acquisition unit. This unit was then connect via ethernet cable to a Hewlett-Packard HP375 computer running Zonic Zeta software to control the System 7000.

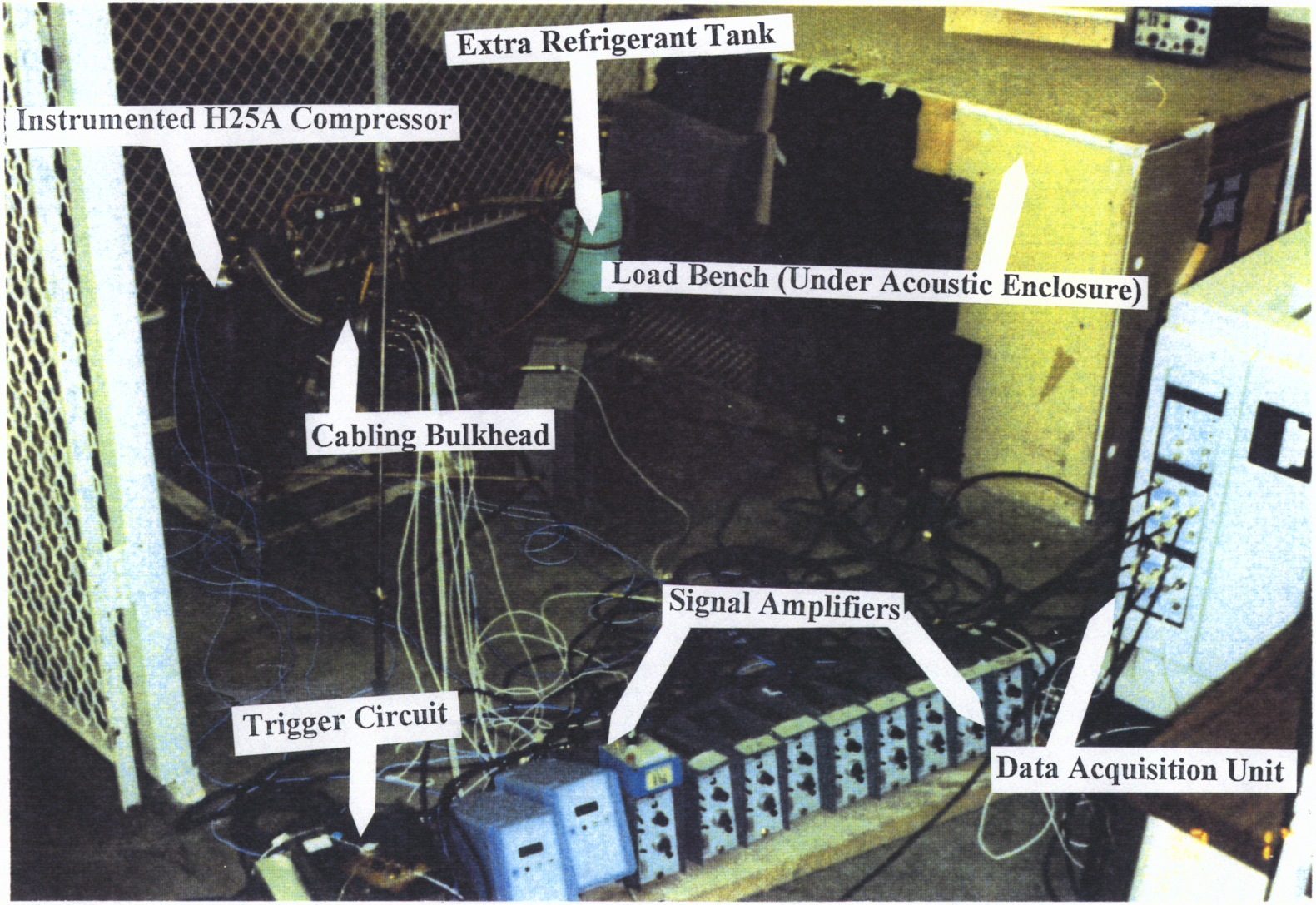

FIGURE 4.14. H25A Test Setup

To provide information about sound radiation from the different surfaces of the compressor, four tests were conducted with four different external microphone locations. These locations are shown in Figs. 4.15-4.16. The first test was conducted with the microphone located perpendicular to the compressor "long side", 2 ft (.61 m) away and at a height equal to the compressor "belt line" weld. The second test was conducted with the microphone perpendicular to the "short side", at the same height and distance. The third test was conducted with the microphone as nearly perpendicular to the compressor top as possible, 2 ft (.61 m) away as shown. The final test was done with the microphone located 6 ft (1.8 m) away at approximate ear level. This last test was hoped to provide average sound data for the compressor which would not be dependent upon the different radiation from the different compressor surfaces. It would however, due to its distance, be subject to more time-delay error and lower signal-to-noise ratio.

4.4. DATA COLLECTION PROCEDURE

Before collecting any transducer data, the compressor was turned on and allowed to reach standard operating conditions of approximately 77 psi (530 kPa) suction pressure (gage) and 290 psi (2000 kPa) discharge pressure. In addition, the compressor suction line temperature was checked to verify the inlet refrigerant was 65° F (18.3° C), as suggested by Bristol Compressors. This indicated the compressor was operating as it would in a typical commercial application.

Once the compressor reached its standard operating conditions, the Zonic System 7000 data acquisition unit was set to trigger upon the signal from the trigger circuit. At this time, the unit began acquiring time data blocks of 1024 data points at a sampling rate of one sample every 0.0781 ms. The maximum analysis frequency with this sample rate was 5000 Hz with a spectral resolution of 12.5 Hz. In all, 100 data blocks were acquired for each microphone location. Each test took approximately twenty minutes. The test data was saved on a throughput magnetic disk which saves the data unaveraged in the time-domain. In this manner, the data could be replayed and averaged in the time-domain or frequency domain with various post processing options.

The Zonic System 7000 unit itself was used to time average the data from each transducer. Spectra with phase information were then computed from these time averaged

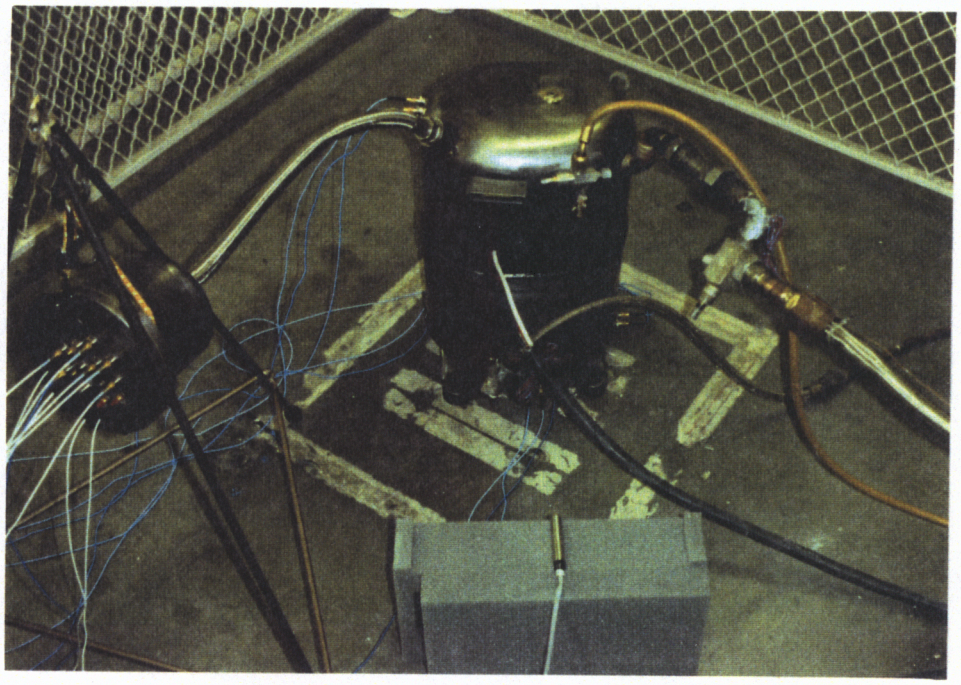

(a) "Long Side" Microphone Location

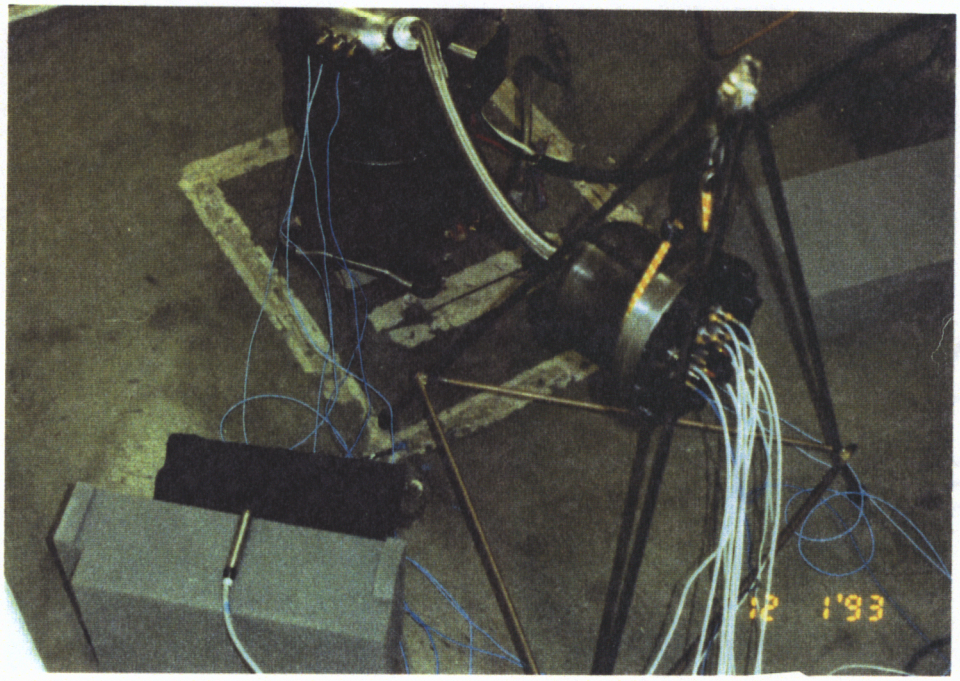

(b) "Short Side" Microphone Location

FIGURE 4.15. Long Side and Short Side Microphone Locations

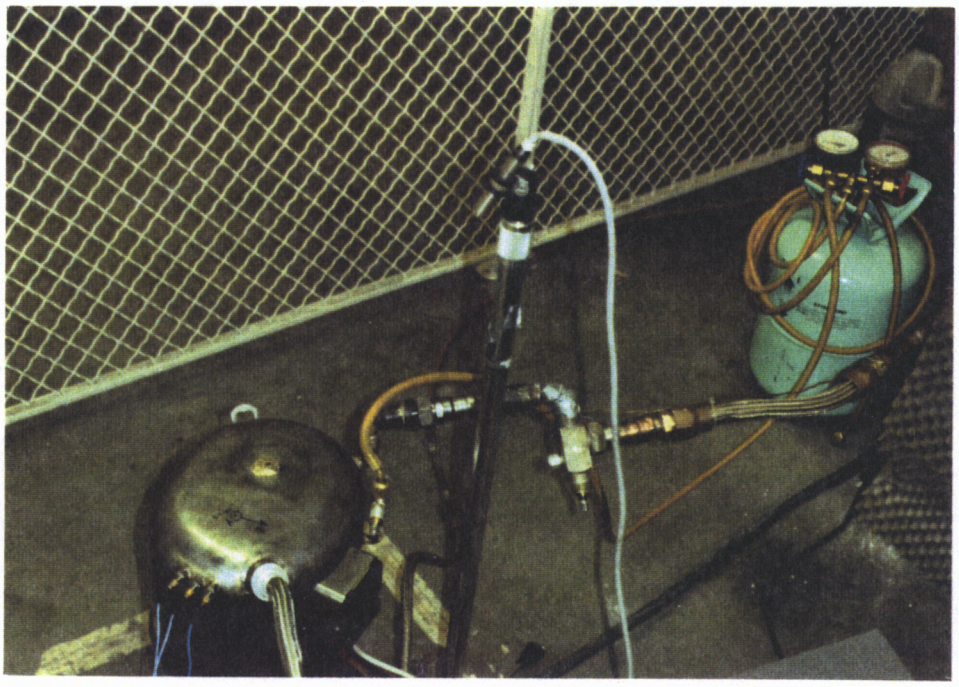

(a) "Top" Microphone Location

(b) "Far-Field" Microphone Location

FIGURE 4.16. Top and Far-Field Microphone Locations

signals by performing a fast Fourier Transform of the time averaged blocks. The advantage to averaging in the time-domain and computing spectra from these time averaged blocks (as opposed to frequency-domain averaging) is the ability to extract phase information in the frequency domain. This phase information is useful when comparing the test data to analytical predictions of dynamic forces made by the dynamic modeling team of this project. Since the governing equations for MISO systems assume frequency averaged data, however, the spectra generated from the time averaged blocks were not used to develop the MISO model. Rather, the blocks were re-computed as frequency-averaged auto spectra.

To conduct the multiple input/single output analysis, the data was converted to IDEAS VI compatible ADF time history files. This conversion would allow the data to be processed by the mechanical engineering software IDEAS VI. Within IDEAS VI, routines for compiling spectral matrices and determining multiple reference FRF's and coherences are easily accessed.

CHAPTER 5.
RESULTS OF H25A COMPRESSOR TEST

This chapter presents the results obtained from the testing of the instrumented Bristol H25A compressor. Examples of averaged time and frequency data from the transducers are shown, along with sound level spectra from the various microphone locations. Lastly, results from various multiple-input/single-output analyses are presented.

5.1. TIME- AND FREQUENCY-DOMAIN TRANSDUCER DATA

As mentioned in chapter 4, time-domain transducer data was collected for each of the transducers listed in table 4.1. For the multiple-input study, this data was frequency-domain averaged and compiled into a spectral matrix as discussed in section 2.3.1. For the purpose of comparison of experimental data with the analytical dynamic compressor model, it was necessary to time average the force gages, cylinder pressures, suction and exhaust pressures, and compressor accelerations. This time-averaged data could then be transformed into complex frequency-domain data via Fourier transform (the advantage being that this spectrum would retain phase information and allow for a phase comparison with the analytical force models).

Appendix 4 contains a complete set of transducer data plots. These are presented as time-domain traces and phase and magnitude spectra. In the computation of all frequency spectra a Hanning window was used. For other data acquisition parameters, see section 4.3.

5.1.1. FORCE GAGE DATA

Figure 5.1(a) shows the time-domain data for the top spring force in the x-axis direction (see Fig. 4.6 for axes definition). This trace is typical of all of the force gages in many respects. The fundamental period can be seen to be 0.0173 s, corresponding to a fundamental frequency of 57.8 Hz, the operating speed of the compressor during the test. In this and all other transducer data, about four and one half fundamental periods of data

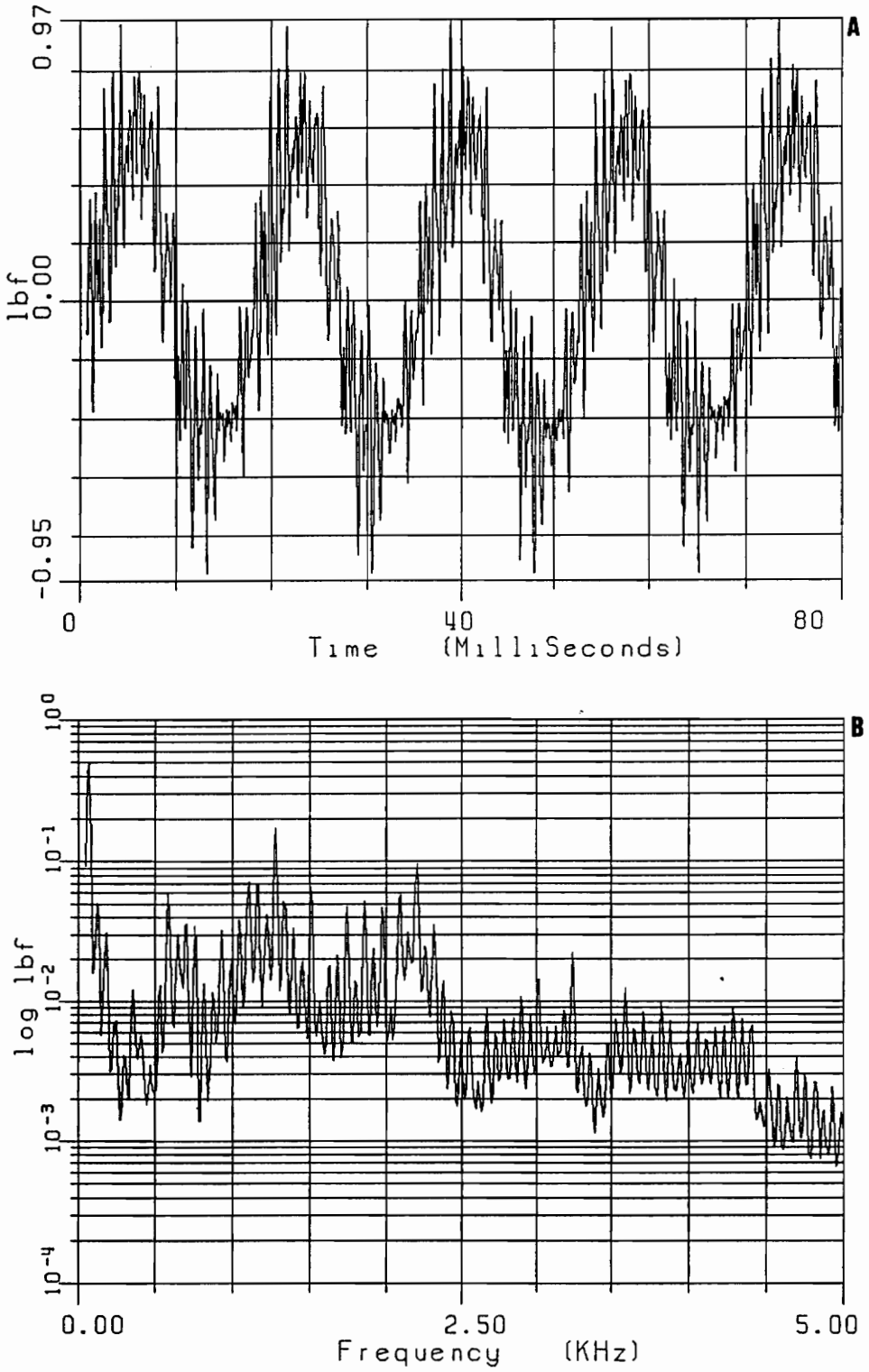

FIGURE 5.1. (a) Time- and (b) Frequency-Domain Top Spring Force Data: X-Axis (1 lbf = 4.448 N)

were collected. The force in this gage fluctuates between roughly 0.5 lbf (2.2 N) (tension of gage) and -0.5 lbf (-2.2 N) (compression of gage). This magnitude may be considered typical as no gage exceeded a force of 2 lbf (8.9 N) in either tension or compression. Also typical of this gage is the presence of high frequency components, which can be seen as small, repeated fluctuations on the fundamental period wave. The periodic nature of these high-frequency components indicate the stationarity of the data, which was assumed in all analysis of the data.

In Fig. 5.1(a) a small DC offset is present. This was seen on some of the other data, and is attributed to a slight mis-calibration of the charge amps or the data acquisition unit. Since this data is dynamic, and since the DC offset is not major, this offset was not corrected for in data post-processing.

In Fig. 5.1(b), the spectrum up to 5 kHz of the same gage is shown. This plot is also typical of all of the force gages in the several ways. First of all, the dominant frequency response occurs at 57.8 Hz, or the fundamental frequency. This is true for all of the force signals except the right gage's y-axis force, in which the fundamental frequency is second to the first harmonic in magnitude. The second multiple of the fundamental possibly indicates a force related to the piston forces (which would occur twice per crankcase revolution) as opposed to some rotating unbalance (which would occur at the fundamental frequency).

5.1.2. PRESSURE GAGE DATA

Figures 5.2-5.5(a) show the time-domain data for the pressure transducers within the compressor. Since these gages measure dynamic pressure only, the zero value of the plots' y-axis corresponds to the static pressure on the gage, not zero pressure as shown. Static pressures were monitored during the test to ensure standard operation of the compressor and serve as the zero point on the plots. For the suction pressure, the zero pressure corresponds to approximately 77 psi (53 kPa). For the exhaust this value is approximately 290 psi (2000 kPa). The housing pressure zero should be 77 psi (53 kPa), as the compressor suction line is open to the compressor housing. The zero of the cylinder pressure plots should be near 110 psi, the static pressure in the housing after

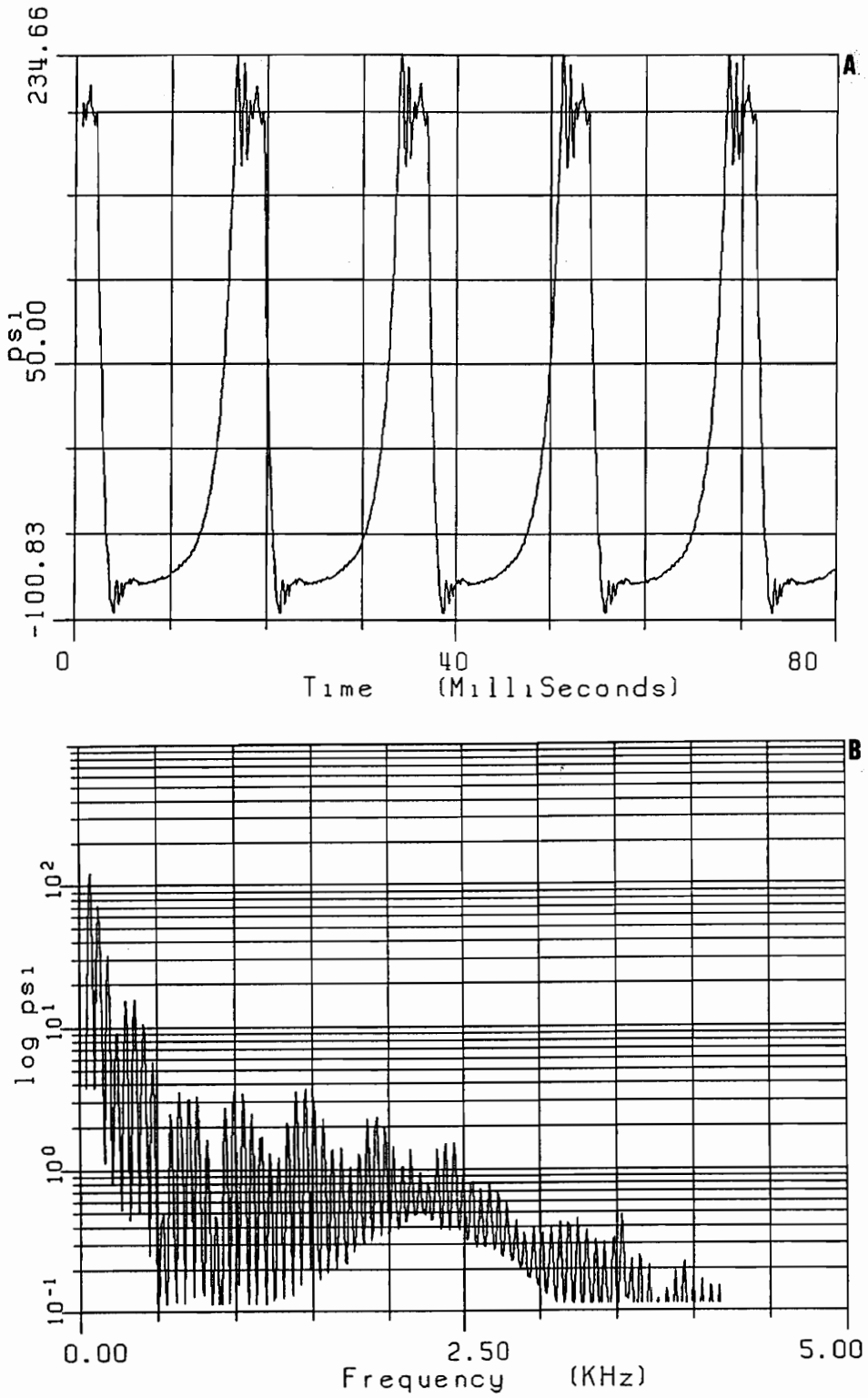

FIGURE 5.2. (a) Time- and (b) Frequency-Domain Bottom Cylinder Pressure Data (1 psi = 6894.8 Pa)

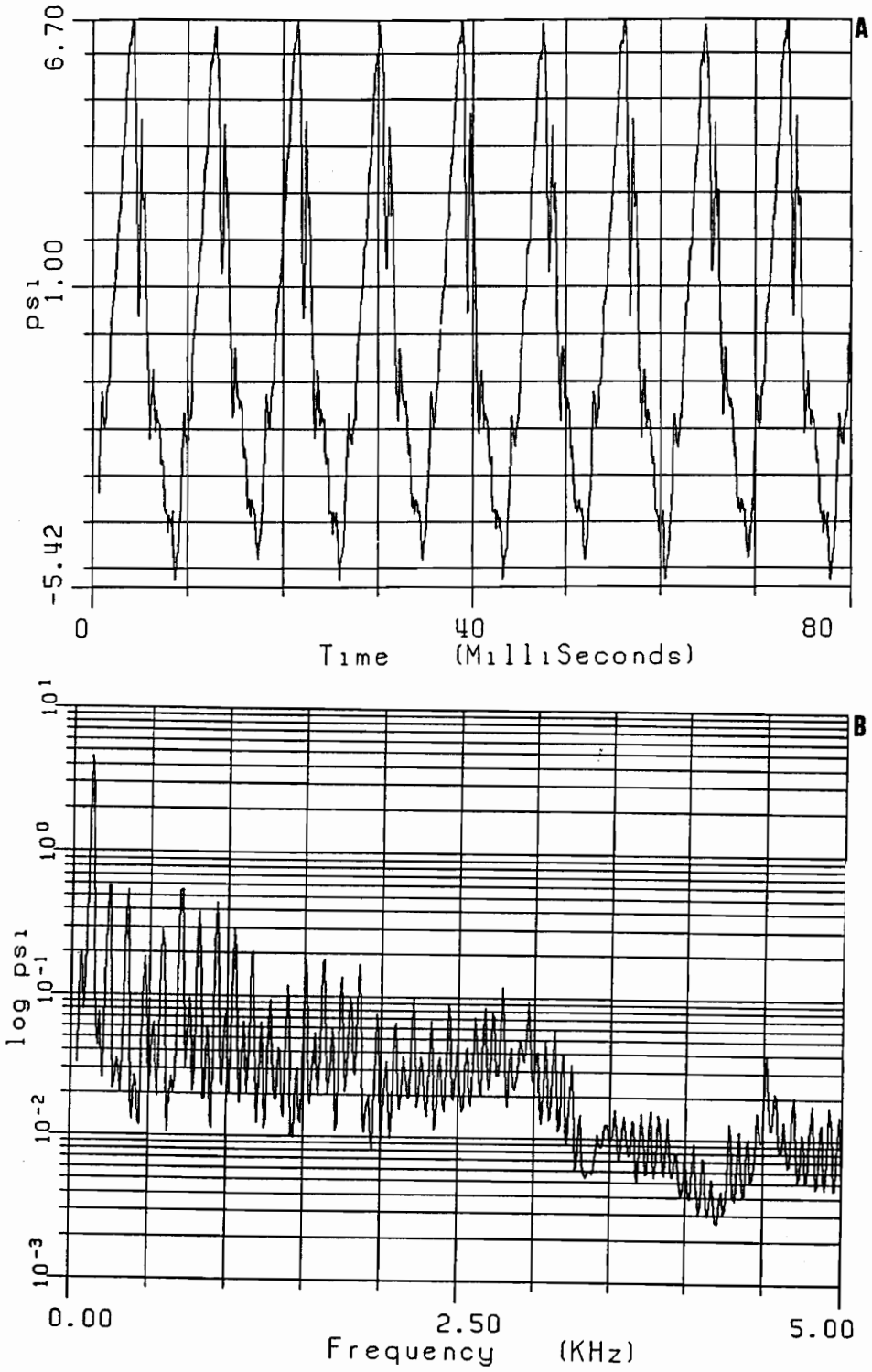

FIGURE 5.3. (a) Time- and (b) Frequency-Domain Suction Pressure Data (1 psi = 6894.8 Pa)

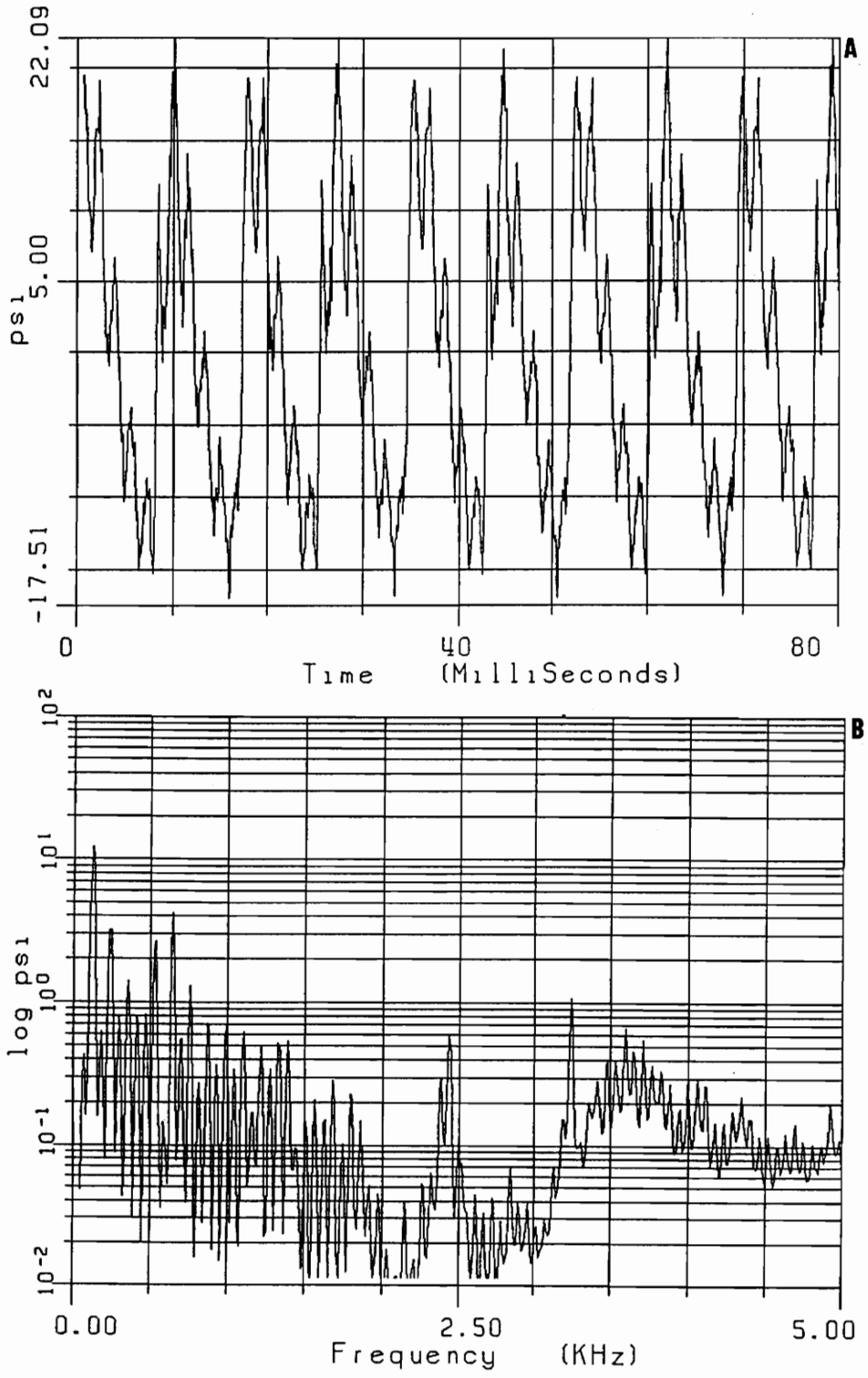

FIGURE 5.4. (a) Time- and (b) Frequency-Domain Exhaust Pressure Data (1 psi = 6894.8 Pa)

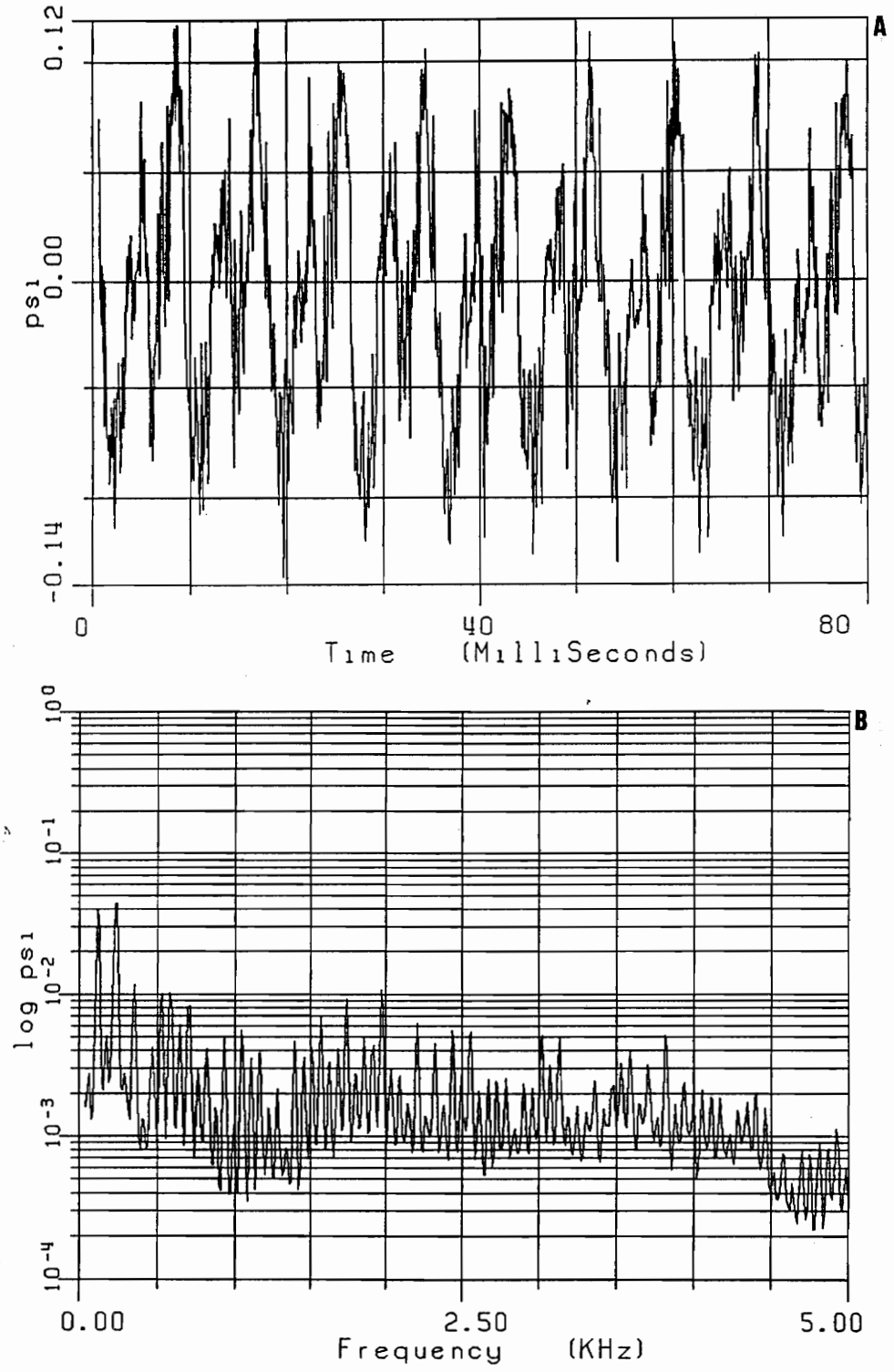

FIGURE 5.5. (a) Time- and (b) Frequency-Domain Housing Cavity Pressure Data (1 psi = 6894.8 Pa)

being charged with refrigerant. On the cylinder pressure traces, the effect of the valves impacting their seats can be seen as the pressure fluctuations at maximum pressure. These fluctuations cause the maximum ΔP across the cylinder pressure curve to exceed the expected range between maximum and minimum cylinder pressure.

In Figs. 5.2-5.5(b), the pressure gage spectra are shown. The suction and exhaust pressures have dominant frequency content at the second multiple of the running speed, because this is a two stroke, two cylinder compressor. Also, there is a noticeable difference in the magnitude of odd harmonics versus the even harmonics for the suction, exhaust, and housing pressures. The even harmonics clearly dominate the frequency spectrum from 0-500 Hz for all of these transducer outputs. After 500 Hz, the exhaust pressure begins to exhibit odd numbered dominant resonances, while the housing and suction pressures continue to exhibit higher magnitudes with the even harmonics. After around 2000 Hz, all of these pressures cease to show any even/odd harmonic trends. The trends seen in the pressure data is contrasted to the spring force data of Fig. 5.1(b), which is not so obviously dominated by either odd or even harmonics of the fundamental frequency. Also of note is that the housing pressure has its most dominant peak at the fourth multiple of the fundamental, showing that the housing pressure has a different dynamic behavior than the suction pressure, despite the fact that the two static pressures should be identical. The housing pressure dynamics could be influenced by the standing wave characteristics of the housing space.

The rms value of the housing pressure dominant harmonic gives us an idea of the sound pressure level within the compressor. This value, of approximately 0.045 psi (0.310 kPa), would represent a sound level of nearly 144 dB re 2.9×10^{-9} psi (20×10^{-6} Pa) in air at atmospheric pressure and room temperature. This value of interior compressor noise is an over-simplification however, because it does not take into account all of the harmonics present in the housing pressure spectrum. This value also assumes that the housing pressure is uniform throughout the compressor shell, Also, this sound pressure level estimate does not account for the fact that conditions within the shell do not fit the standard air model assumed with the standard reference pressure. It only serves to present an indication of the large magnitude of the sound level within the compressor shell.

5.1.3. OTHER TRANSDUCER DATA AND SUMMARY

Along with force and pressure data, other data were collected including compressor accelerations and a signal from a gear installed on the crankshaft as discussed in chapter 4. A complete set of this data can be seen in appendix 4. Table 5.1 summarizes the key features of the data including the peak-to-peak magnitude of the data as well as the dominant harmonics of each data set.

The dominant frequency of the shock-loop accelerometer data shown in Fig. 5.6(b) was found to be the second multiple of the operating speed. This indicates that at low frequencies, this data behaved more like the exhaust gases flowing through this tube than it did like an equivalent suspension spring. At higher frequencies (around 1000 Hz and above), the shock-loop acceleration begins to look less like the exhaust gas because it does not favor the odd harmonics of the fundamental frequency. In this range, the shock-loop accelerometer more closely resembles the suspension springs, which show more equity between the relative magnitudes of odd and even harmonics.

The compressor accelerations were unique, due to the fact that their dominant harmonics occurred at much higher harmonics than the force and pressure data. An example of this can be seen in a typical accelerometer signal shown in Fig. 5.7. This data was taken from the Y-axis component (see Fig 4.9) of the accelerometer mounted on the motor cap.

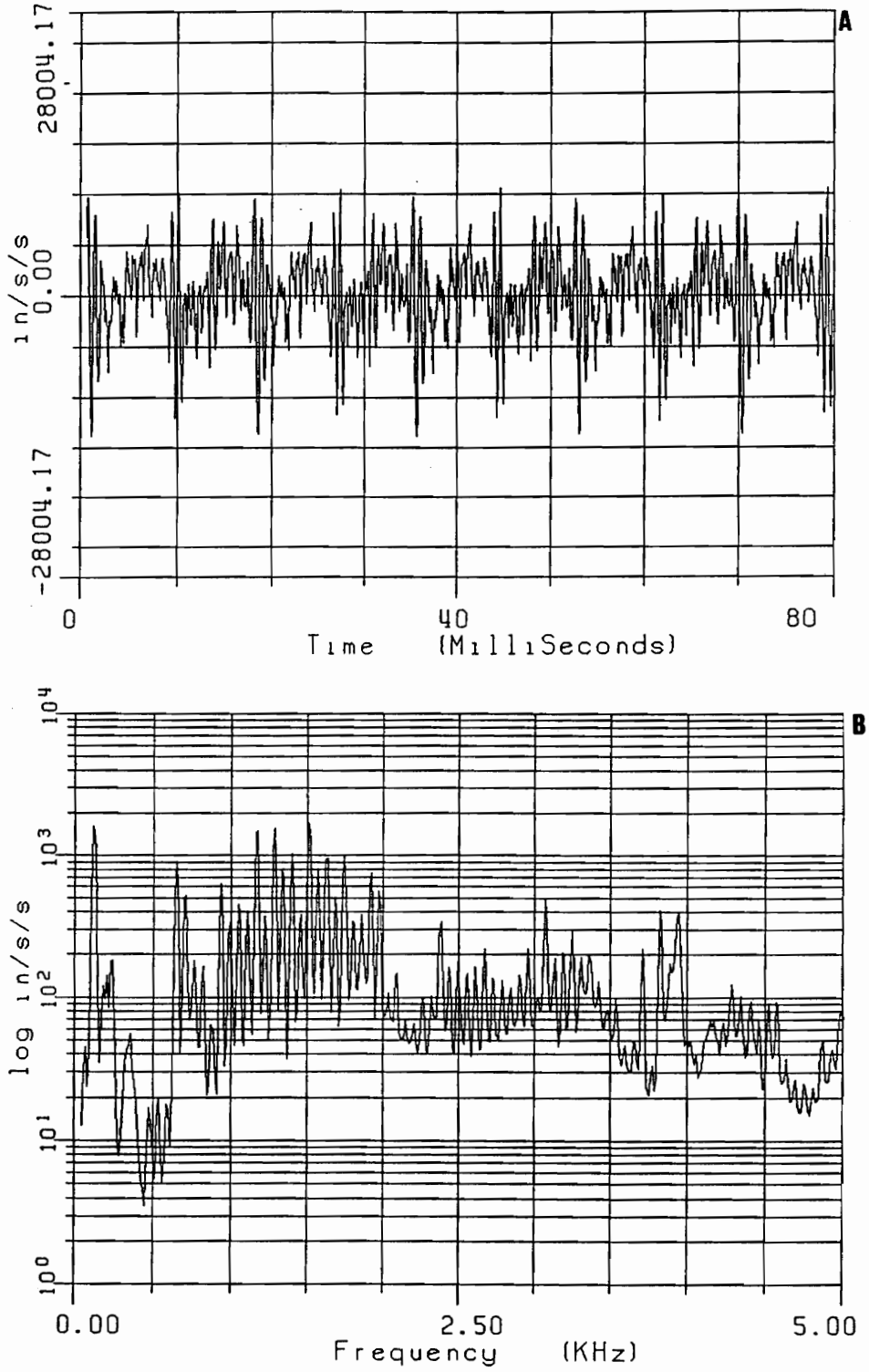

FIGURE 5.6. (a) Time- and (b) Frequency-Domain Shock-Loop Accelerometer Data (1 in/s/s = 25.4 mm/s/s)

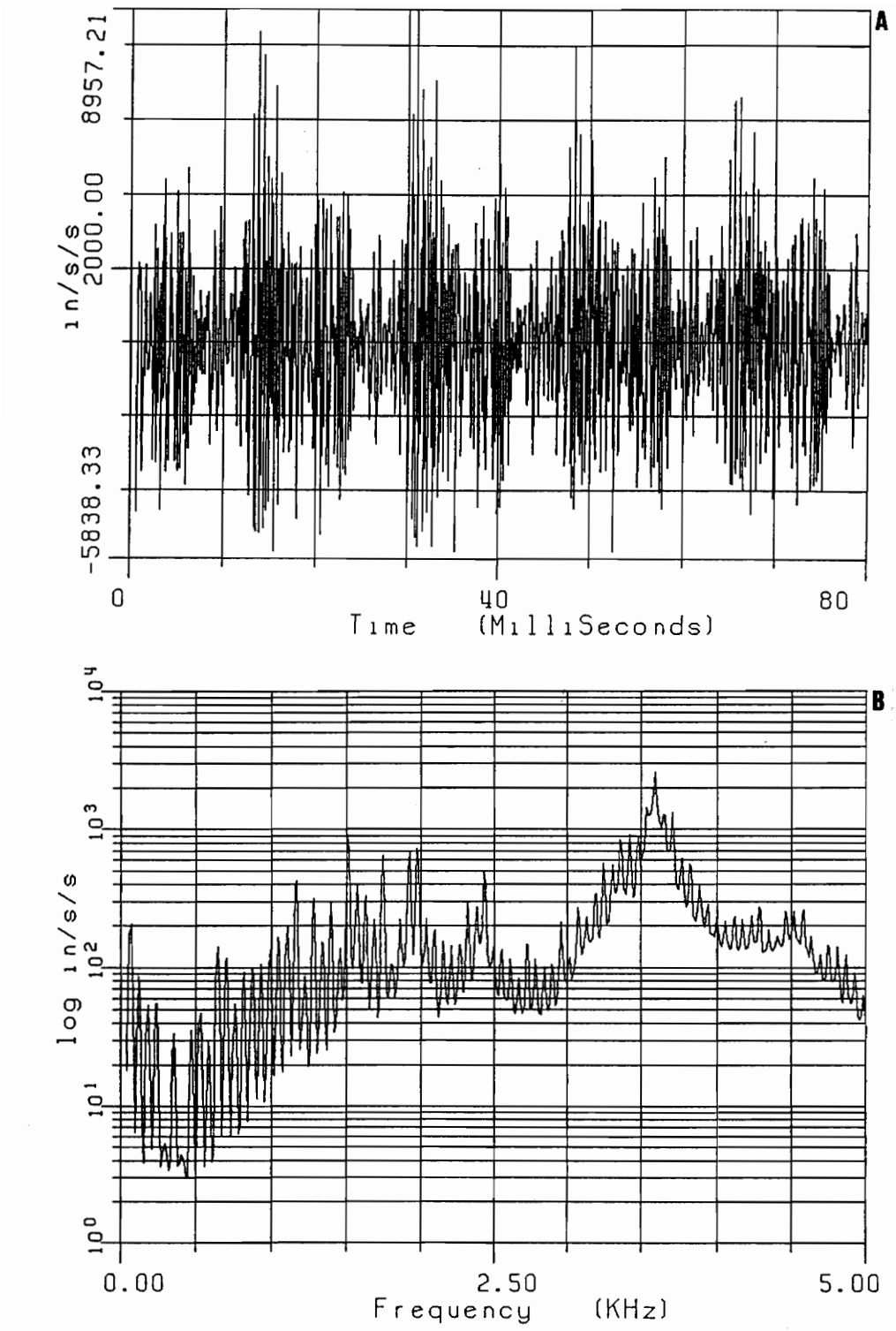

FIGURE 5.7. (a) Time- and (b) Frequency-Domain Compressor Acceleration Data (1 in/s/s = 25.4 mm/s/s)

TABLE 5.1. Dominant Characteristics of Transducer Outputs

Transducer Location	**Magnitude (peak-to-peak)**	**Dominant Multiples of Fundamental Frequency**
Right Spring X axis	4.4 lb (20 N)	1, 9, 10, 14, 35
Right Spring Y axis	3.0 lb (13 N)	2, 1, 11, 34
Right Spring Z axis	2.9 lb (13 N)	1, 2, 16, 18, 14, 9, 26
Left Spring X axis	3.8 lb (17 N)	1, 10, 2, 14, 20, 24, 26
Left Spring Y axis	3.0 lb (13 N)	1, 2, 11, 16, 20, 18, 4
Left Spring Z axis	3.6 lb (16 N)	1, 26, 14, 2, 20, 22, 24
Top Spring X axis	1.9 lb (8.5 N)	1, 15, 47
Top Spring Y axis	0.9 lb (4.0 N)	1, 10, 2, 4
Top Spring Z axis	2.0 lb (8.9 N)	1, 22, 10, 11, 26
Shock-Loop	2375 in/s/s (60.33 m/s/s)	2, 26, 22, 20
Housing Cavity	0.25 psi (1.7 kPa)	4, 2
Top Cylinder	321 psi (2213 kPa)	1, 2, 3, 5, 6
Bottom Cylinder	336 psi (2317 kPa)	1, 2, 3, 6, 5,
Exhaust Pressure	40 psi (276 kPa)	2, 11, 44, 9, 6, 13
Suction Pressure	12 psi (83 kPa)	2, 4, 6, 12, 16, 14
Crankcase X axis	6270 in/s/s (154 m/s/s)	26, 24, 46, 30
Crankcase Y axis	7200 in/s/s (183 m/s/s)	26, 24, 65, 30, 20
Crankcase Z axis	2530 in/s/s (64.3 m/s/s)	1, 2, 65, 20, 4
Motor Cap X axis	12,380 in/s/s (314 m/s/s)	52, 53, 26, 56, 34
Motor Cap Y axis	17,410 in/s/s (442 m/s/s)	62, 61, 64, 63, 26
Motor Cap Z axis	14,800 in/s/s (376 m/s/s)	62, 42, 40, 36, 26

5.2. RESULTS OF COMPRESSOR SOUND OUTPUT MEASUREMENT

In addition to transducers within the compressor, simultaneous sound measurements were made with an external microphone positioned in four locations as seen in Fig. 4.15 and Fig. 4.16. This sound data was taken with the same data acquisition parameters as the internal transducer data. The resulting sound spectrum from the far-field microphone test is shown in Fig. 5.8. The spectra from three other microphone tests are shown in appendix 5.

These figures show the un-weighted sound pressure level (SPL) in dB, referenced to 2.9×10^{-9} psi (20×10^{-6} Pa) . The dominant harmonics of the sound pressure level were dependent upon the microphone location, indicating that each face of the compressor had its own sound radiation characteristics. Table 5.2 lists the dominant harmonics of the SPL for each microphone location.

Many of the dominant harmonics of compressor sound output from these tests fell within or near the 1000 Hz-1600 Hz frequency range of the H25A sound spectrum identified by Bristol Compressors and discussed in section 1.2.2. The 1000 Hz one-third octave band corresponds roughly to the 18th harmonic (1040 Hz) which was the dominant harmonic in the far-field and long side microphone locations. This harmonic was also a major harmonic in the short side microphone location. The 1600 Hz one-third octave band (1400-1800 Hz) roughly corresponds to the 30th harmonic (1734 Hz) of the fundamental frequency, and appears in the far-field and long side microphone locations as a major harmonic.

Although most of the important harmonics of the sound measurement tests were found to fall within the 1000 Hz to 600 Hz range, other major frequency content was seen outside this range. Present as a major harmonic in these tests is the 33rd harmonic (1907 Hz) which was just outside this range. The 4th harmonic (231 Hz), which corresponds to the 250 Hz octave (224-280 Hz) was noticed as major only on the compressor short side. Here it was seen as the dominant harmonic for that sound spectrum.

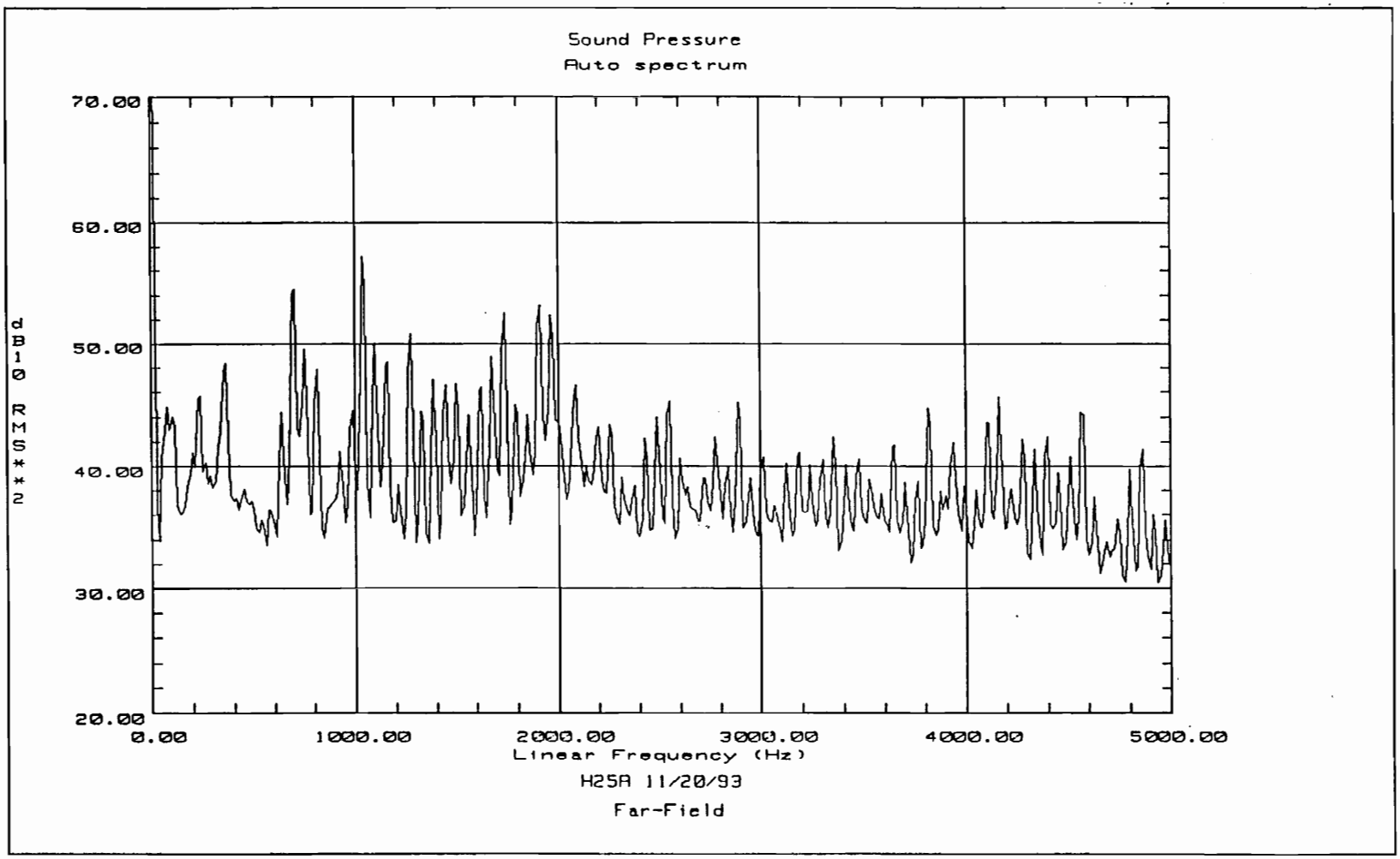

FIGURE 5.8. Far-Field Compressor Sound Output Spectrum

TABLE 5.2. Dominant Multiples of Sound Output Spectrum vs. Microphone Location

Microphone Location	Dominant Harmonics
Far-Field	18, 12, 33, 30, 34
Long Side	18, 33, 30, 24, 20, 12
Short Side	4, 26, 12, 18, 20, 11, 6
Top	38, 12, 20, 13

It is speculated here that the dominant 4th harmonic in the short side microphone location is linked to the pressure fluctuations within the compressor housing. As can be seen in table 5.1, the 4th harmonic is a major harmonic for the suction pressure and exhaust data. It is also the highest magnitude peak for the housing pressure data. Since the housing pressure and suction pressure directly contact the compressor housing, and because these pressure spectra show such a dominant fourth harmonic (more so than the exhaust pressure), it is speculated that this low-frequency sound is the result of the suction and housing pressure fluctuations.

It should also be mentioned that a general trend was noticed in the sound spectra which pertained to the pressure data. All of the microphone tests resulted in spectra which show dominant peaks spaced by approximately 116 Hz (twice the fundamental frequency) at low frequencies (below around 800 Hz) and at the even harmonics of the fundamental frequency. Above 800 Hz, the peaks are spaced at 57.8 Hz, without any trends with respect to even or odd harmonics. This dominance of the even harmonics at low frequencies leads to the conclusion that the low-frequency sound spectra look much more like the pressure spectra than they do like the spring data.. This once again gives evidence that the low-frequency compressor sound output is pressure related.

5.3. MULTIPLE COHERENCE RESULTS

Although comparing the spectra of inputs and outputs by inspection can sometimes yield important results, it can also lead to confusion in cases where the output doesn't resemble any of the inputs. For this reason, the multiple-input model has been developed to mathematically indicate which inputs contribute to the output and to what degree.

As discussed in section 2.3.3, the multiple coherence function $\gamma^2_{y:x}$ can be used to quantify the validity of a multiple-input model. In cases where insufficient inputs are considered to describe an output, the multiple coherence function can be expected to approach a value of zero. In cases where adequate inputs are considered to describe an output, the value of multiple coherence can be expected to tend towards one. Other factors, such as non-linearity and low signal-to-noise ratios can also contribute to low values of multiple coherence.

The results shown in this section show multiple coherence functions between various model inputs and the sound pressure level measured at the compressor long side. These multiple coherences are typical of the multiple coherence functions from the other microphone locations, except for the far-field test coherence which was slightly lower, most likely due to lower signal-to-noise ratios at this microphone location.

Figure 5.9(a) shows the multiple coherence with all of the force gages, all of the pressure transducers, and the shock-loop accelerometer considered as inputs to the sound pressure level output. Note that this multiple coherence is high for some harmonics of the fundamental frequency, is zero at many frequencies, has low multiple coherence at the frequencies between harmonics, and looks abnormal from 0-2800 Hz. The low coherence between harmonics is most likely due to low output in the broad-band resulting in low signal-to-noise ratios, and was expected. The areas of zero coherence and the range from 0-2800 Hz, however, indicated an unacceptable model. A similar result from the H23A study indicated that the shock-loop accelerometer was the principal cause of this abnormality[4]. Considering a model with only the spring forces and compressor pressures as inputs resulted in the multiple coherence of Fig. 5.9(b). In this figure, the multiple coherence is above 0.8 at most frequencies above 1500 Hz, but many lower frequencies exhibit poorer coherence, with several areas dropping to zero coherence. This is once again an unacceptable model, as evidenced by the multiple coherence function.

The disruption of information in the multiple coherence plots of Fig. 5.9 is most likely due to high levels of ordinary coherence between model inputs. As discussed in section 3.2.5, the ordinary coherence between any two inputs to a multiple input model should never be unity. As can be seen from the ordinary coherence plot of Fig. 5.10(a), the top and bottom cylinder pressures had unity values of ordinary coherence for many harmonics between 0 and 1000 Hz. Similarly, the shock-loop accelerometer was totally coherent with the exhaust pressure at a few harmonics as seen in Fig. 5.10(b). This evidently is related to the poor and unusual multiple coherence function seen in Fig. 5.9. Although it cannot be explained why exactly these inputs caused the unusual behavior in the multiple coherence at so many frequencies, they were not considered as model inputs

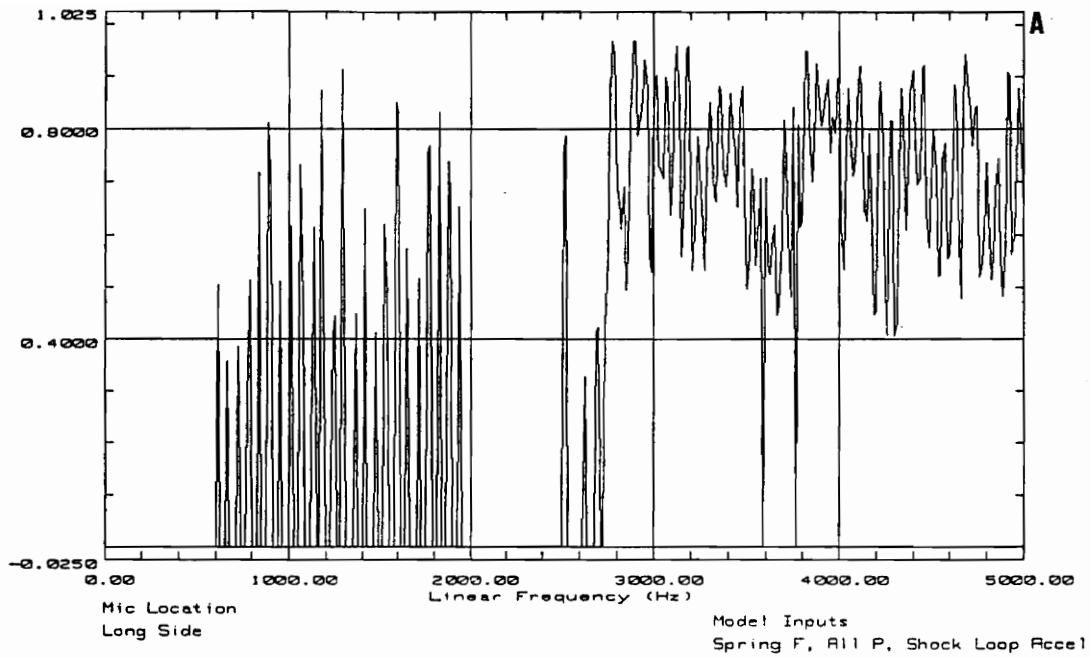

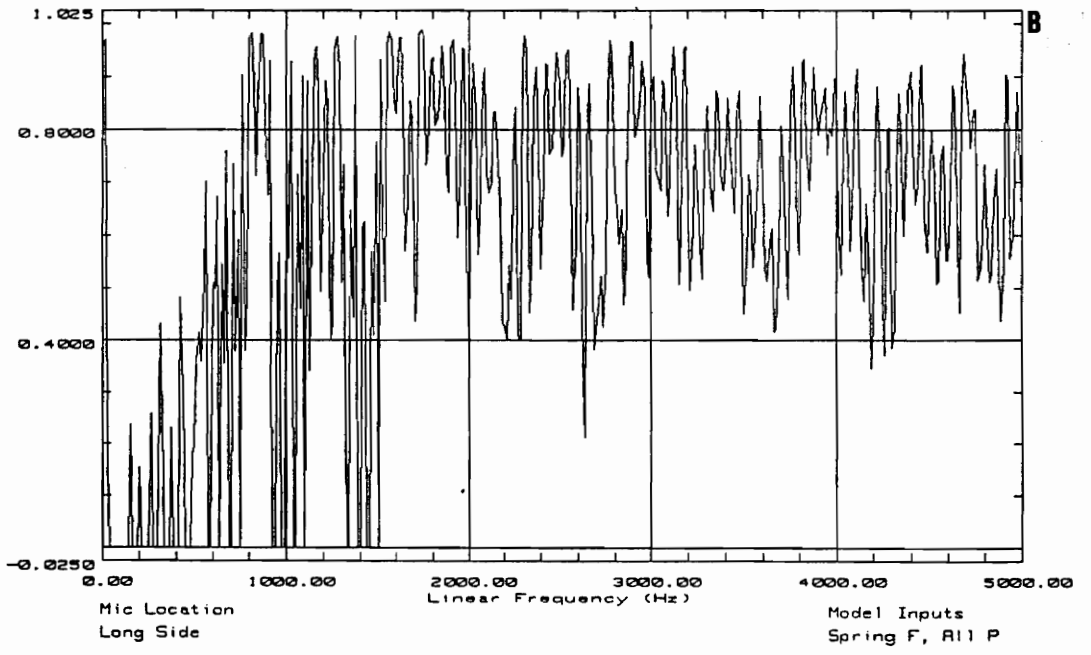

FIGURE 5.9. Multiple Coherence Functions Including (a) Shock-loop Acceleration and (b) Cylinder Pressures as Inputs

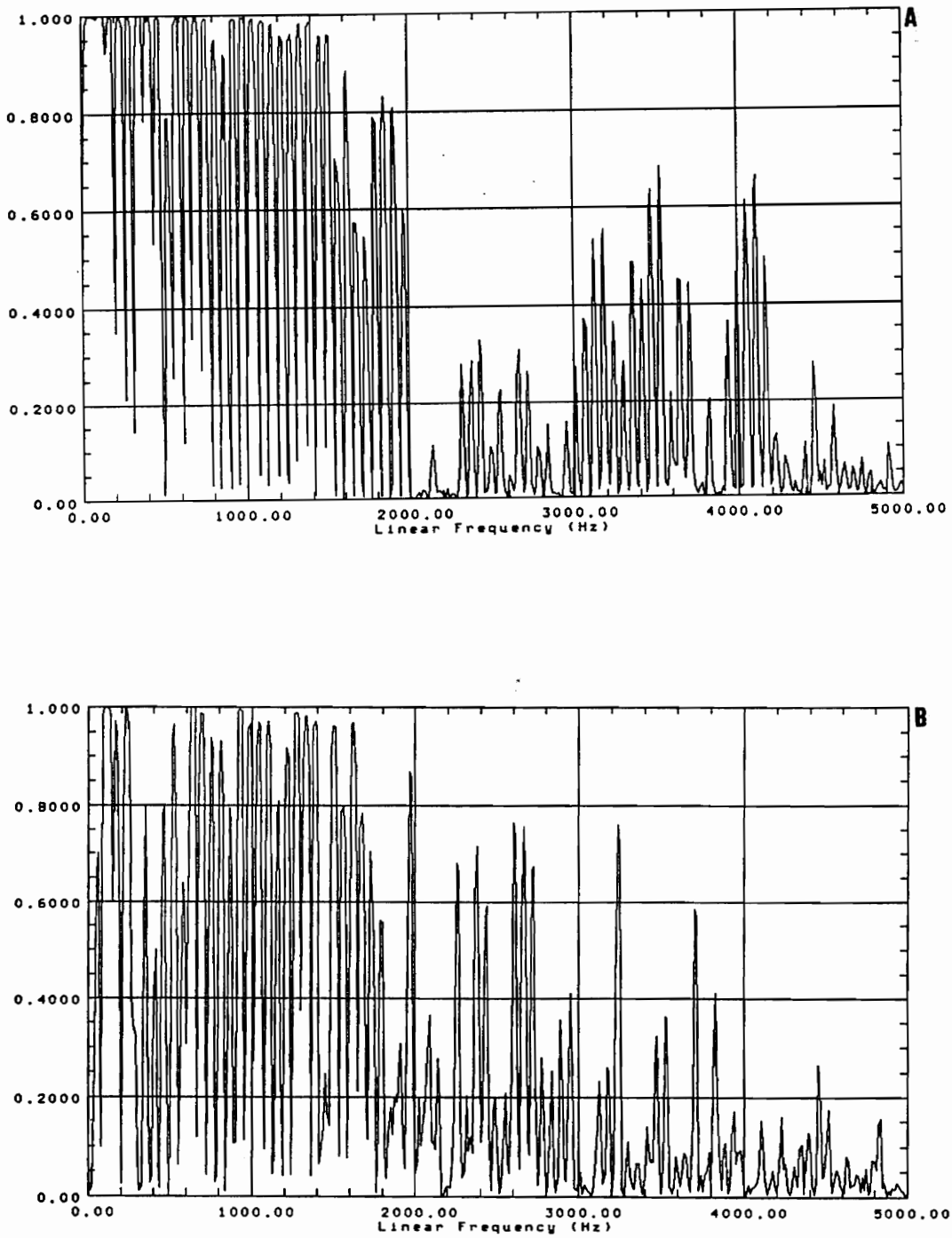

FIGURE 5.10. Ordinary Coherence Between (a) Cylinder Pressures and (b) Exhaust Pressure and Shock-loop Accelerometer

based upon the guidelines explained in section 3.2.5. and upon the fact that acceptable multiple coherence functions were obtained with these particular inputs removed. It should also be noted that the ordinary coherence between inputs in general was very high (0.9 or greater) below 1600 Hz and rather low beyond this frequency. Several examples of ordinary coherence between model inputs are shown in appendix 6.

Figure 5.11 shows the multiple coherence with a third model in which neither the cylinder pressures nor the shock-loop accelerometer were not considered as inputs. This multiple coherence is above 0.8 at all harmonics between 700 Hz and 2200 Hz, and at many frequencies beyond 2200 Hz. With the exception of the low frequencies, this model appears to show an adequate representation of the output by the force gages, the housing pressure, and the suction and exhaust pressures. Figure 5.12 shows the measured sound output, G_{yy}, compared to the sound output contributed by these inputs, G'_{yy}. The difference between these inputs is G_{nn}, as described in section 2.3.2. G_{nn} for this model appears as a nearly broad band spectrum of approximately 35 dB magnitude for the long side microphone location.

Pearson and Thaller [26], utilized multiple coherence to rank the importance of inputs to the total output of a system, as discussed in section 3.3. By comparing the multiple coherence functions of different inputs with the same output, judgment could be made as to the importance of the inputs to the output. Figure 5.13(b) shows the multiple coherence function between the far-field sound pressure spectrum and the pressure transducer measurements. Figure 5.13(a) shows the multiple coherence between the far-field sound pressure level and the force gage measurements. Note that although there is some difference in the multiple coherence values between the harmonics of the fundamental frequency, both plots show a multiple coherence above .8 for the harmonics between 700-2000 Hz. Employing the reasoning of [26], this would mean that Fig. 5.13(a) shows that the pressures are not significant contributors to the far-field sound pressure level from 700-2000 Hz. That is because there is sufficient multiple coherence between the force inputs and the output to indicate that the forces alone can account for the sound pressure level output. However, the same can be said of the pressure inputs when viewing Fig. 5.13(b). Therefore, the logic of this method of viewing multiple coherence data is not valid in this case because it yields contradictory results. This may be due to the fact that coherence between the force and pressure data was high, but no

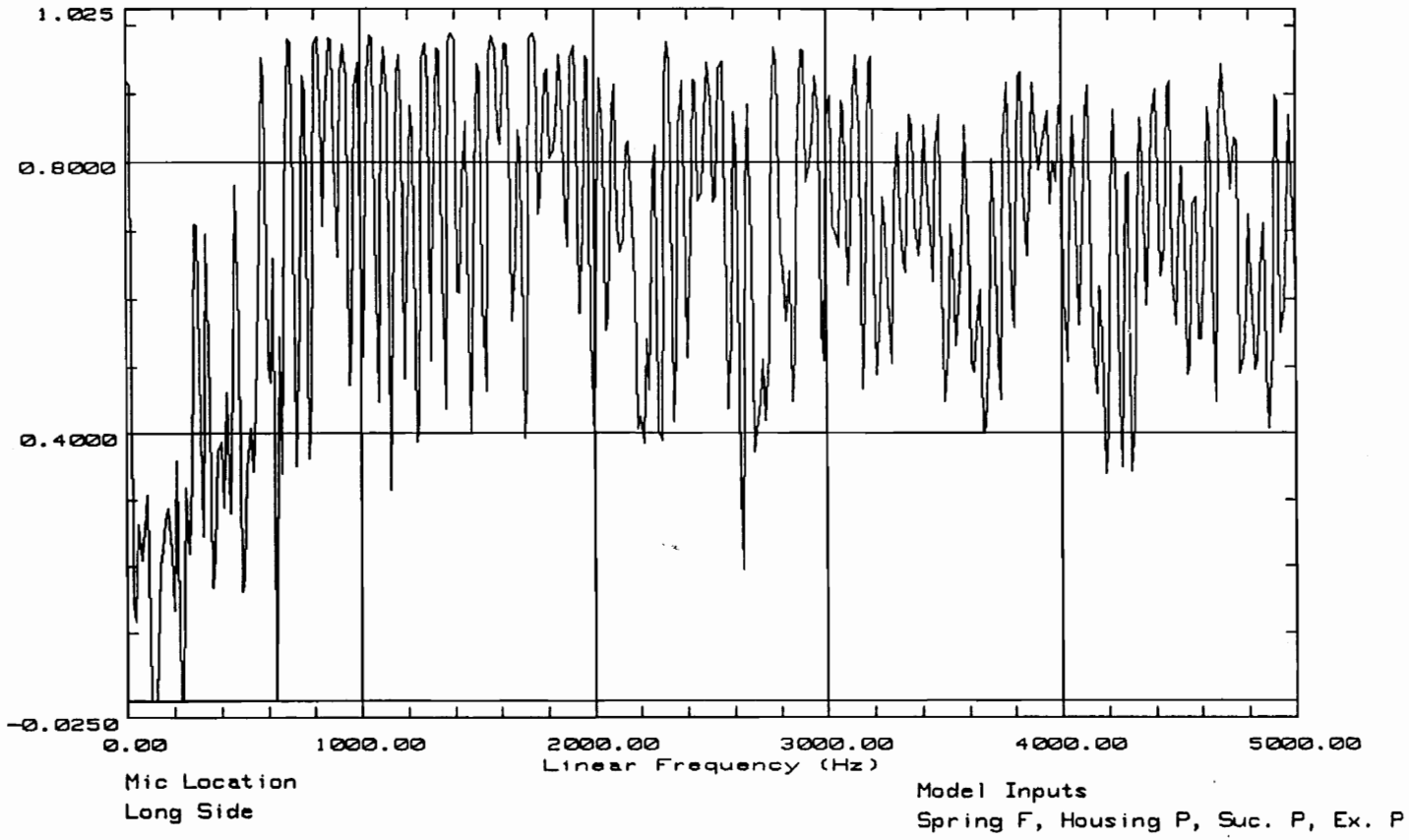

FIGURE 5.11. Multiple Coherence Function of Final Model

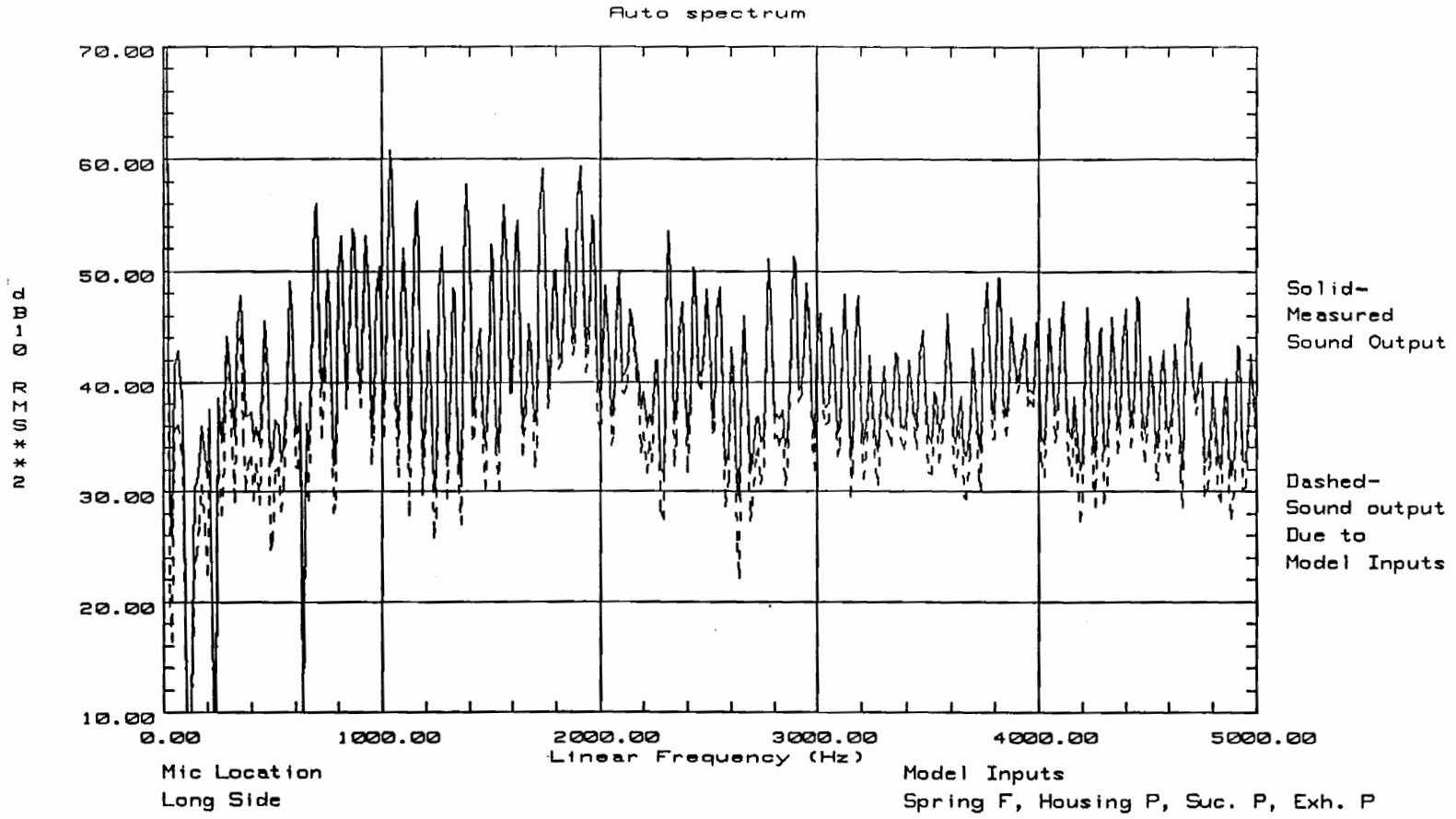

FIGURE 5.12. Measured Versus Model Output for Final Model

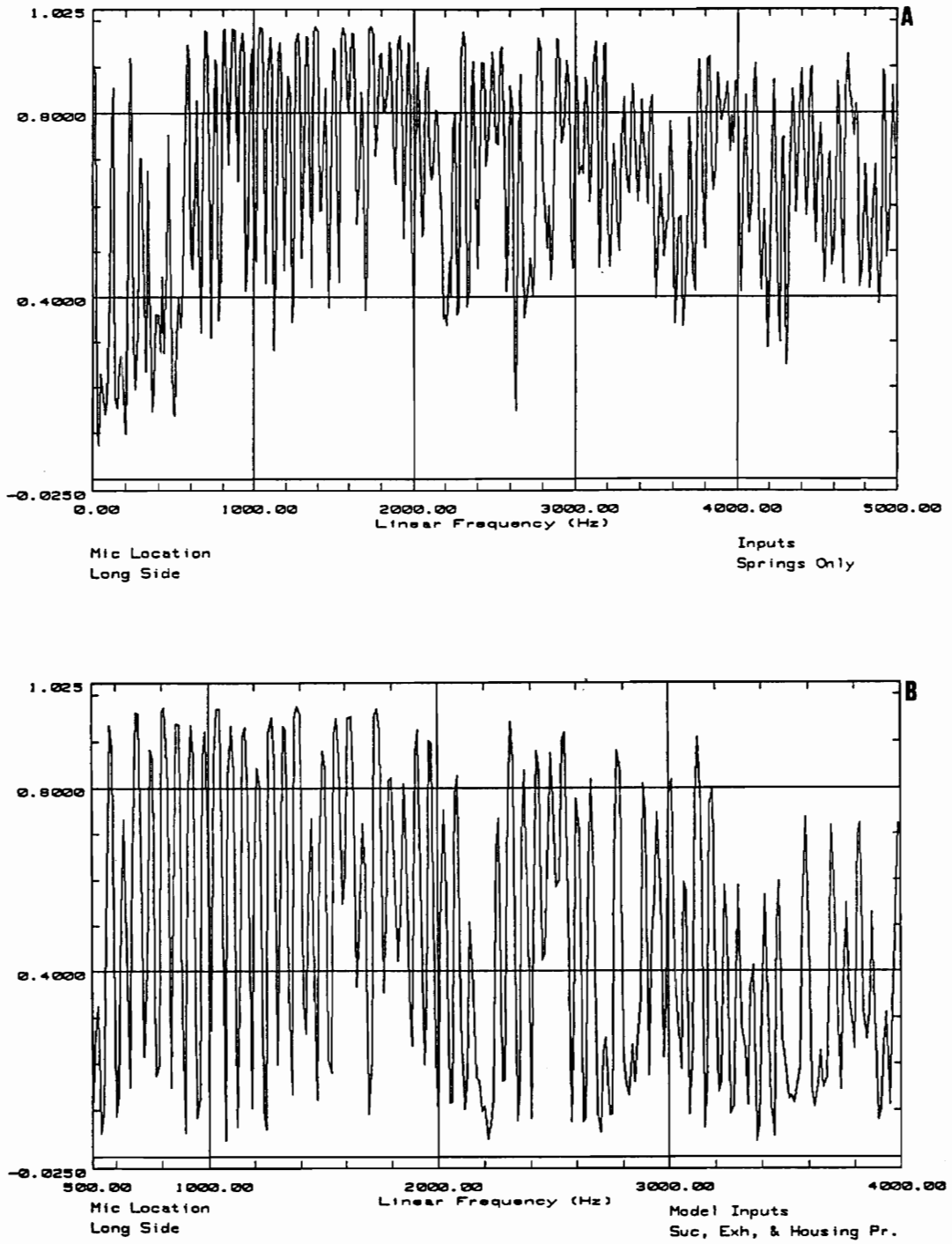

FIGURE 5.13. Multiple Coherence of (a) Spring Forces and (b) Suction, Exhaust, and Housing Pressures

attempt has been made to mathematically show this. Instead, multiple coherence comparisons of the type described here were simply avoided in this study due to the inconsistency found.

5.4. RESULTS OF MULTIPLE-REFERENCE FRF ANALYSIS

The results of Figs. 5.11 and 5.12 are encouraging because they indicate that a multiple-input/single-output analysis with inputs consisting of the suspension spring forces and compressor pressures and an output of the external sound pressure level could be performed. This could provide useful information about whether the mechanical structure-borne vibration path or the acoustic pressure path transmits more of the compressor sound to the external environment. The low multiple coherence below 700 Hz, as well as the abnormal coherence at 700 Hz, prevented a thorough analysis of low-frequency data. The most important frequency range for this study (1000 Hz to 4000 Hz), however, met the expectations of the experimenters for a satisfactory model.

Figures 5.14-5.17 are the results of a multiple-reference FRF analysis as described in sections 2.3 and 3.1.1. Considering the nine force inputs as x_1, x_2, ..., x_9 and the suction, exhaust, and housing pressures as inputs x_{10}, x_{11}, and x_{12}, Figs. 5.14 compares the sound pressure level output of the model,

$$G'_{yy} = \sum_{i=1}^{12}\sum_{j=1}^{12} H_i^* G_{ij} H_j = \gamma^2_{y:x} G_{yy} \tag{5.1}$$

to the sound pressure level directly contributed by the pressure signals

$$G_{yy:x_{10},x_{11},x_{12}} = \sum_{i=10}^{12}\sum_{j=10}^{12} H_i^* G_{ij} H_j \tag{5.2}$$

Where H_i, H_j, and G_{ij} were computed from a spectral matrix as described in section 2.3. from data taken in the far-field microphone test. Figure 5.15 shows the same information over a smaller frequency range so detail can be seen around the 1000 Hz-2000 Hz region.

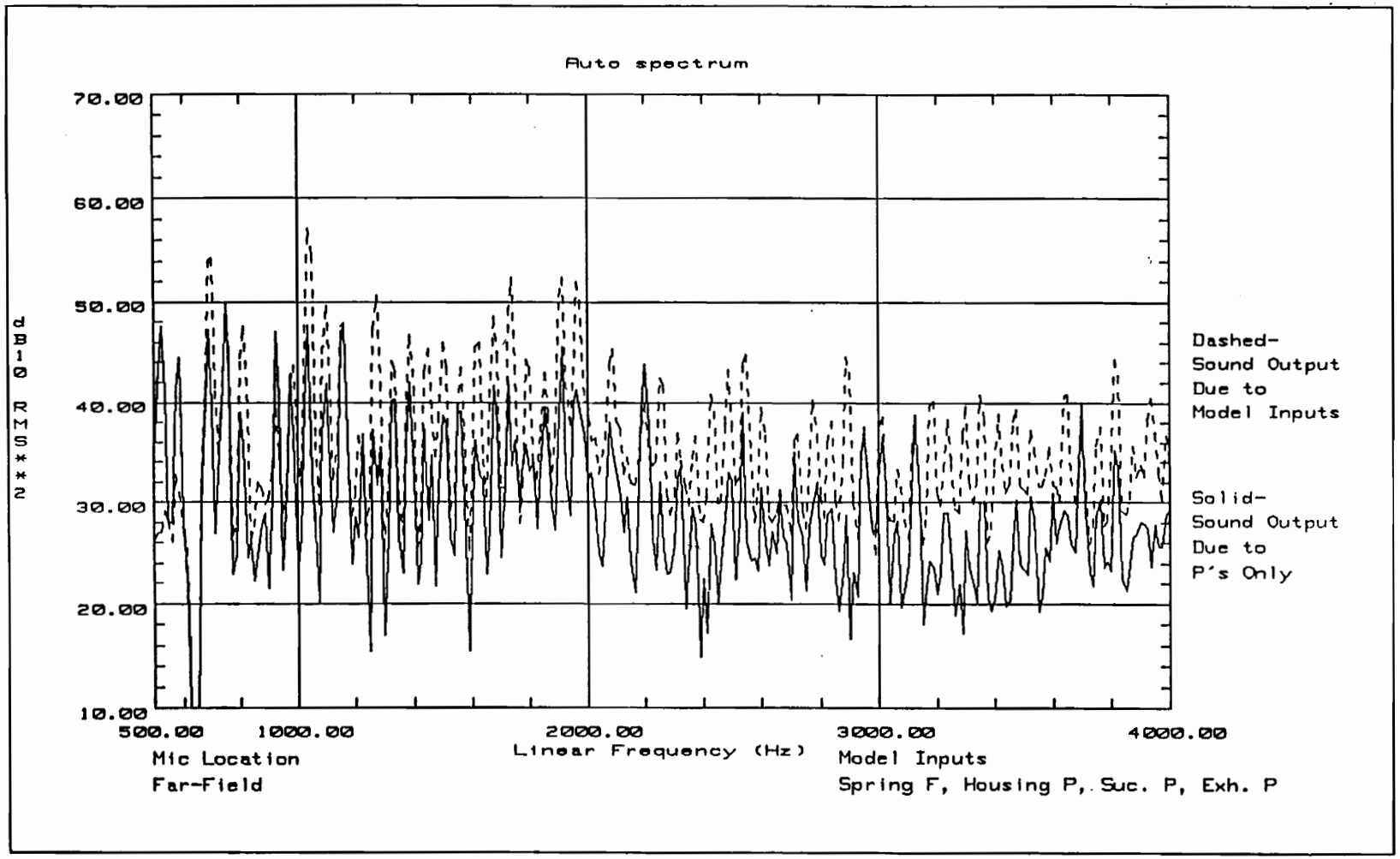

FIGURE 5.14 Prediction of Far-Field Sound Output Due to Pressure Fluctuations (Spring Forces Removed)

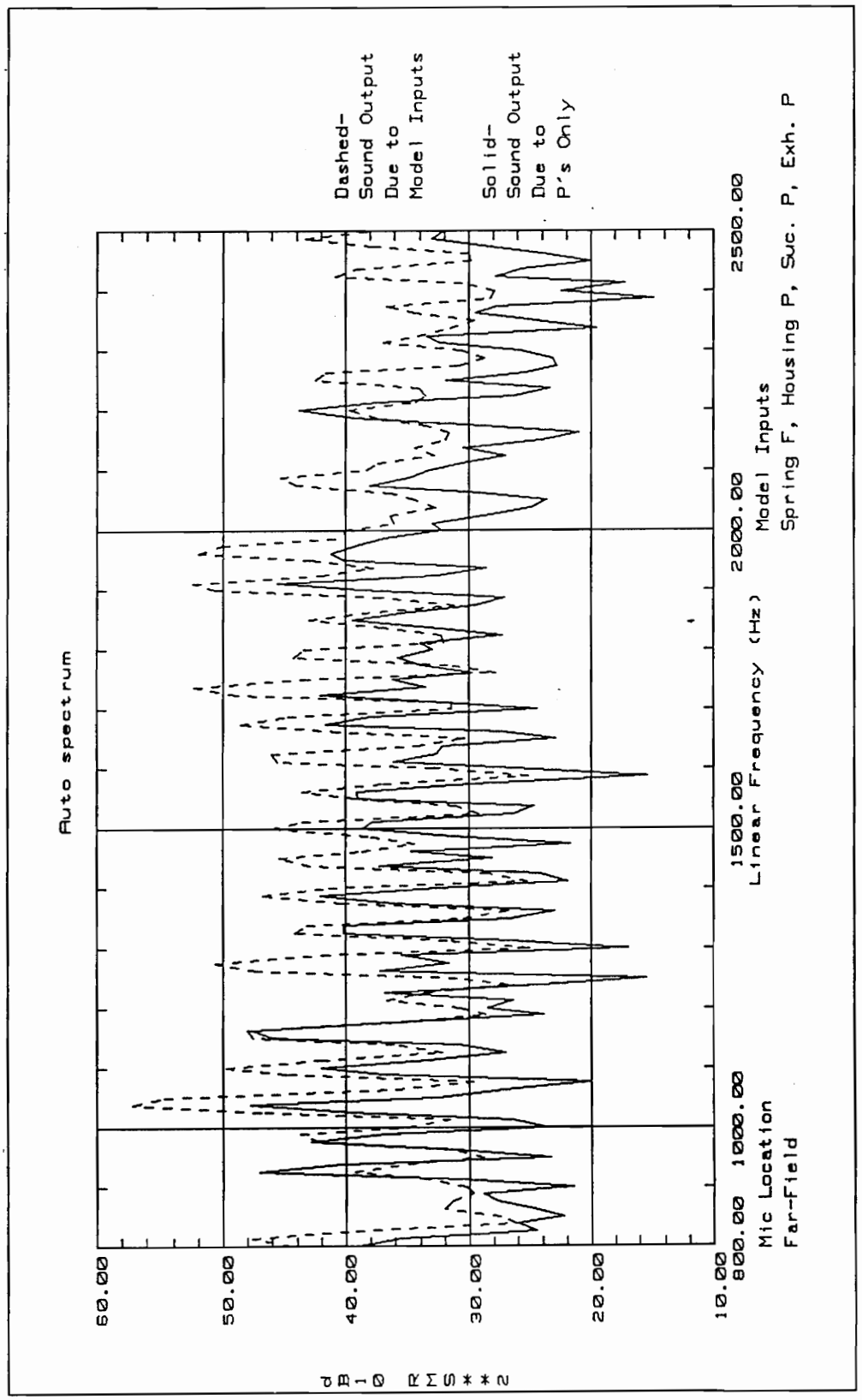

FIGURE 5.15 Middle Frequency Prediction of Far-Field Sound Output Due to Pressure Fluctuations

Figures 5.16 and 5.17 compare the model sound output contributed by the spring force signals

$$G_{yy:x_1,x_2,\ldots,x_9} = \sum_{i=1}^{9}\sum_{j=1}^{9} H_i^* G_{ij} H_j \tag{5.3}$$

to the sound pressure level output of the model, G'_{yy}.

Examination of Fig. 5.14 indicates an average magnitude drop of each harmonic by about 6.5 dB with the suspension spring inputs removed. The harmonics in Fig. 5.16 for the most part remain unchanged with the pressure inputs removed. The indication of these plots is that overall, the far-field sound level consists of more correlated content from the spring transmission path than from the acoustic pressure inputs. The tests from the other microphone locations, presented in appendix 7, yield the same conclusion.

As expected, the MIMO model provided information which was not obvious by inspection of the transducer spectral data. The results of the MISO analysis indicate that the pressures are not important to the frequency range from around 800 Hz and above. The MISO results also indicate the corollary, that the spring forces are important to the higher frequency sound spectra, both in the far-field and at all the compressor faces.

Since the multiple coherence of the model investigated was low in areas below 700 Hz, it was not desirable to make conclusions based upon this data. As can be seen in Fig. 5.11, however, some frequencies corresponding to harmonics of the fundamental frequency exhibit multiple coherence values of 0.6 and above, which can be considered marginally acceptable. Figure 5.18 shows the same model as shown in Fig. 5.14, only with the X-axis of the plot shifted to include the low frequencies. It can be seen in this plot that the area around the 4th harmonic is over-represented by the compressor pressures. Around 800 Hz, the pressure spectra fall below the sound output. Although this supplements the earlier conclusion that the pressure fluctuations are responsible for low-frequency compressor sound output, it must be remembered that the low multiple coherence values in this range make Fig. 5.18 suspect to some degree.

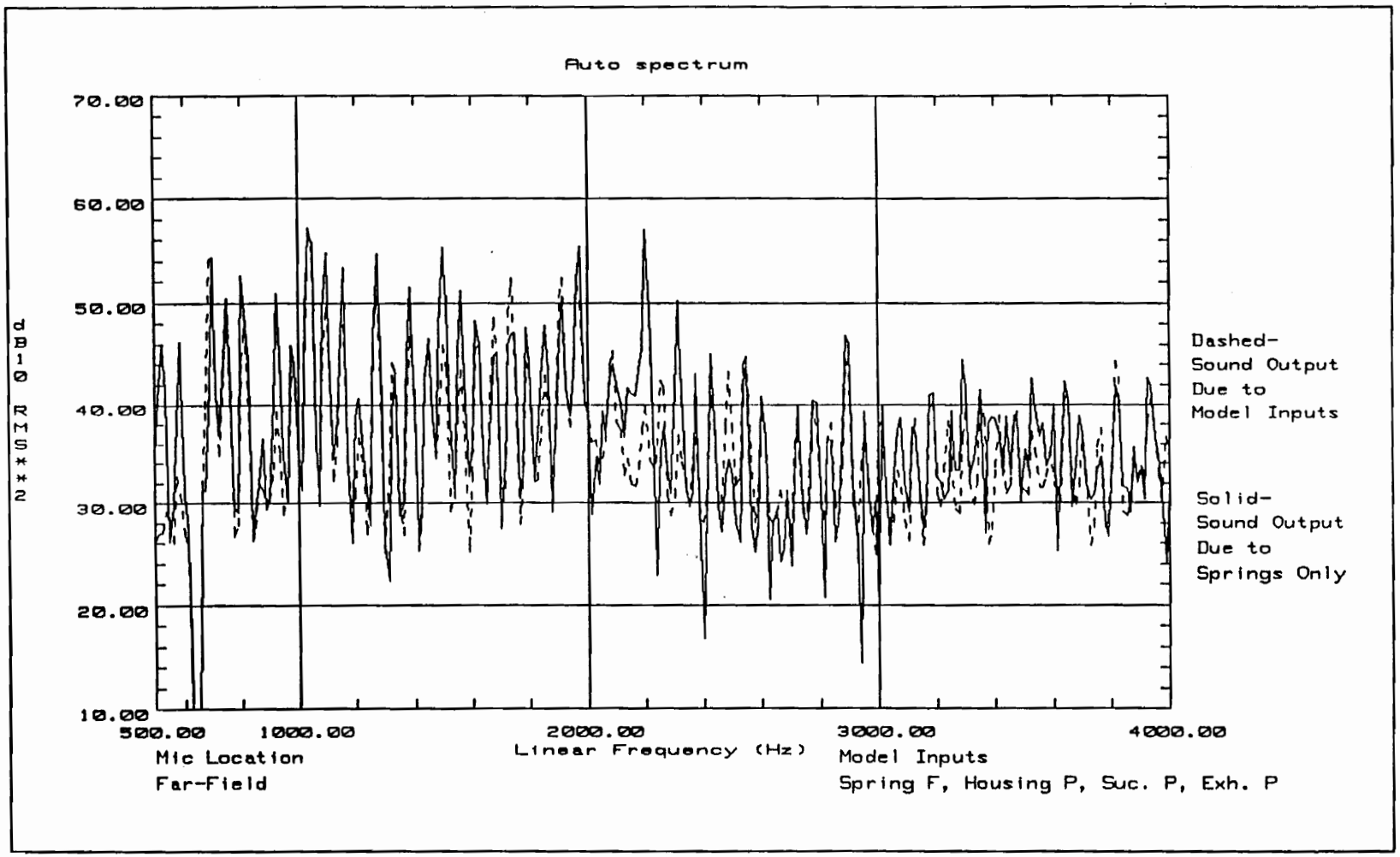

FIGURE 5.16 Prediction of Far-Field Sound Output Due to Spring Forces
(Pressure Fluctuations Removed)

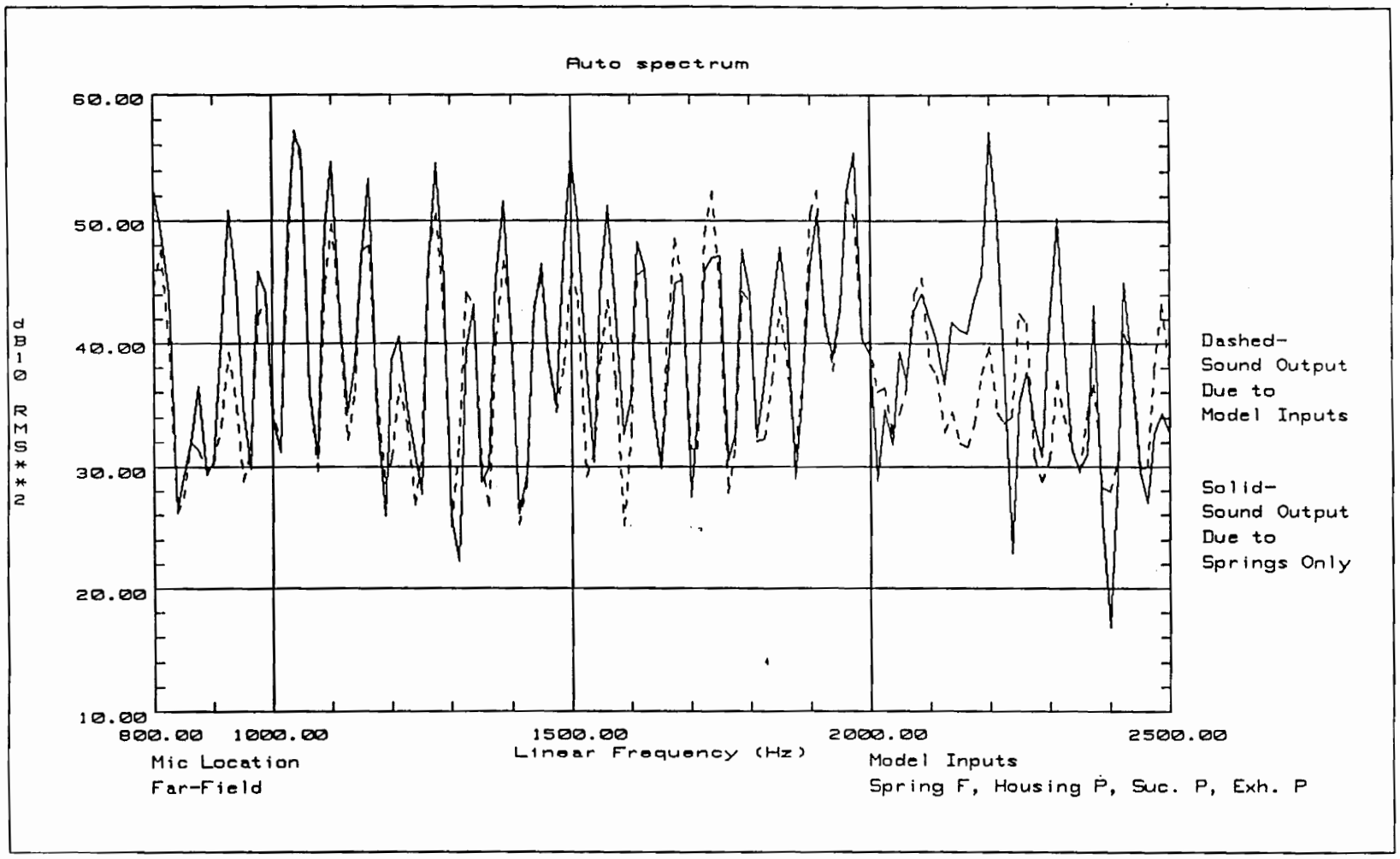

FIGURE 5.17 Middle Frequency Prediction of Far-Field Sound Output Due to Spring Forces

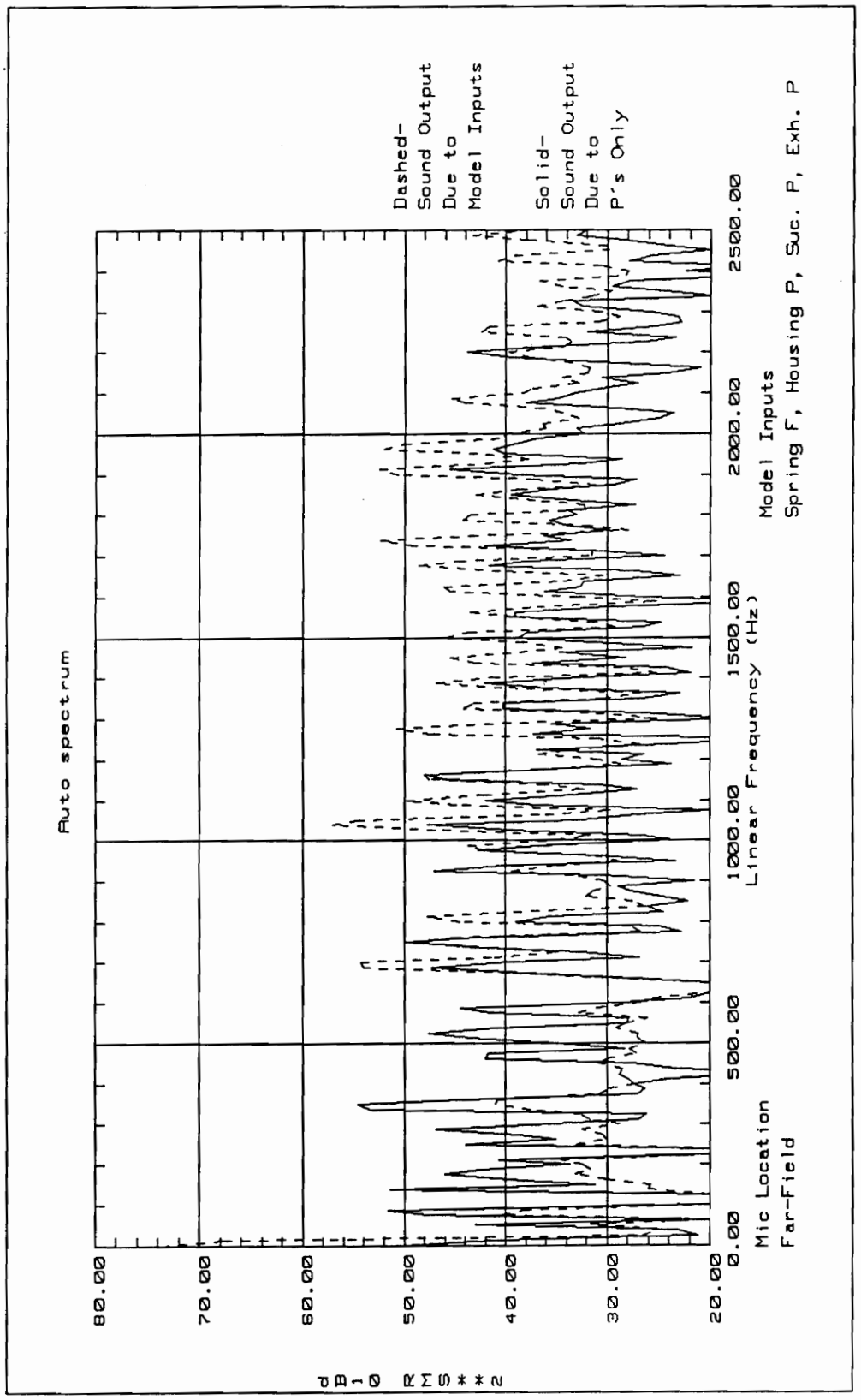

FIGURE 5.18 Low Frequency Prediction of Sound Output Due to Pressure Fluctuations

Note that in all of the MISO analysis plots some harmonic peaks drop, others remain the same, and some even rise after the deletion of some inputs. This fact can be attributed to the phasing of each harmonic as compared with the output and the other inputs. The phase information of each input is carried through the cross spectrum and FRF terms in Eqns. (5.1),(5.2), and (5.3). As the terms of these equations sum, the output auto spectrum magnitude rises and falls as harmonics add constructively and destructively. The result is that a combination of a few inputs may exceed the total output at some frequencies because some destructive terms have not yet been added.

Although the tests with differing microphone locations generally agreed with each other, there were many differences in the specific harmonics which dropped and by what amount. Appendix 7 shows the results of modeling the sound output due to the pressure inputs only for the three other microphone locations. One major difference is the harmonic peaks which were unchanged or actually raised in magnitude. Table 5.3 illustrates the difference in harmonics which did not decrease with the removal of the suspension springs, as well as the overall average dB drop over the frequency range shown (peaks which did not drop were counted as a zero drop for averaging).

Appendix 8 shows the results of attempts to compare the relative contribution of the top spring to the right side spring. The contribution of the top spring alone to the far-field sound output spectrum is 4.1 dB below the total model output on average. The contribution of the right side spring is 3.2 dB below the model sound pressure output. This indicates that the side springs contribute more to the far-field sound level than the top spring, although the difference is not as dramatic as the comparison between the springs and the pressures. The difference between the top and side springs can also be noted form table 5.2, which shows that the compressor top emits a sound spectrum which is unique from the sound radiated from the other compressor sides, as well as the far-field. None of the dominant peaks in the top sound spectrum corresponded to the important harmonics of the far-field. The long side, on the other hand, shares many common dominant peaks with the far-field.

TABLE 5.3. Comparison of Microphone Location to Effect of Spring Removal on Compressor Sound Output

Microphone Location	**Average dB Drop of Sound Output Harmonics with Springs Removed**	**Multiples of Fundamental not Significantly Diminished with Springs Removed**
Far-Field	6.5	9, 10, 13, 16, 17, 20, 51, 52, 54, 64
Long Side	8.2	9, 10, 17, 20, 38, 52, 62
Short Side	9.5	9, 10, 16, 35, 48
Top	8.7	9, 10, 14, 16, 22, 23, 25, 30, 66

This finding, that the long side sound radiation and side support springs are more important to the far-field sound radiation than the compressor top, is seemingly in disagreement with the finding by Young that the top suspension spring and the compressor top are more important to the overall compressor sound output[4]. Actually, the compressor studied by Young, the Bristol H23A, had a different shaped top than the H25A. After noting the finding of Young, Bristol redesigned the flat H23A top into a more domed top, as seen in the H25A (Figs. 1.1, 1.2). The finding here seems to indicate that the domed top does in fact radiate less sound to the far-field, and the compressor long sides have now moved into the prominent place as the major sound radiators.

5.5. RESULTS OF CONDITIONED SPECTRAL ANALYSIS

An attempt was made to support the results of section 5.4 with the conditioned spectral method described in section 2.4 and section 3.1.2. By removing the linear effects of some inputs, it was hoped that evidence could be found to support the findings showing a strong contribution of the mechanical path to external sound output. Unfortunately, the nature of conditioned spectral analysis is somewhat different than multiple reference FRF analysis. In the case of this experiment, it could only be used to address different questions.

As mentioned in section 2.4, causality among inputs must be established prior to attempting a successful conditioned spectral analysis. Once established, the input with the highest priority must be conditioned out of the output first, followed by the next highest priority input. The last input conditioned out must not contribute to or cause any of the inputs already conditioned out of the output. In the case of this analysis, priority was unable to be determined among all of the inputs. Do the spring forces cause the housing pressure or vice versa? Questions like this could not be fully answered. Since the system was driven by a non-random excitation, the priority ranking system proposed by Park and Kim[15] could not be used. The only definite conclusion made regarding priority was that all of the pressure fluctuations and spring forces were caused by the process of gas compression in the cylinders. This process moves the gas through the system, thus creating the suction, exhaust, and housing pressures. Also, the piston slap, friction, valve

impacts, and piston head forces cause the structure-borne vibrations which result in suspension spring forces.

Figure 5.19 shows the sound output before and after the removal, or conditioning out, of the top and bottom cylinder pressures. Considering the top cylinder pressure to be input x_1, and the bottom cylinder pressure to be x_2, the output with the removal of the cylinder pressures is equivalent to

$$G_{yy.12} = G_{yy.1}(1-\gamma^2_{2y.1}) \tag{5.4}$$

Note that the sound pressure level drops significantly with both cylinder pressures conditioned out of the sound pressure output, as expected. Also note, however, that some specific harmonics do not drop as drastically as others. The region up to 2000 Hz results in every peak dropping at least 6 dB with some dropping as much as 17 dB. Between 2000 Hz and 3000 Hz, however, there are some peaks which only drop 4 dB or less. This plot then indicates that although much of the compressor sound output is a direct result of the cylinder pressure (which includes valve effects), there are other independent factors which contribute a small amount to some of the higher frequencies.

An attempt was made to condition out spring forces and other pressure signals, but the results were not easily interpreted. In both cases, the sound pressure level output dropped significantly. This is to be expected because the conditioned spectral model assumes that first inputs conditioned out of the output are the cause of the other inputs. Without a true knowledge of input priority, presenting and discussing results of this type is not a correct usage of this theory.

One approach which can circumvent this restriction is to run a conditioned spectral model with every possible combination of inputs, calculating partial coherence as described in section 2.4.2. The result would be a set of partial coherence between each input and output, with the effect of all the other inputs removed. Although this is not technically correct way to develop a total model, the coherence may yield information about the importance of each input to the output. Appendix 9 show some of the results of

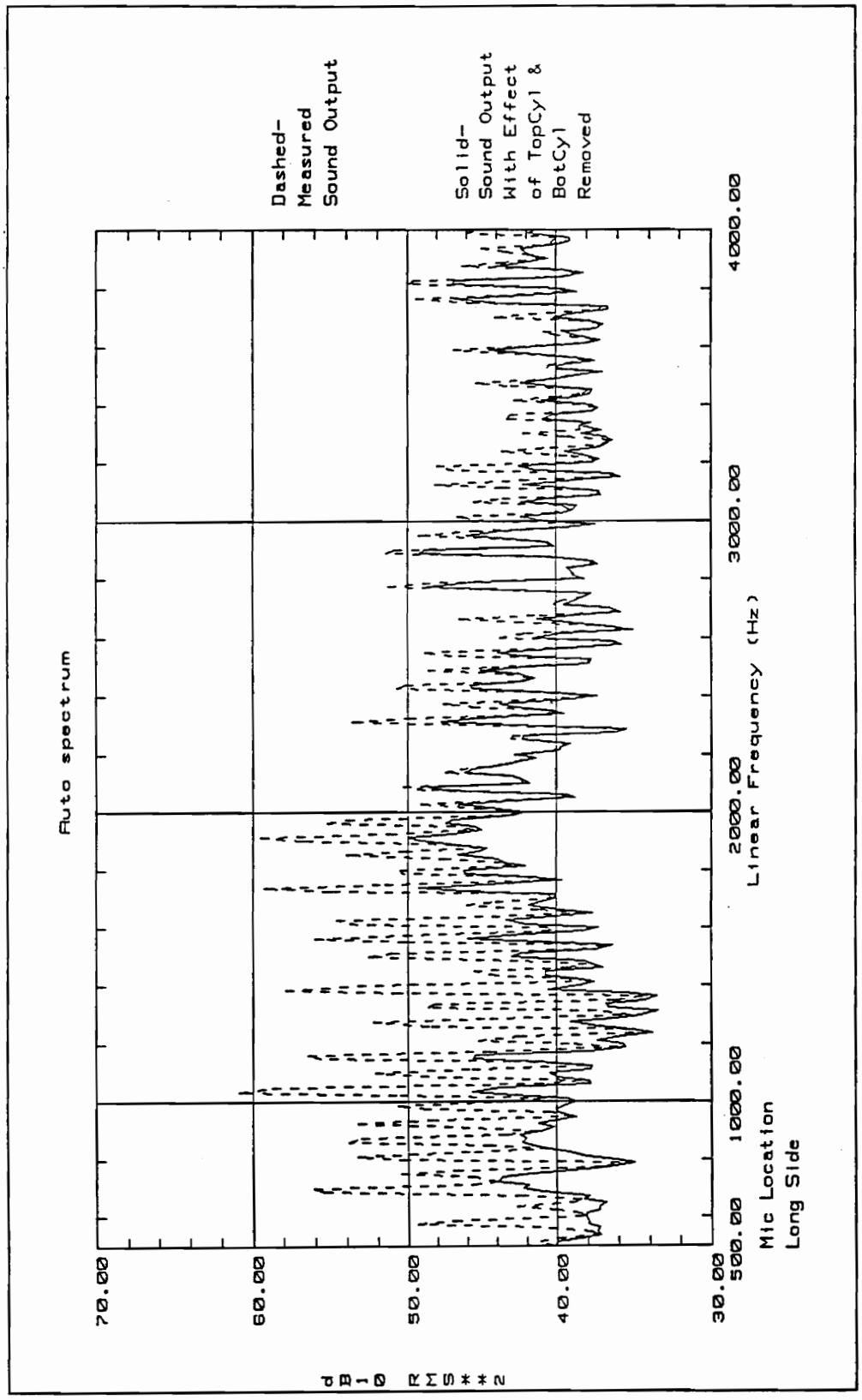

FIGURE 5.19 Sound Output Spectrum with Cylinder Pressures Conditioned Out

this approach. As can be seen, the partial coherences were low and did not contain many major frequency peaks. Because of this, no conclusions could be made as to the relative importance of each input based upon this type of analysis.

CHAPTER 6.
CONCLUSIONS AND RECOMMENDATIONS

The work presented in this thesis has yielded insight into the propagation of sound within the Bristol H25A compressor. Through the use of multiple-input/single-output (MISO) modeling, as well as through inspection of experimental data, conclusions have been reached pertaining to the relative importance of these propagation paths. This chapter summarizes these conclusions, and makes recommendations for the application and extension of the findings.

6.1. CONCLUSIONS

The most significant conclusion drawn from the results pertains to Figs. 5.14 and 5.15. In these figures, the compressor sound output directly contributable to the suspension springs is compared to the sound output contributable to the pressure fluctuations within the compressor. These predictions are the result of the MISO model generated from experimental test data, and predict the absolute "best case" sound reduction possible when certain inputs are removed from the system. The dramatic contrast between these two plots can only lead to the conclusion that the suspension spring transmission path is the dominant path for sound for most of the frequencies above 800 Hz. Comparison of the contributions of the side suspension springs to the top spring indicates that the side suspension springs provide more far-field radiated sound than the top stabilizer spring.

Inspection of the sound output spectra from the various microphone locations shown in Figs. 4.15 and 4.16 also support the conclusion that the compressor long sides (where the side suspension springs are mounted) radiate more sound to the far field than the compressor top. This is seen in table 5.2, where the compressor top and compressor short side dominant harmonics are quite different than the compressor long side and far-field dominant harmonics.

Frequencies below 800 Hz could not be conclusively identified by the MISO model due to low multiple coherence in this frequency range. Similarities between the low-frequency sound spectra and the low-frequency suction and housing pressure spectra, however, seem to indicate a relationship between the housing pressure and the low-frequency sound output. This may be related to low-frequency standing waves in the compressor housing, as investigated by Young[4].

Based upon tests performed on the instrumented compressor, it is concluded that the instrumented H25A compressor was dynamically different than a production H25A compressor. This is evidenced by the fact that the compressor ran from 1 to 4 dBA quieter than production compressors in two tests, without a significant effect on capacity or efficiency. Also, FRF's of the instrumented compressor's shell were quite different from a production compressor's shell. The changes in shell dynamics are attributed to the effect of the modified suspension springs shown in Figs. 4.2-4.5, mainly because the shell FRF's were obtained on un-pressurized compressors that were not running. Thus, the dynamic change was most likely due to structural changes in the instrumented compressor, not the disruption of the dynamic pressures within the operating compressor. This re-enforces the belief that the suspension springs can affect shell dynamics, and thus compressor sound output.

6.2. RECOMMENDATIONS

Based upon the above conclusions, it is recommended that efforts to reduce high frequency (above 800 Hz) sound output from the H25A compressor be focused upon altering the suspension system. The analysis techniques used here cannot provide recommendations as to how the suspension should be modified. However, the reduced sound output of the instrumented compressor indicates that Figs 4.2-4.5 may contain useful information regarding beneficial modifications to the compressor suspension system.

The most obvious change to the suspension system was the addition of a lumped mass in the suspension springs. Other, more subtle, changes occurred which could be investigated by finite-element modeling or experimental analysis. Effects on the

suspension system damping and stiffness should be determined and possible recreated. Another possible modification which affected the suspension system is the quartz crystal present within the piezoelectric force gages. All forces passing through the spring mounts were first transmitted through the piezoelectric quartz crystal. Perhaps this material was less efficient at transmitting the forces passing through the suspension springs.

The low-frequency harmonic content associated with the compressor pressure fluctuations and sound output is interesting because experimental determination of the compressor shell vibration modes showed no modes at frequencies below around 600 Hz[2]. This leads to the speculation that the low-frequency sound output may be transmitted by standing waves within the housing cavity. Such standing waves were identified in the H23A by Young[4]. Since the wavelength of these low frequency waves are larger than the compressor, the compressor behaves like a monopole sound radiator at these frequencies. Such radiation would not exhibit a detectable vibration mode shape.

Although the results determined here are based upon proven theoretical modeling techniques, it is suggested that some experimental verification of the results be attempted. Such an experiment might be the replaying of recorded housing cavity sound in an empty shell charged with refrigerant. Since a setup such as this would be void of any suspension, the outside sound levels should be low. This experiment should be inexpensive and worth the investment of time and resources.

One area of MISO analysis worth investigating is the effect of highly coherent inputs on the results of the MISO model. As discussed by Bendat[5], and covered in section 3.2.5 of this thesis, totally coherent inputs to a MISO model are not acceptable and can have an effect on the models validity as shown in section 5.3. Appendix 6 shows that the inputs used in this MISO study were very coherent (.9 and above) at many frequencies, although not totally coherent. One question not yet answered is whether highly, but not totally, coherent inputs can cause MISO results to be suspect in any way.

The final recommendation is that the statistical variation of compressor dynamics be considered. Although the dimensions and operating characteristics of a compressor line are often tightly controlled, the dynamic behavior of a compressor model can vary from unit to unit. This has been demonstrated in appendix 3. Any experiment which results in

an appreciable sound reduction should be repeated at least once on another compressor to ensure repeatability.

In many ways, the conclusions found support findings made on the H23A by Young[4], most notably the finding that the suspension springs are important to compressor sound output. As other compressor studies are conducted, constancy of results should always be kept in mind. For this reason, this study should only be considered as another sample in a body of knowledge about sound propagation which will hopefully keep growing in years to come.

REFERENCES

1. Price, S.M., *Identification of High Frequency Noise Paths and Noise Source Mechanisms in Reciprocating Hermetic Compressors*, Master's Thesis, Purdue University, Department of Mechanical Engineering, West Lafayette, IN, 1985.

2. Rose, J.A., *The Experimental Characterization of the Dynamics of a Reciprocating Freon Compressor System*, Master's Thesis, Virginia Polytechnic Institute and State University, Department of Mechanical Engineering, Blacksburg, VA, 1994.

3. Agee, B., Burnett, R., Cardany, K., Gardner, B., Kelly, A., Smith, J., Vipperman, J., Wallace, K., Hurst, C.J., Knight, C.E., and Mitchell, L.D., *Investigation of the Potential for Noise Reduction of a Reciprocating Compressor*, Project Report, Virginia Polytechnic Institute and State University, Department of Mechanical Engineering, Blacksburg, VA, 1990.

4. Young, D., Master's Thesis in Progress, Virginia Polytechnic Institute and State University, Department of Mechanical Engineering, Blacksburg, VA, Contact: Professor L.D. Mitchell.

5. Bendat, J.S. and Piersol, A.G., *Random Data*, Wiley-Interscience, New York, 1986.

6. Bendat, J.S. and Piersol, A.G., *Engineering Application of Correlation and Spectral Analysis*, Wiley-Interscience, New York, 1980.

7. Bendat, J.S., "Solutions for the Multiple Input/output Problem", *Journal of Sound and Vibration*, Vol. 44, No. 3, Feb. 1976, pp. 311-326.

8. Bendat, J.S., "System Identification from Multiple Input/output Data", *Journal of Sound and Vibration*, Vol. 49, No. 3, Dec. 1976, pp. 293-308.

9. Bendat, J.S., "Modern Analysis Procedures for Multiple Input/output Problems", *Journal of the Acoustical Society of America*, Vol. 68, No. 2, Aug. 1980, pp. 498-503.

10. Dodds, C.J. and Robson, J.D., "Partial Coherence in Multivariate Random Processes", *Journal of Sound and Vibration*, Vol. 42, No. 2, Sept. 1975, pp. 243-250.

11. Trethewey, M.W., *Establishment of Multiple Input Modeling Techniques for Transient Noise Source Identification: With Application to Structural Sources of Forge Hammer Noise*, Ph.D. Dissertation, Michigan Technological University, Department of Mechanical Engineering, Michigan, 1981.

12. Trethewey, M.W. and Evensen, H.A., "Evaluation of the Structural Noise Sources of a Four-Piece Gravity Drop Forge Hammer by Residual Spectrum Techniques", Internoise 80 Proceedings, Miami, FL, Dec. 1980, pp. 487-490.

13. Trethewey, M.W. and Evensen, H.A., "Identification of Noise Sources of Forge Hammers During Production: An Application of Residual Spectrum Techniques to Transients", *Journal of Sound and Vibration*, Vol. 77, No. 3, 1981, pp. 357-374.

14. Trethewey, M.W., Evensen, H.A., and Shapton, W.R., "Combination of Multiple Input Models and Experimental Modal Analysis for Identification of Structural Noise Generating Mechanisms: With Application to Forge Hammers", *Noise Control Engineering Journal*, Vol. 21, No.3, Nov.-Dec. 1983, pp. 89-102.

15. Park, J.S. and Kim, K.J., "Determination of Priority Among Correlated Inputs in Source Identification Problems", *Mechanical Systems and Signal Processing*, Vol. 6, No. 6, 1992, pp. 491-502.

16. Ufford, D.A. and Bernhard, R.J., " A Signal Processing Technique to Identify the Number of Incoherent Sources in a System", Inter-Noise 90 Proceedings, Newport Beach, CA, Dec. 1989, pp. 1123-1128.

17. Leuridan, J., Roesems, D., and Otte, D., "Use of Principal Components Analysis for Correlation Analysis Between Vibration and Acoustical Signals", ISATA 87, Florence, Italy, 1987, pp. 488-504.

18. Romburg, T.M., "An Algorithm for the Multivariate Spectral Analysis of Linear Systems", *Journal of Sound and Vibration*, Vol. 59, No. 3, 8 Aug. 1978, pp.395-404.

19. Tweed, L.W. and Branch, R.D., "Fundamental Aspects of Multiple Input/output Analysis", ASME paper 85-DET-152, 1985.

20. Seybert, A.F. and Crocker, M.J., "Recent Application of Coherence Techniques in Diagnostics and Pediction of Noise", Inter-Noise 76 Proceedings, 1976

21. Seybert, A.F. and Crocker, M.J., "The Use of Coherence Techniques to Predict the Effects of Engine Operating Parameters on Diesel Engine Noise". ASME Paper 75-DET-33, 1975.

22. Alfredson, R.J., "The Partial Coherence Technique for Source Identification on a Diesel Engine", *Journal of Sound and Vibration*, Vol. 55, No. 4, 22 Dec. 1977, pp. 487-494.

23. Koss L.L. and Alfredson, R.J., "Identification of the Transient Sound Sources on a Punch Press", *Journal of Sound and Vibration*, Vol. 34, No. 1, 1974, pp. 11-33.

24. Hayes, P.A., Seybert, A.F. and Hamilton, J.F., "A Coherence Model for Piston-Impact Generated Noise", SAE Paper No. 790274, 1979.

25. Chung, J.Y., Crocker, M.J., and Hamilton, J.F., "Measurement of Frequency Responses and the Multiple Coherence function of the Noise-generation system of a Diesel Engine", *Journal of the Acoustical Society of America*, Vol. 58, No.3, Sept.1975, pp. 635-642.

26. Thaller, R.E. and Pearson, J., "Coherence Methods Used to Define Transmission Paths in Airborne Antenna Vibration", Shock and Vibration Bulletin, Vol. 46, 1976.

APPENDIX 1.
RESULTS OF IN-SITU CALIBRATION OF TRIAXIAL FORCE GAGES

The calibration curves presented in Figs. A1.1-A1.3 are the results of an in-situ calibration of the Kistler 9251 triaxial force gages used in the Bristol H25A study. This calibration was required because the standard transducer preload specified by Kistler could not be used in this study without placing the gages in danger of failing. These calibration curves were obtained experimentally as described in section 4.1.2.

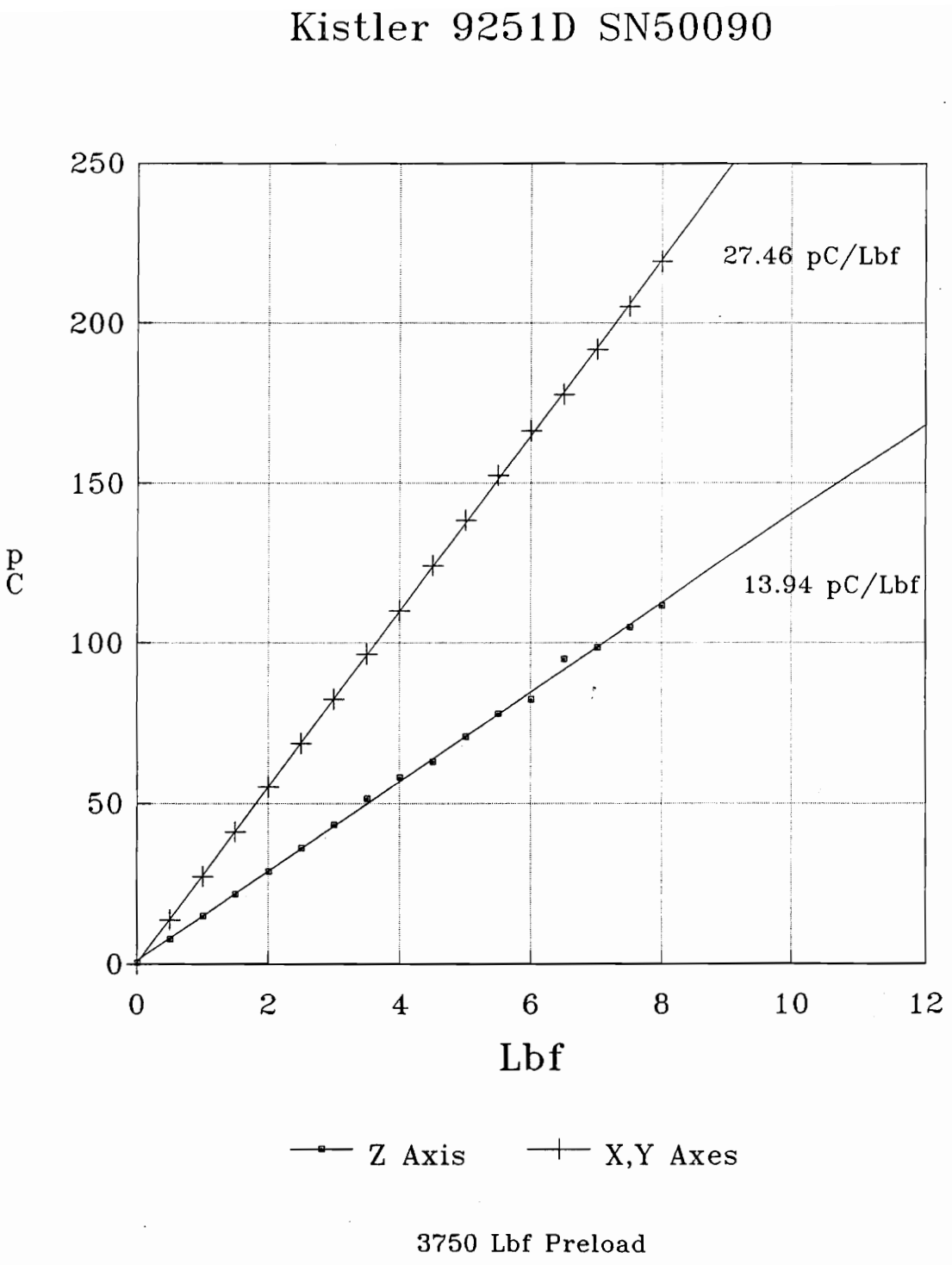

FIGURE A1.1. Static Calibration of Top Triaxial Force Transducer
(1 lbf = 4.448 N)

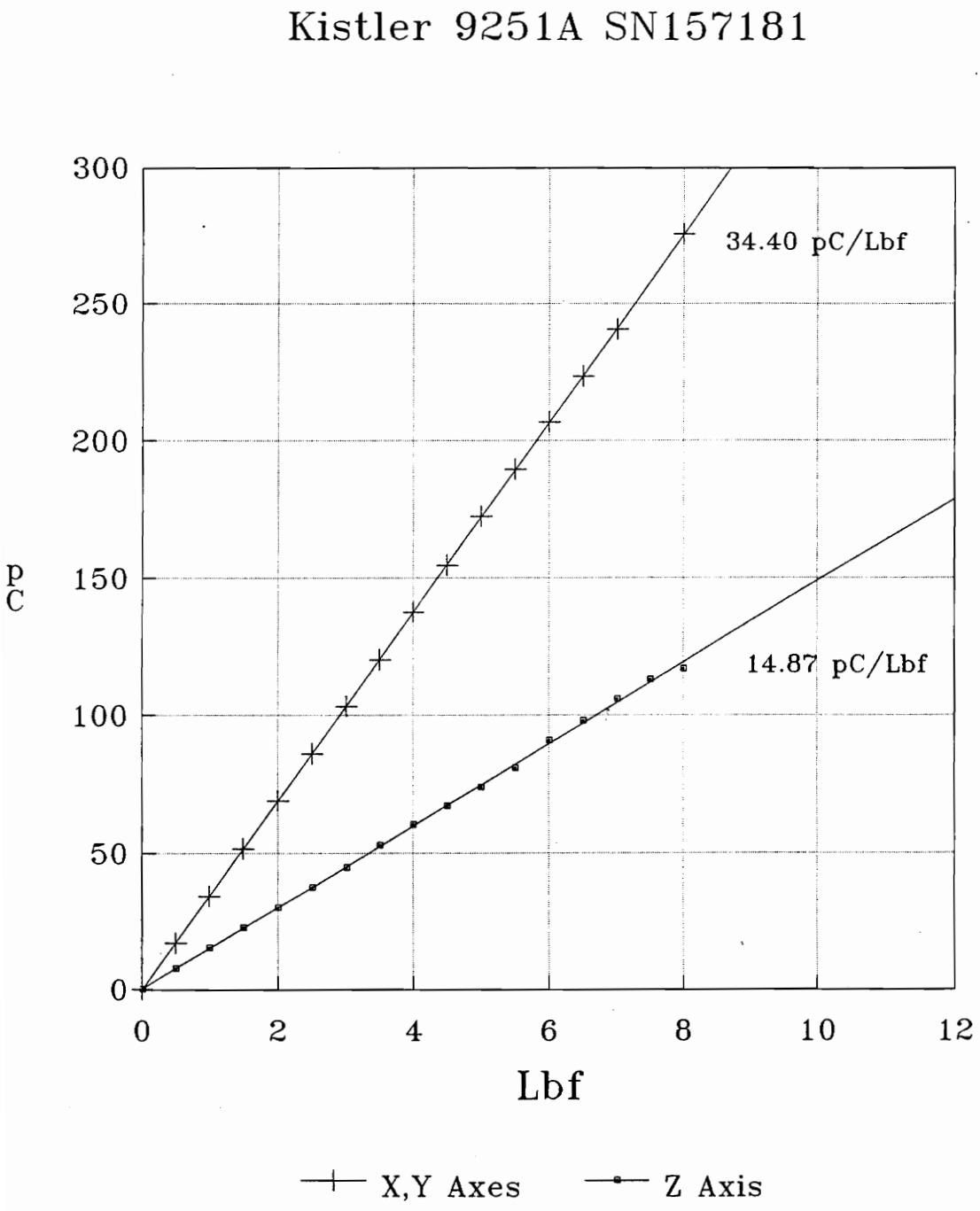

FIGURE A1.2. Static Calibration of Right Triaxial Force Transducer
(1 lbf = 4.448 N)

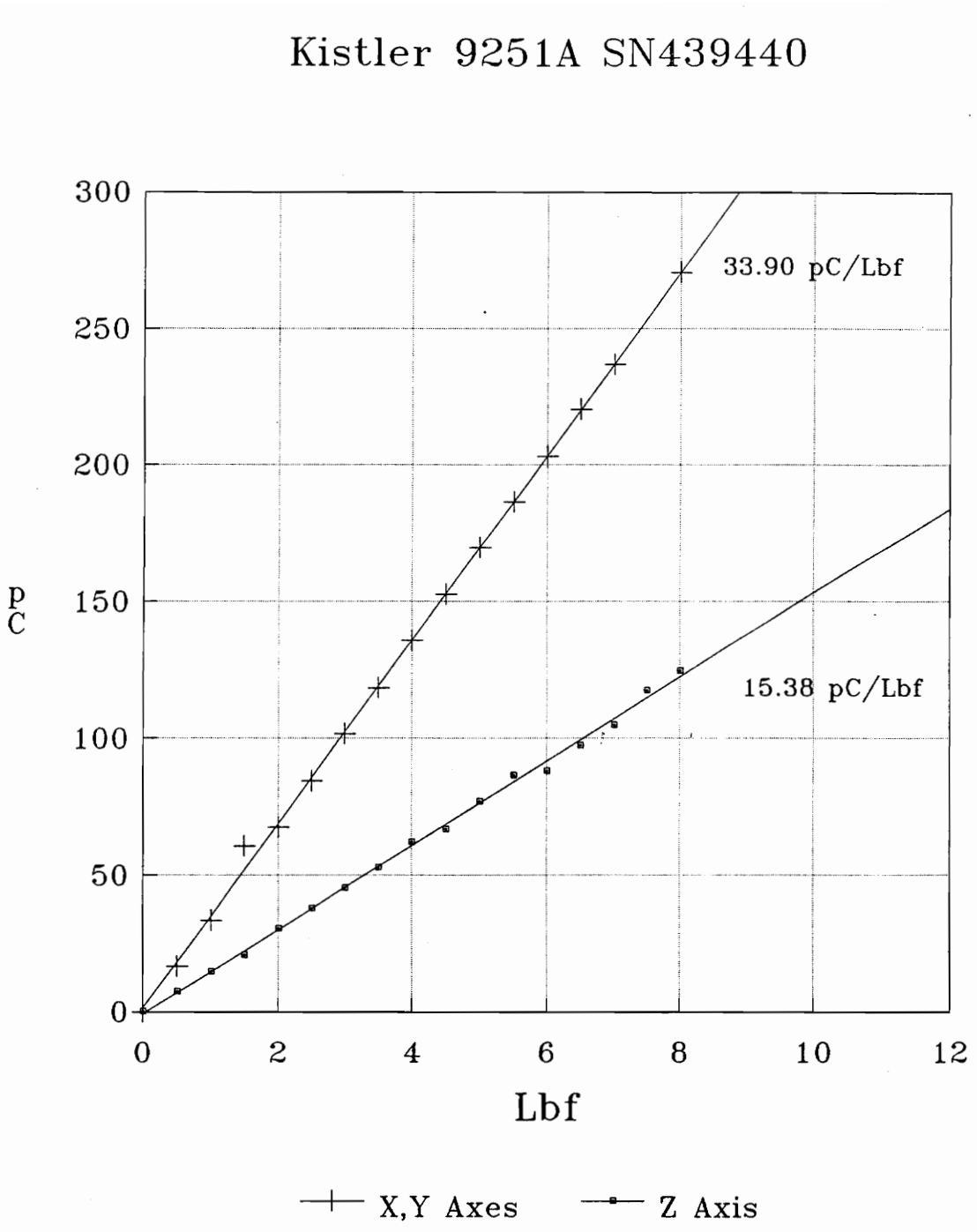

FIGURE A1.3. Static Calibration of Left Triaxial Force Transducer
(1 lbf = 4.448 N)

APPENDIX 2.
DIAGRAM OF TRIGGER CIRCUIT

As discussed in section 4.1.5, a trigger circuit was designed and built by Billy Shephard of Virginia Tech to provide for correct triggering of the H25A data acquisition. This circuit is shown in Fig. A2.1. Further discussion can be seen in section 4.1.5.

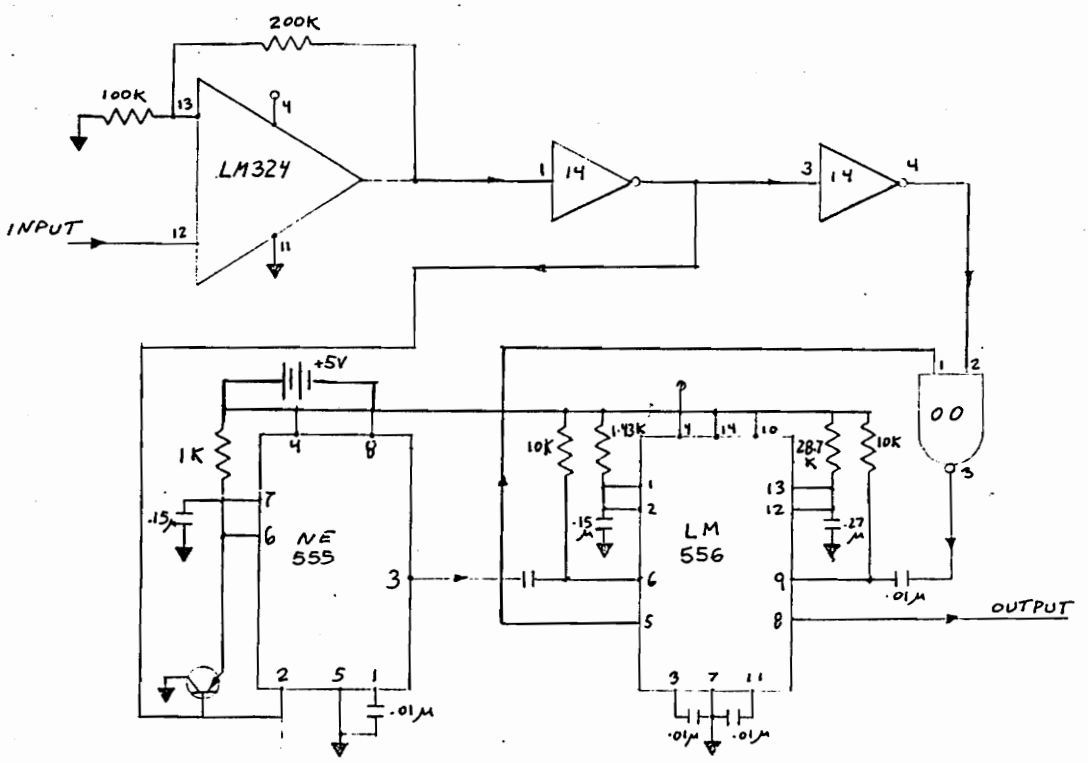

FIGURE A2.1. Schematic of Trigger Circuit
(Courtesy of Billy Shepherd, VPI)

APPENDIX 3.
STATISTICAL STUDY OF H25A SHELL RESONANCES

A3.1. PURPOSE OF STUDY

The purpose of the following study is to investigate the statistical parameters of the Bristol H25A compressor shell's natural frequencies. This includes finding the mean value, sample standard deviation, and 90% confidence intervals from experimental measurements for the natural frequencies up to 2000 Hz. This will hopefully provide a more useful dynamic model of the compressor shell than simply listing resonance values from a single test.

Although this study was conducted on empty compressor shells (shells without any compressor assemblies inside), it is assumed that the dynamics of complete compressors vary statistically as well.

A3.2. PROCEDURE

The natural frequencies of the compressor shells were found by exciting the shells with an impact hammer and measuring their responses with an accelerometer. The data was acquired by an FFT analyzer and processed to display the frequency values of the resonant peaks found on the frequency response functions. Ten averages were taken for each shell test. Resonances were determined to within 5 Hz, the resolution of the analyzer.

In all, five shells were tested. One was tested twice to check repeatability. All shells were mounted in the same manner, and excitation and response locations were also the same.

A3.3. RESULTS

Nineteen natural frequencies were identified which were consistently seen in all five shells. These are listed in Table A3.1, denoted as "peak number". Several other frequencies were seen only in a few of the shells, and could not be included in the analysis.

Table A3.1 lists the natural frequencies of each shell in Hz, the mean and standard deviation for each natural frequency, and the t distribution 90% confidence interval about the mean. The average of all standard deviations was 14.8 Hz. This value is also approximately the average +/- Hz value about the mean of any given natural frequency assuming a 90% level of confidence.

The repeatability check, done on shell C, showed no significant variation in any natural frequencies from trial to trial when 10 averaged spectrums were compared.

A3.4. CONCLUSIONS

From the results, the following conclusions are reached:

1. Variations in shell natural frequencies from shell to shell are not necessarily negligible.

2. Repeatability checks show that differences form shell to shell are inherent to the shells and not the test procedure.

3. Standard deviations of natural frequencies are not the same; thus some frequencies are more variable from shell to shell than others.

4. No trend is immediately evident in natural frequency variation; i.e. "higher frequencies tend to be more variable".

Based on these conclusions, it can be said that the variability of dynamic response is an important consideration when correlation of theoretical models and experimental

results is attempted. The variability of dynamic response is also important when attempting to compare a modified compressor shell to another non-modified shell.

TABLE A3.1. Results of H25A Shell Statistical Study
(All values in Hz)

PK. #	SHELL A	SHELL B	SHELL C	SHELL D	SHELL E	MEAN	STD DEV	90% LOWER	90% UPPER	NOTES
1	645	640	665	660	670	656	12.9	644	668	
2	745	730	760	745	760	748	12.5	736	760	A
3	910	945	940	935	950	936	15.6	921	951	A
4	1020	1050	1060	1045	1060	1047	16.4	1031	1063	B
5	1055	1095	1140	1150	1145	1117	41.0	1078	1156	
6	1130	1135	1160	1195	1165	1157	26.1	1132	1182	
7	1220	1240	1230	1220	1235	1229	8.9	1220	1238	
8	1295	1280	1275	1270	1280	1280	9.4	1271	1289	A,C
9	1340	1345	1330	1320	1330	1333	9.7	1324	1342	
10	1410	1420	1405	1395	1410	1408	9.1	1399	1417	
11	1475	1460	1465	1450	1470	1464	9.6	1455	1473	
12	1525	1555	1540	1530	1545	1539	11.9	1528	1550	
13	1545	1585	1595	1590	1590	1581	20.4	1562	1600	A,C
14	1630	1630	1650	1650	1630	1638	11.0	1628	1648	
15	1720	1705	1700	1700	1715	1708	9.1	1699	1717	C
16	1740	1760	1725	1740	1755	1744	13.9	1731	1757	
17	1820	1830	1815	1800	1825	1818	11.5	1807	1829	
18	1885	1850	1880	1850	1915	1876	27.2	1850	1902	
19	1950	1945	1955	1955	1960	1953	5.7	1948	1958	

NOTES:
A: Some peaks appear as double peaks while others do not
B: Very round peaks make precise identification difficult
C: Shape of peaks makes correlation difficult

APPENDIX 4.
TIME- AND FREQUENCY-DOMAIN OUTPUT OF TRANSDUCER DATA

The following plots are a complete set of data from the transducers listed in table 4.1. They are presented as time-domain plots with accompanying phase and magnitude frequency-domain plots.

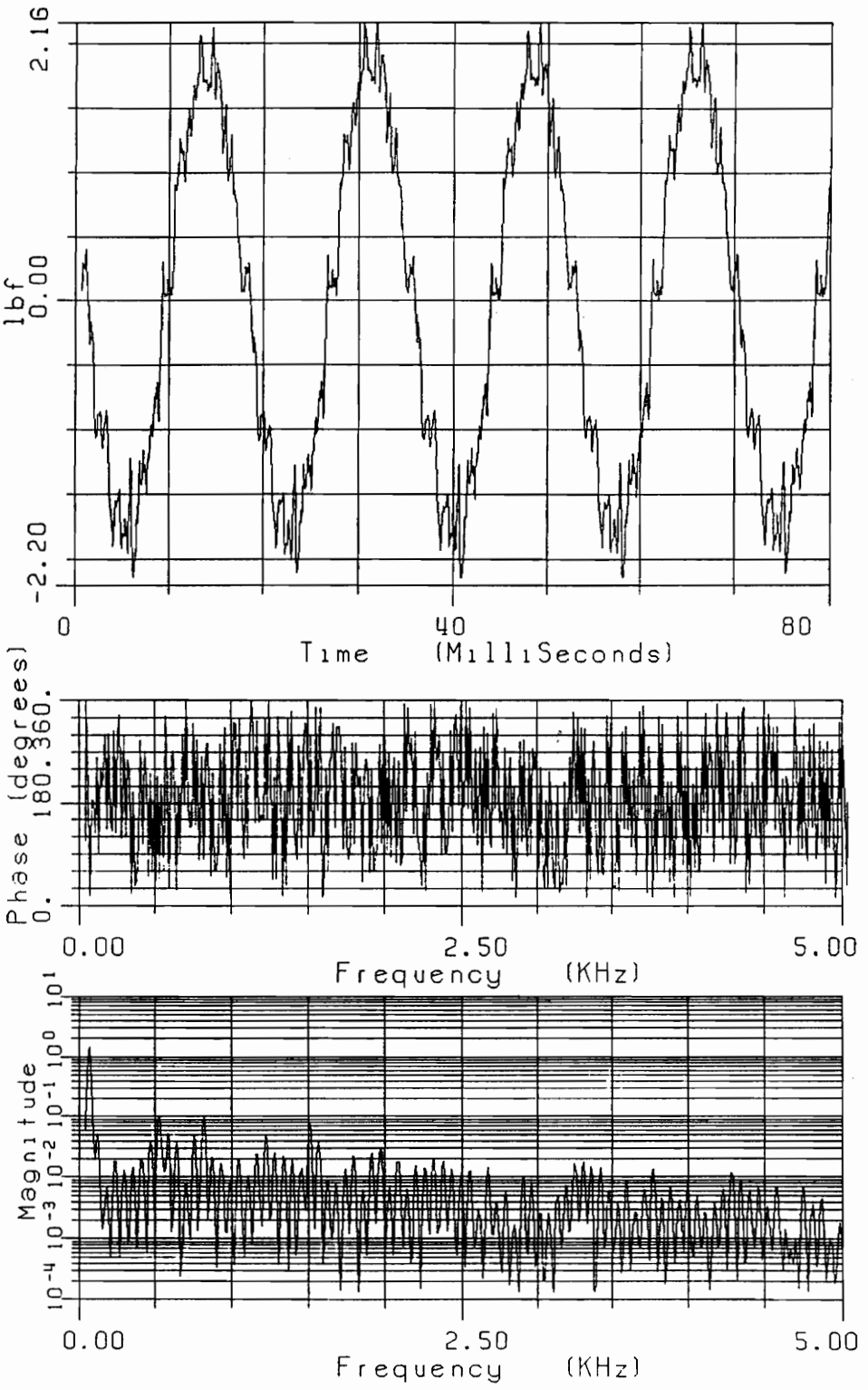

FIGURE A4.1. Time- and Frequency-Domain Right Spring Force Gage Data: X-Axis (1 lbf = 4.448 N)

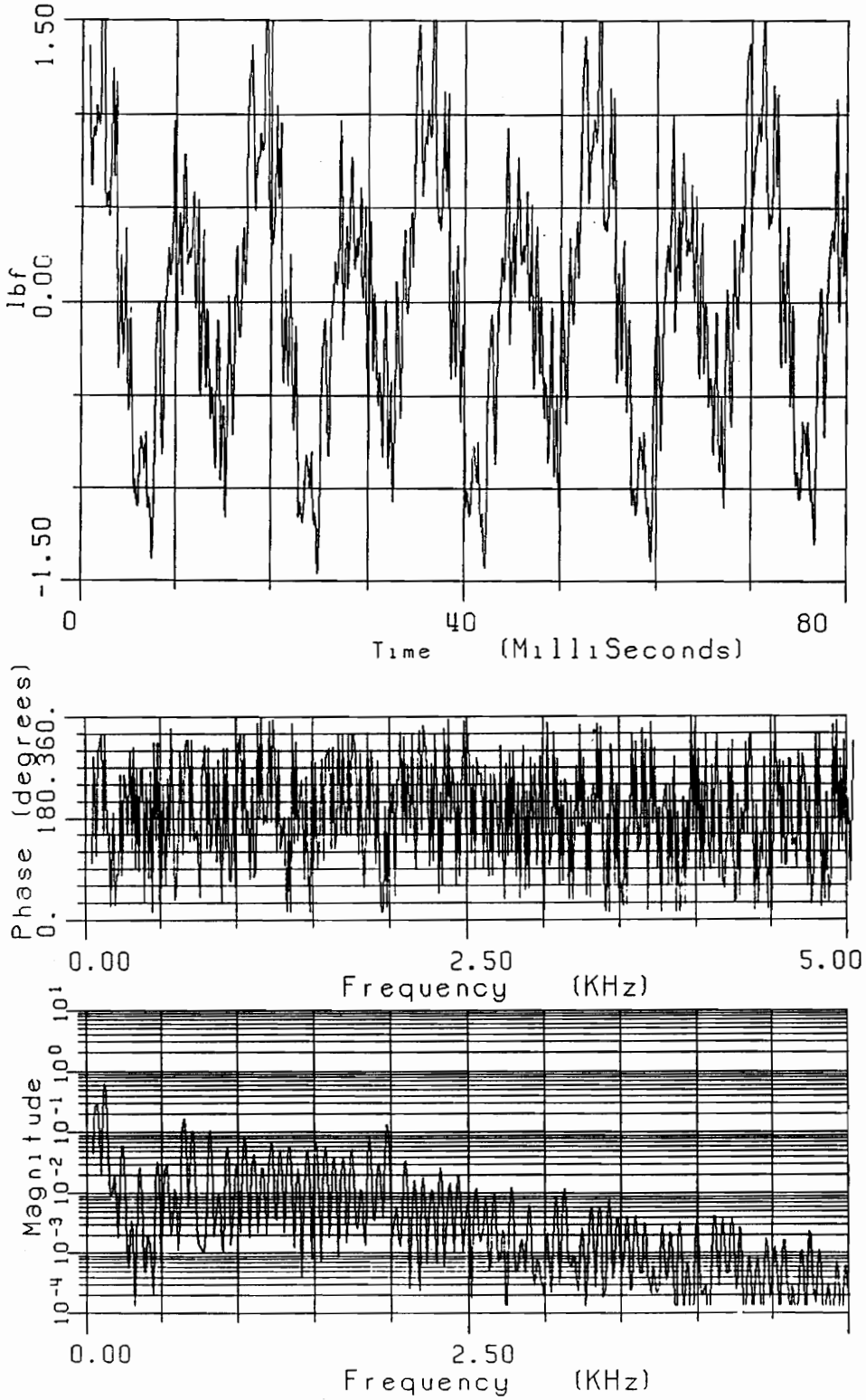

FIGURE A4.2. Time- and Frequency-Domain Right Spring Force Gage Data: Y-Axis (1 lbf = 4.448 N)

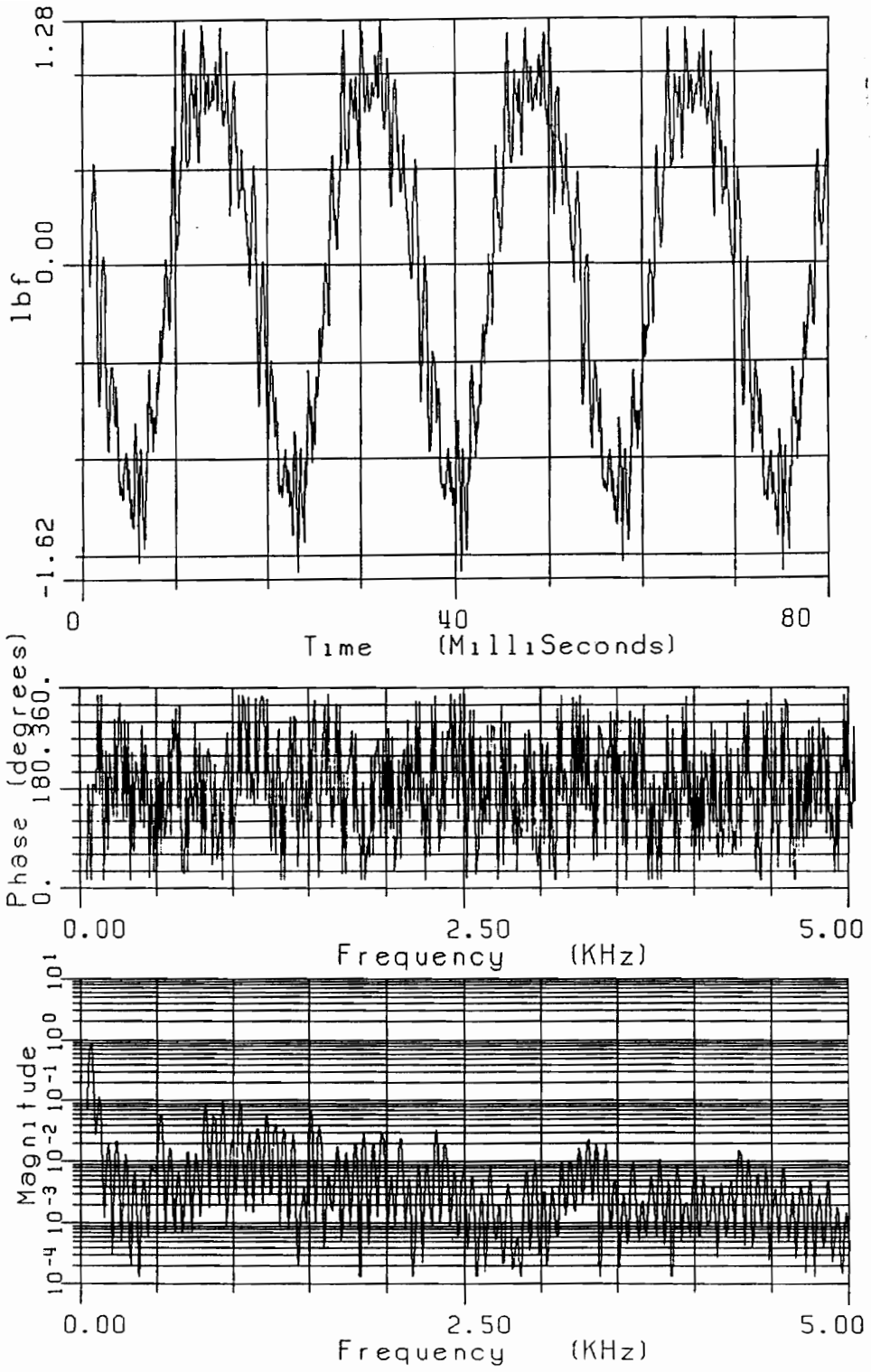

FIGURE A4.3. Time- and Frequency-Domain Right Spring Force Gage Data: Z-Axis (1 lbf = 4.448 N)

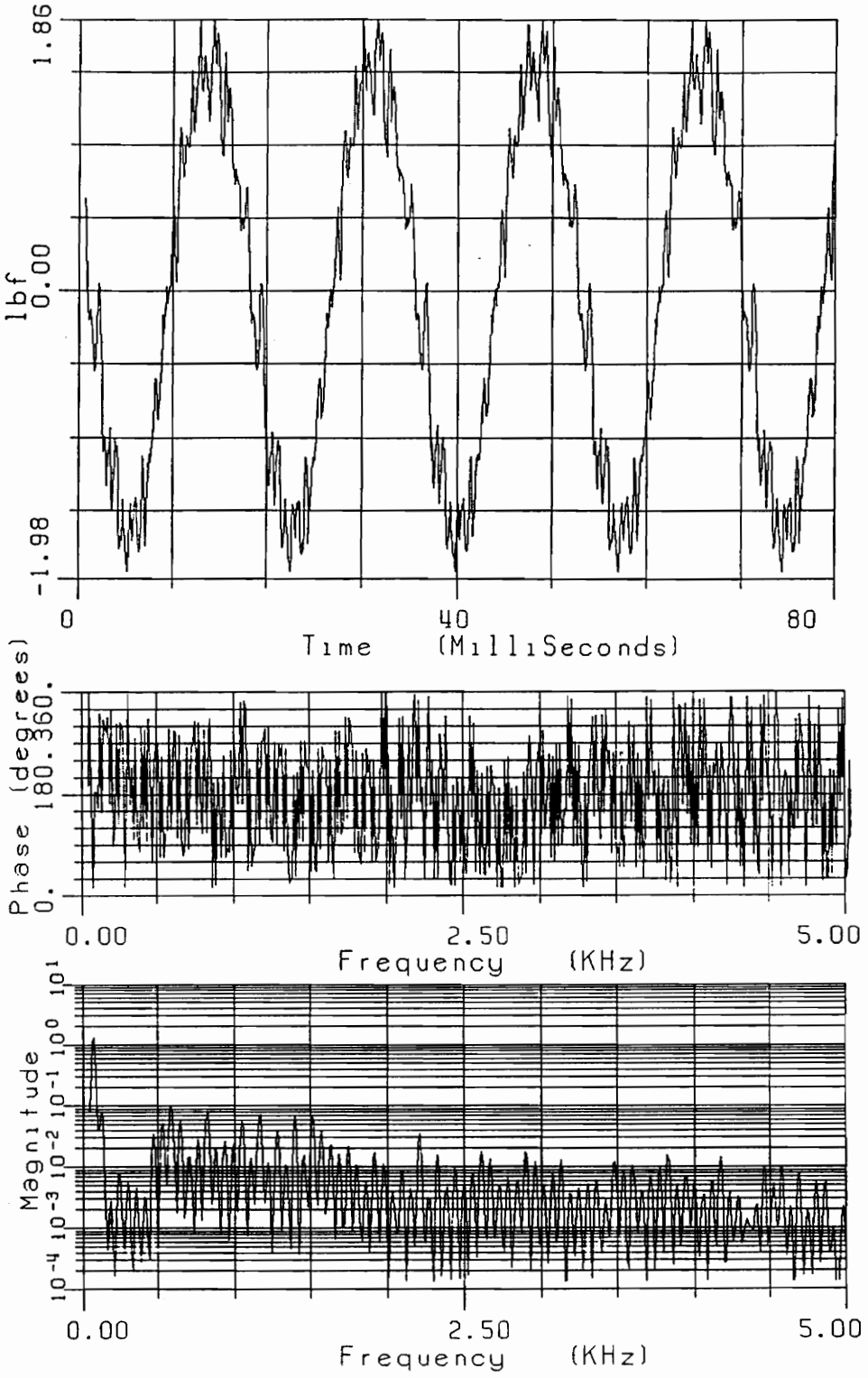

FIGURE A4.4. Time- and Frequency-Domain Left Spring Force Gage Data: X-Axis (1 lbf = 4.448 N)

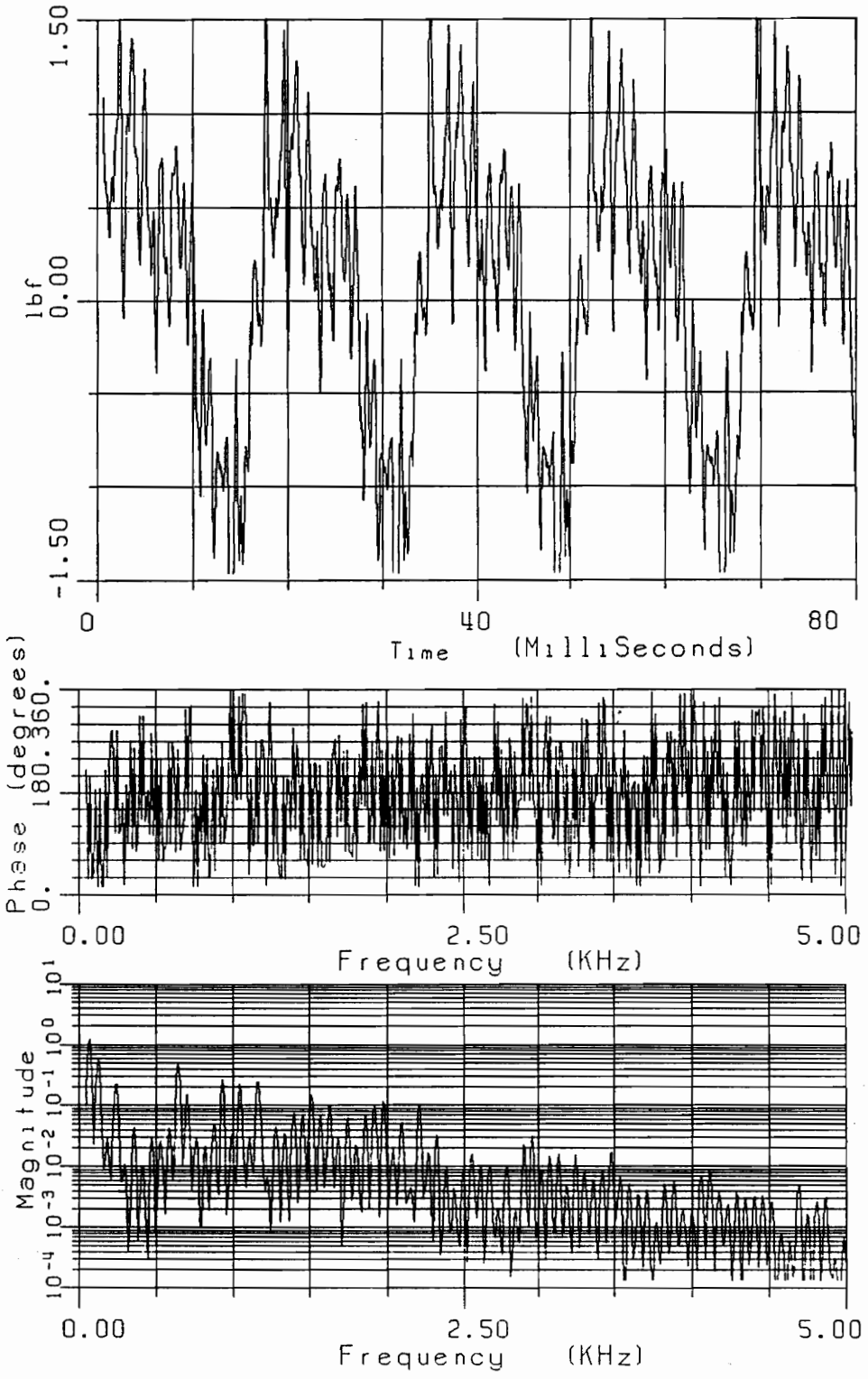

FIGURE A4.5. Time- and Frequency-Domain Left Spring Force Gage Data: Y-Axis (1 lbf = 4.448 N)

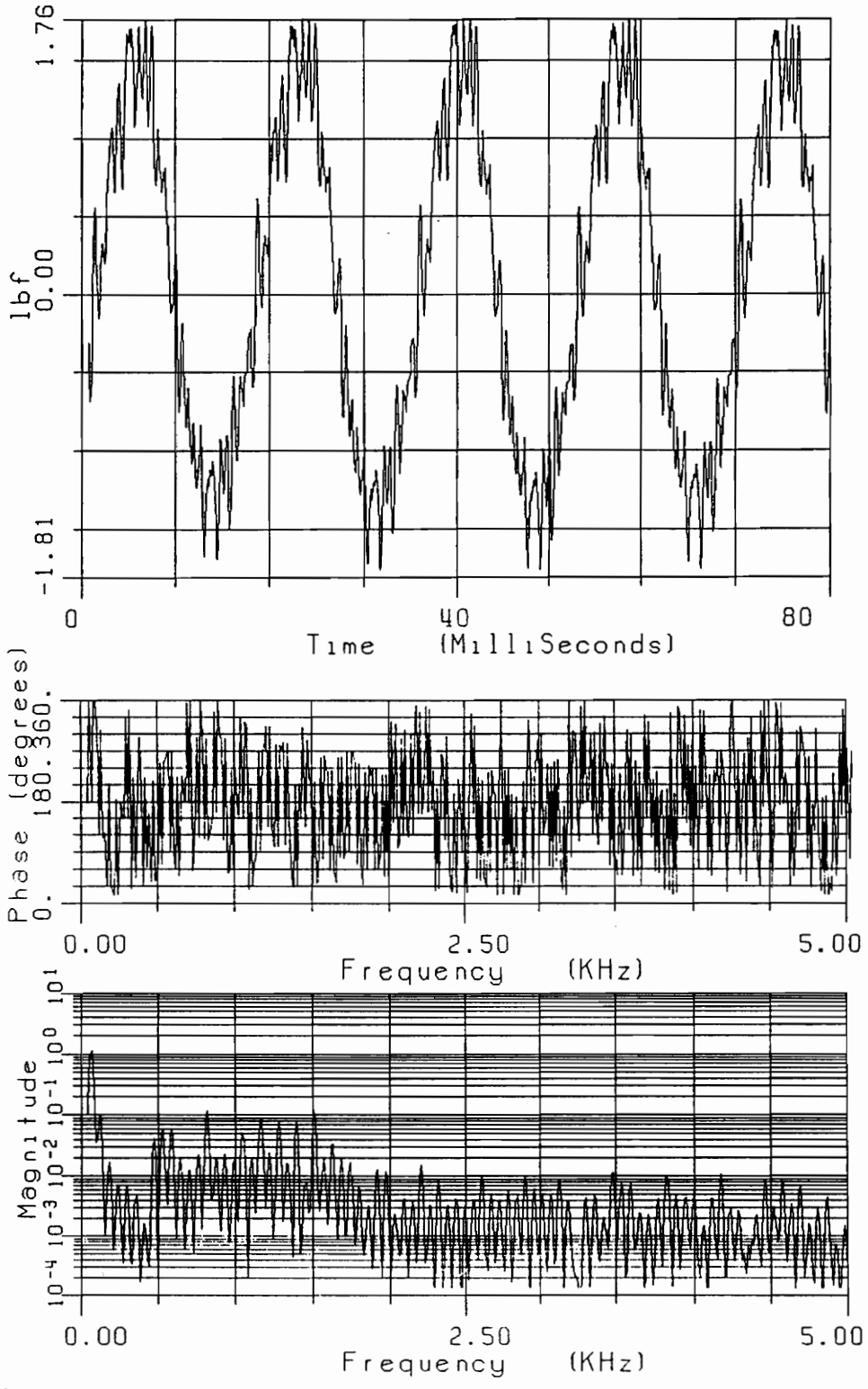

FIGURE A4.6. Time- and Frequency-Domain Left Spring Force Gage Data: Z-Axis (1 lbf = 4.448 N)

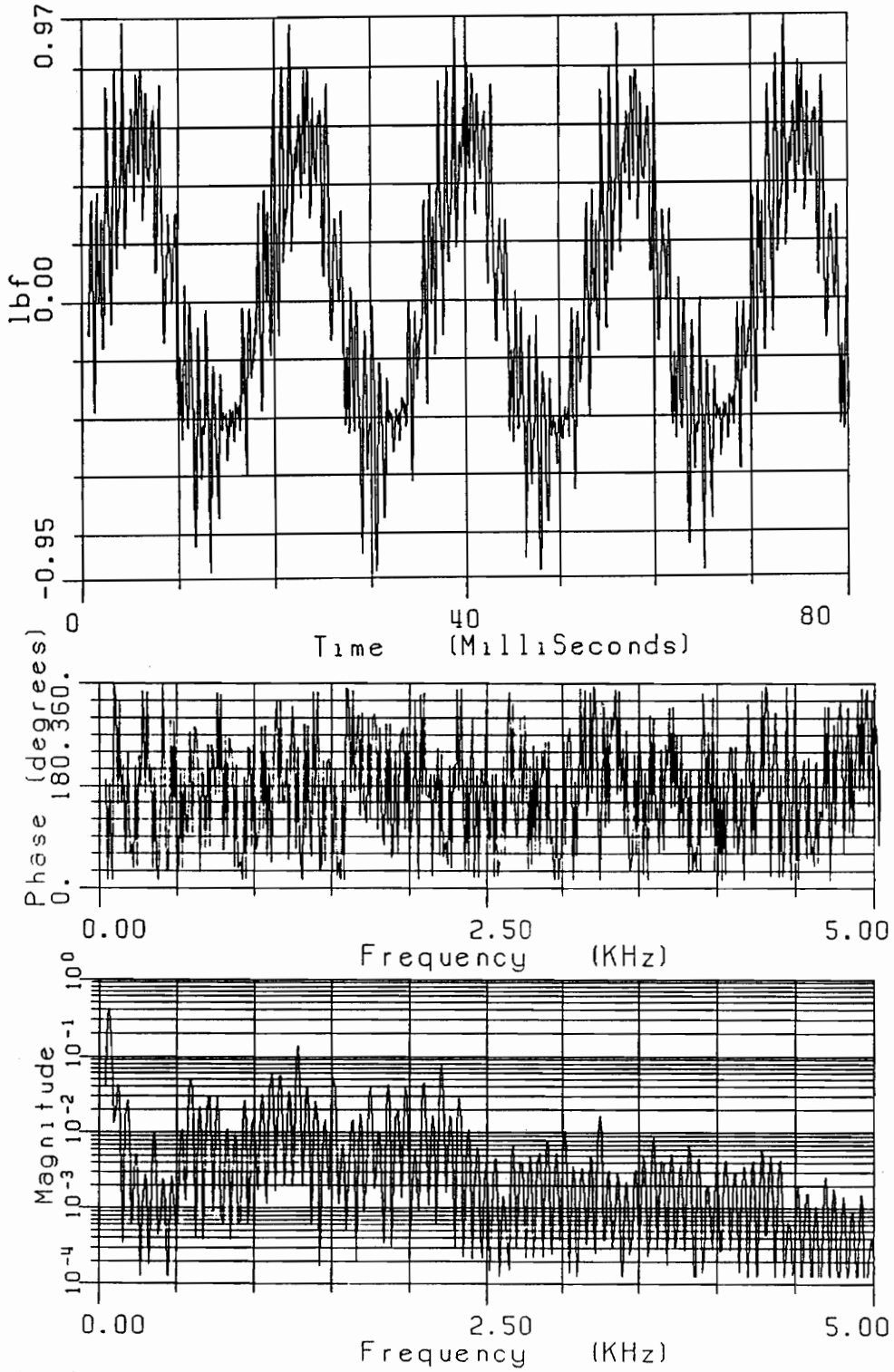

FIGURE A4.7. Time- and Frequency-Domain Top Spring Force Gage Data: X-Axis (1 lbf = 4.448 N)

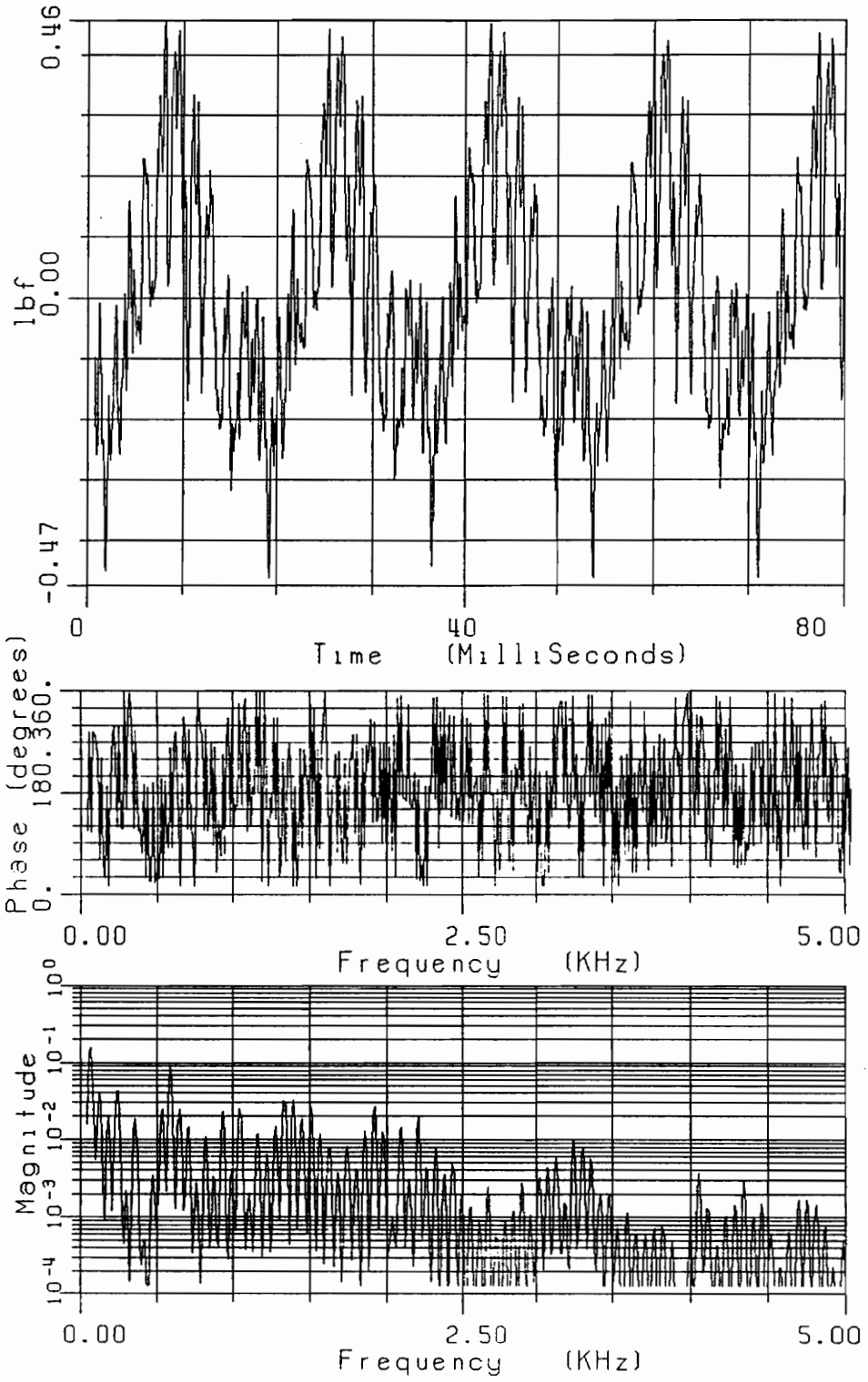

FIGURE A4.8. Time- and Frequency-Domain Top Spring Force Gage Data: Y-Axis (1 lbf = 4.448 N)

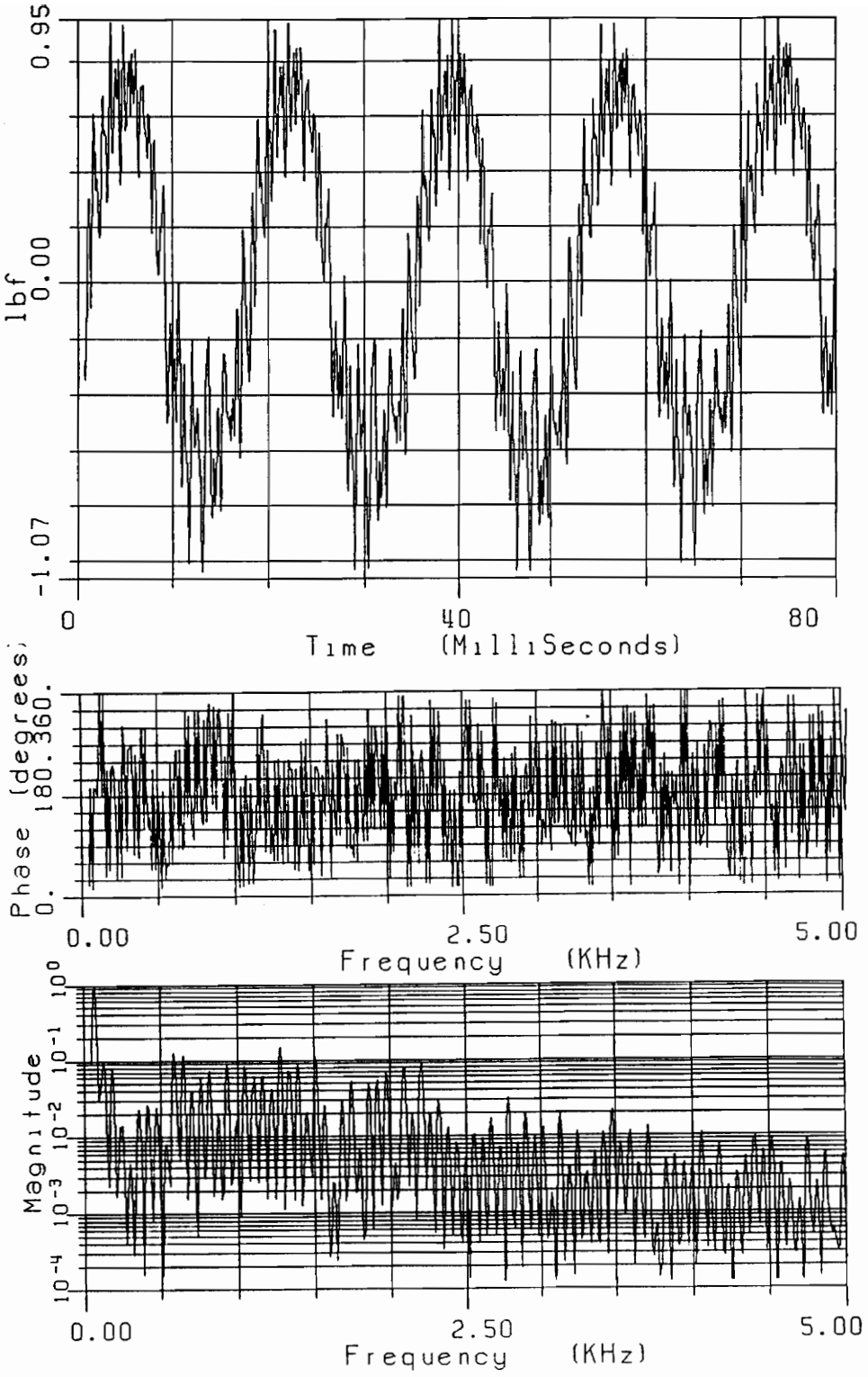

FIGURE A4.9. Time- and Frequency-Domain Top Spring Force Gage Data: Z-Axis (1 lbf = 4.448 N)

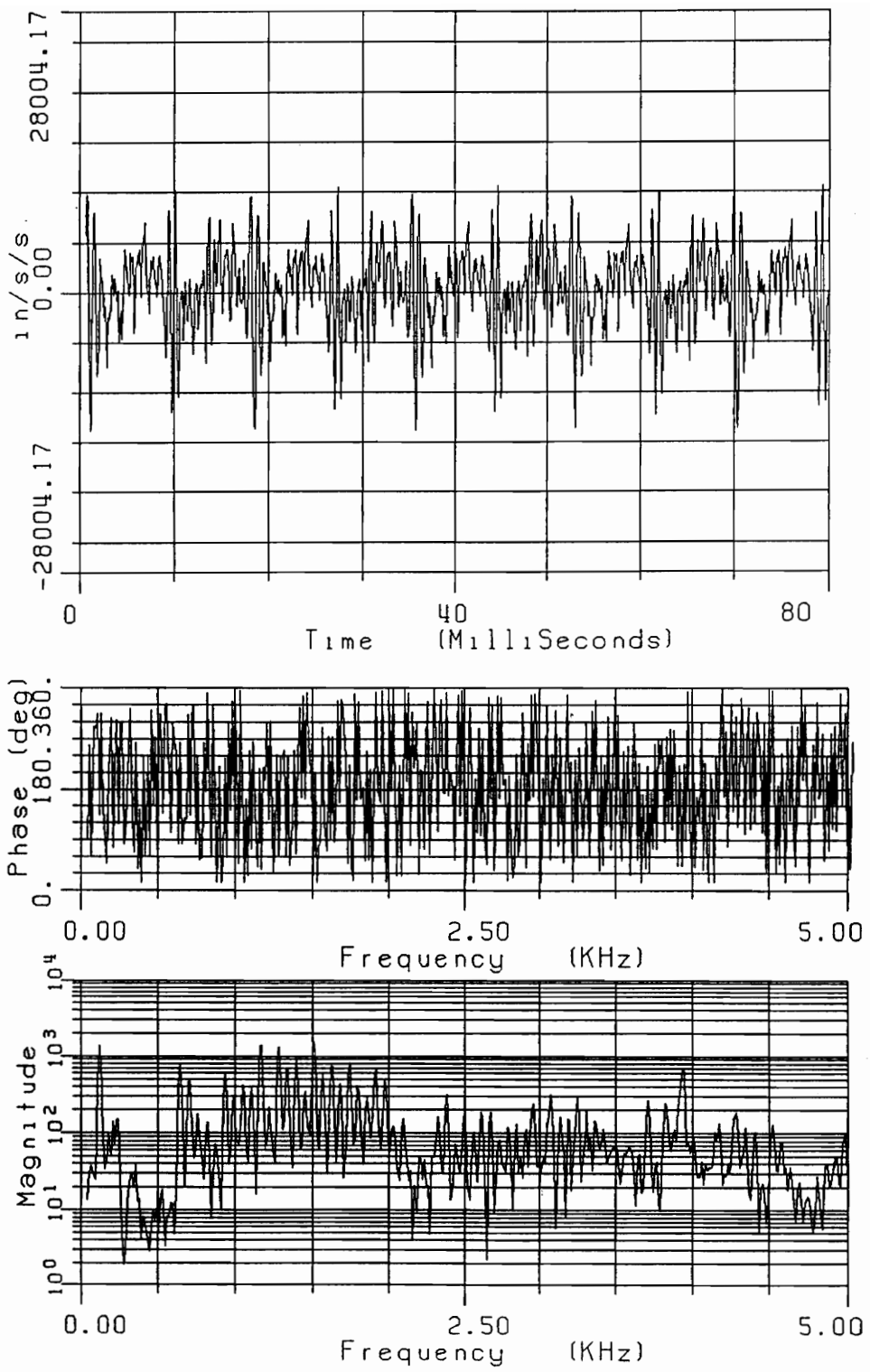

FIGURE A4.10. Time- and Frequency-Domain Shock-Loop Accelerometer Data (1 in/s/s = 25.4 mm/s/s)

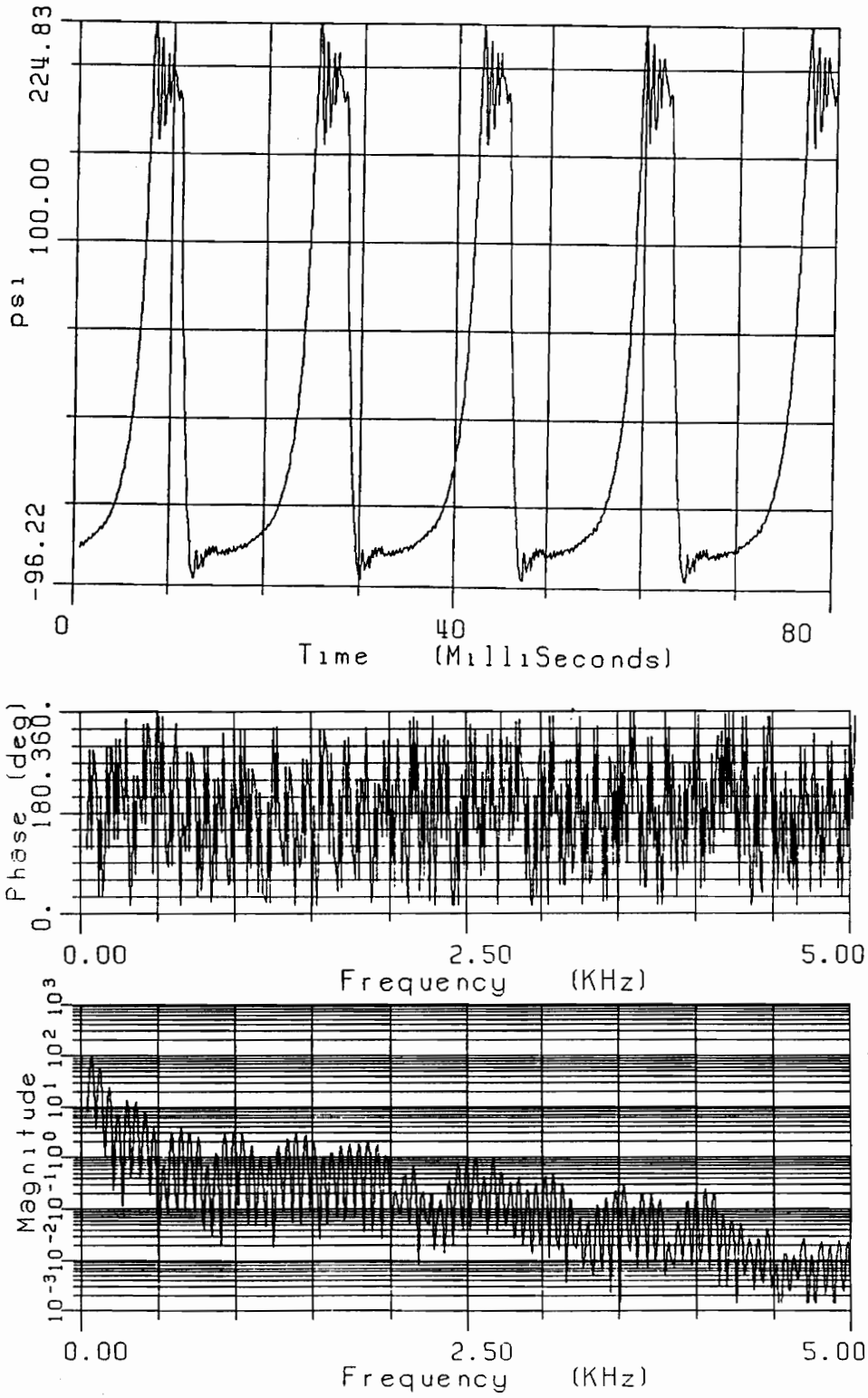

FIGURE A4.11. Time- and Frequency-Domain Top Cylinder Pressure Data (1 psi = 6894.8 Pa)

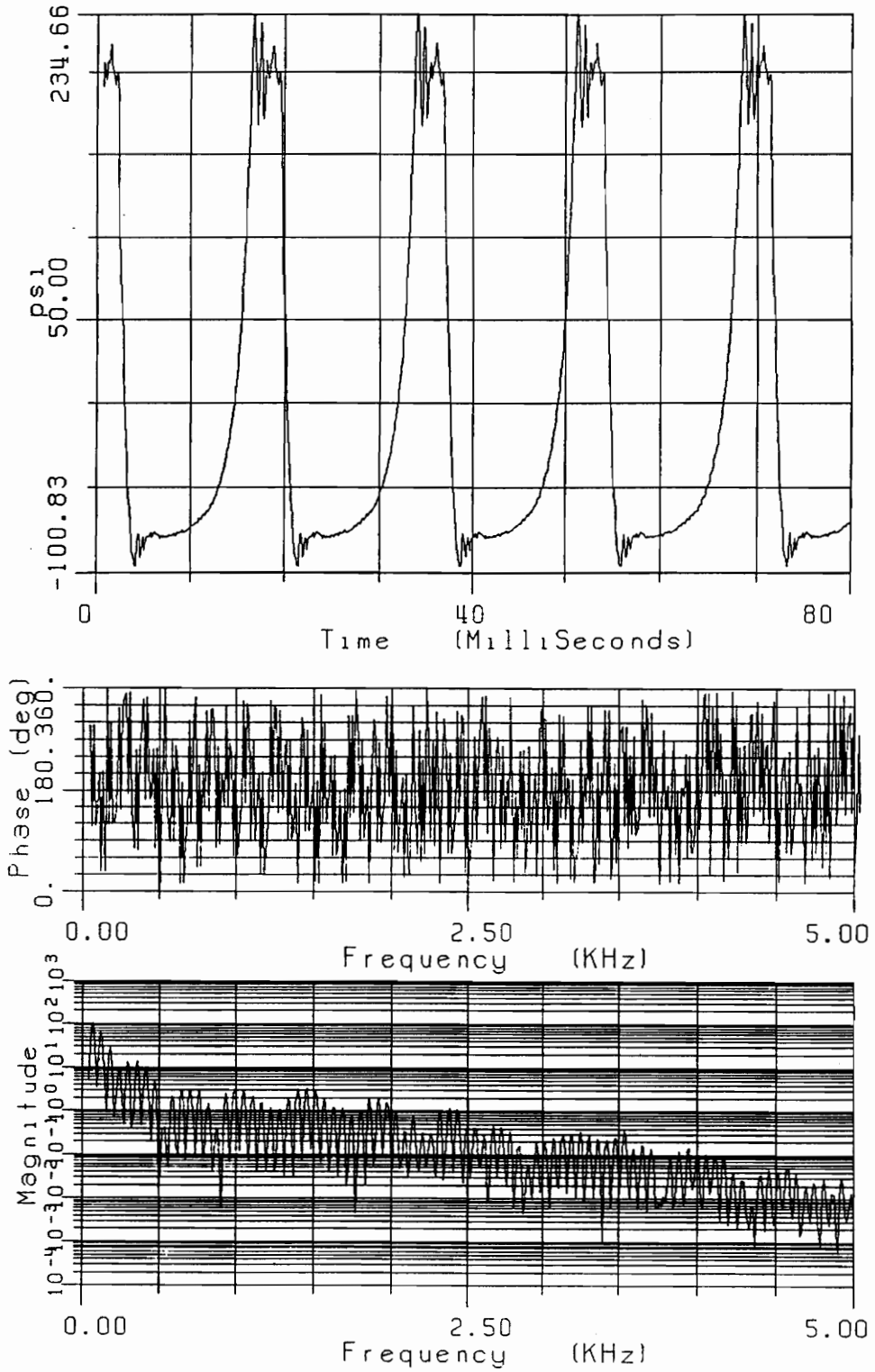

FIGURE A4.12. Time- and Frequency-Domain Bottom Cylinder Pressure Data (1 psi = 6894.8 Pa)

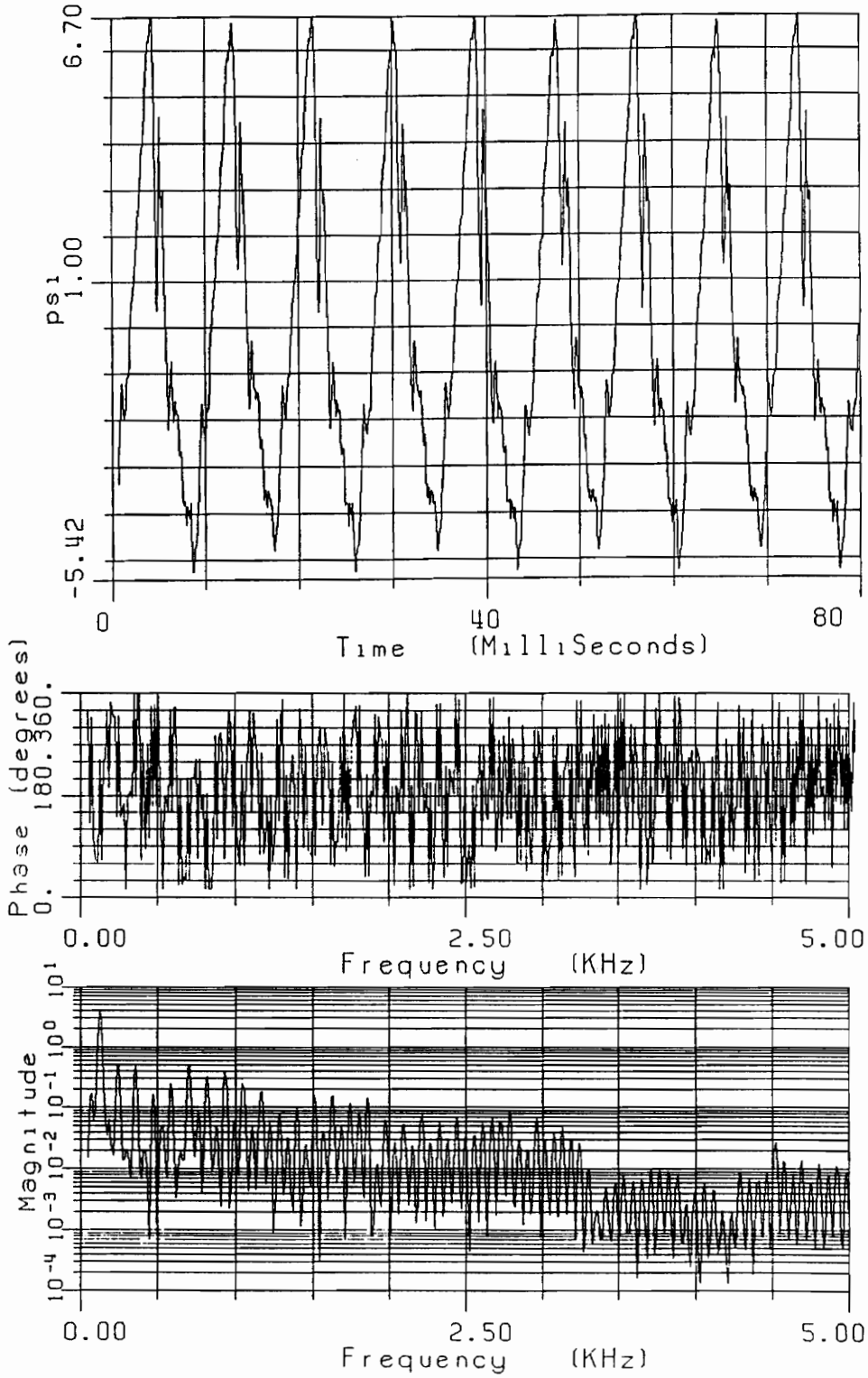

FIGURE A4.13. Time- and Frequency-Domain Suction Pressure Data (1 psi = 6894.8 Pa)

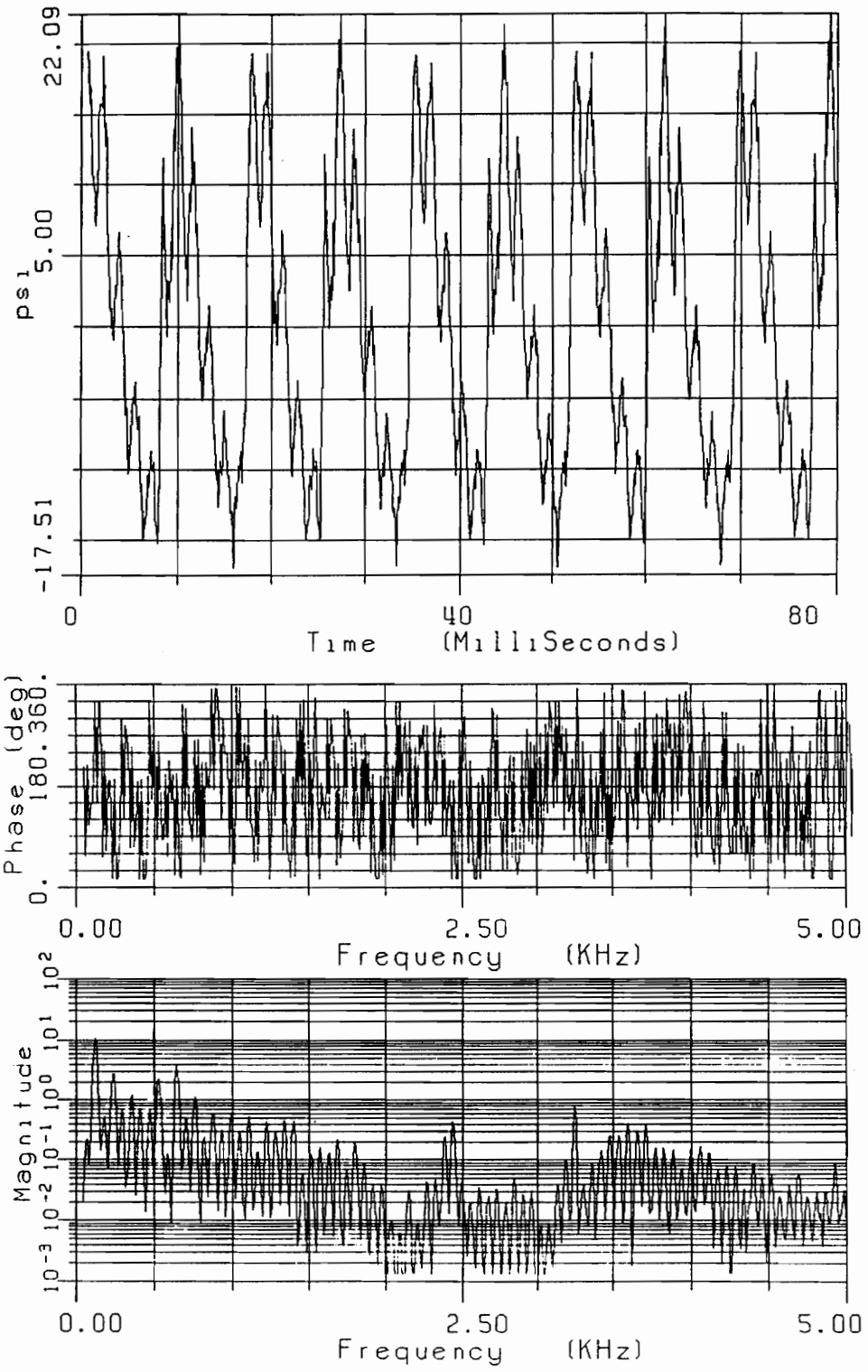

FIGURE A4.14. Time- and Frequency-Domain Exhaust Pressure Data
(1 psi = 6894.8 Pa)

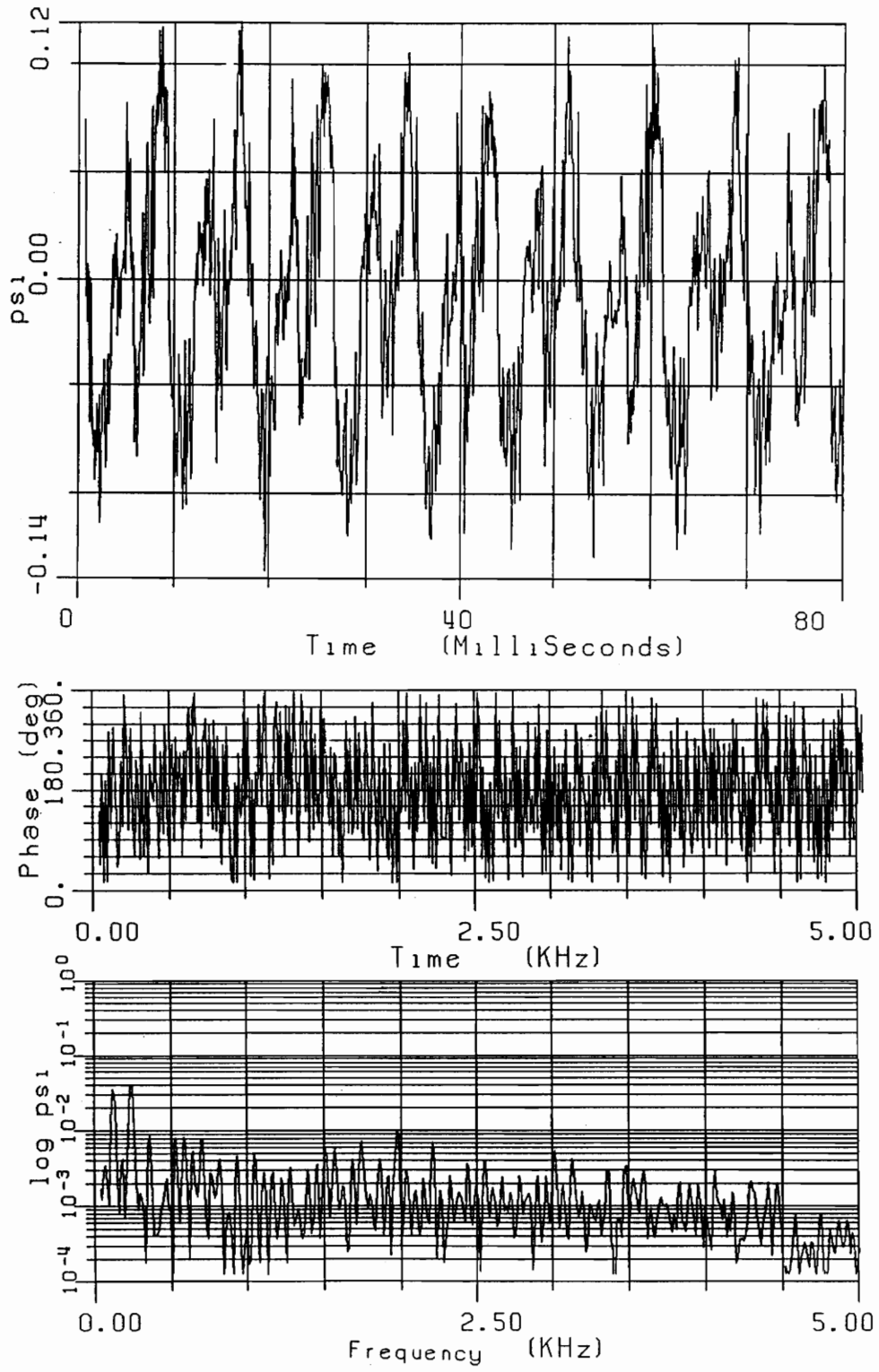

FIGURE A4.15. Time- and Frequency-Domain Housing Cavity Pressure Data (1 psi = 6894.8 Pa)

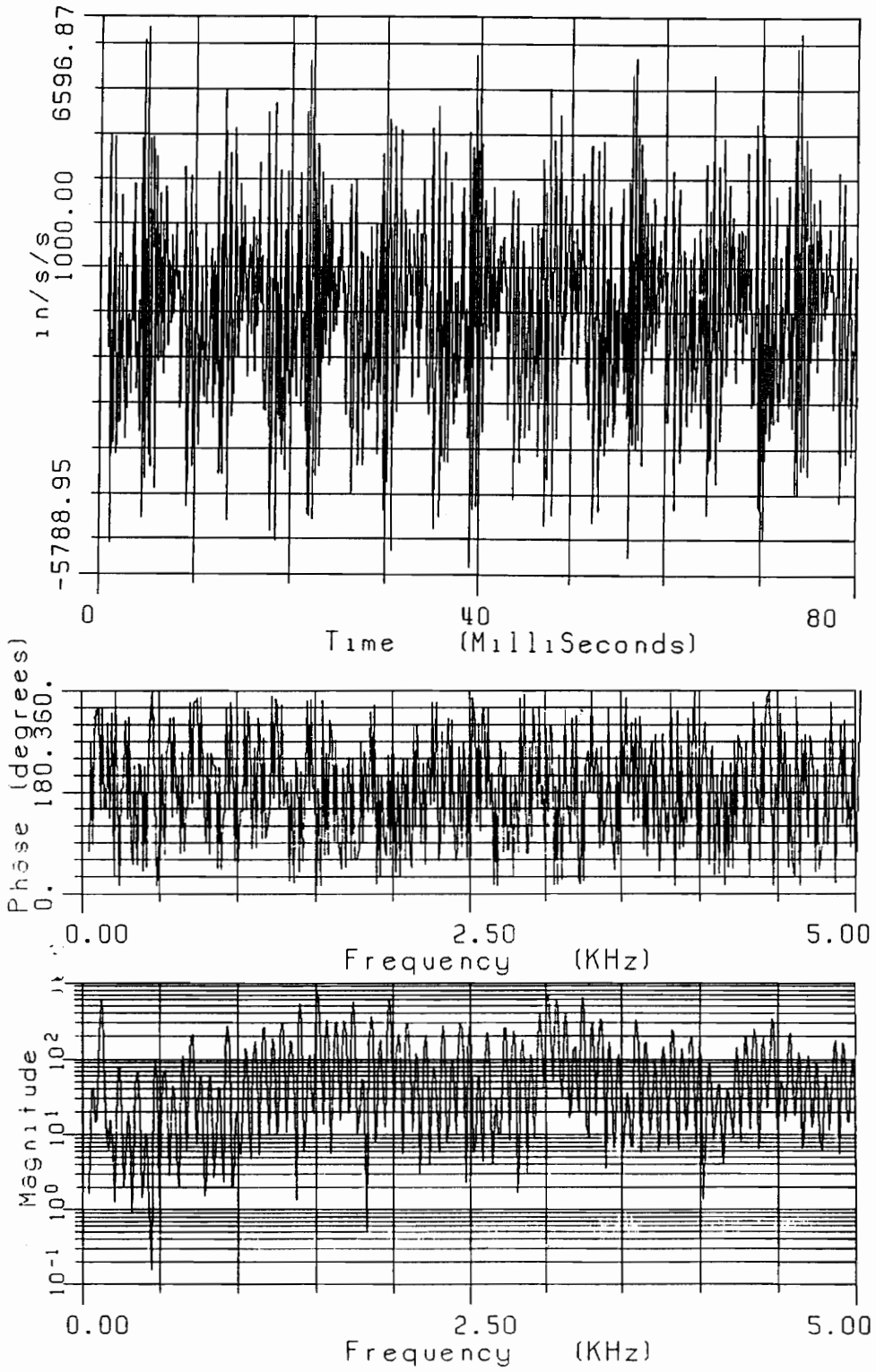

FIGURE A4.16. Time- and Frequency-Domain Motor Cap Accelerometer Data: X-Axis (1 in/s/s = 25.4 mm/s/s)

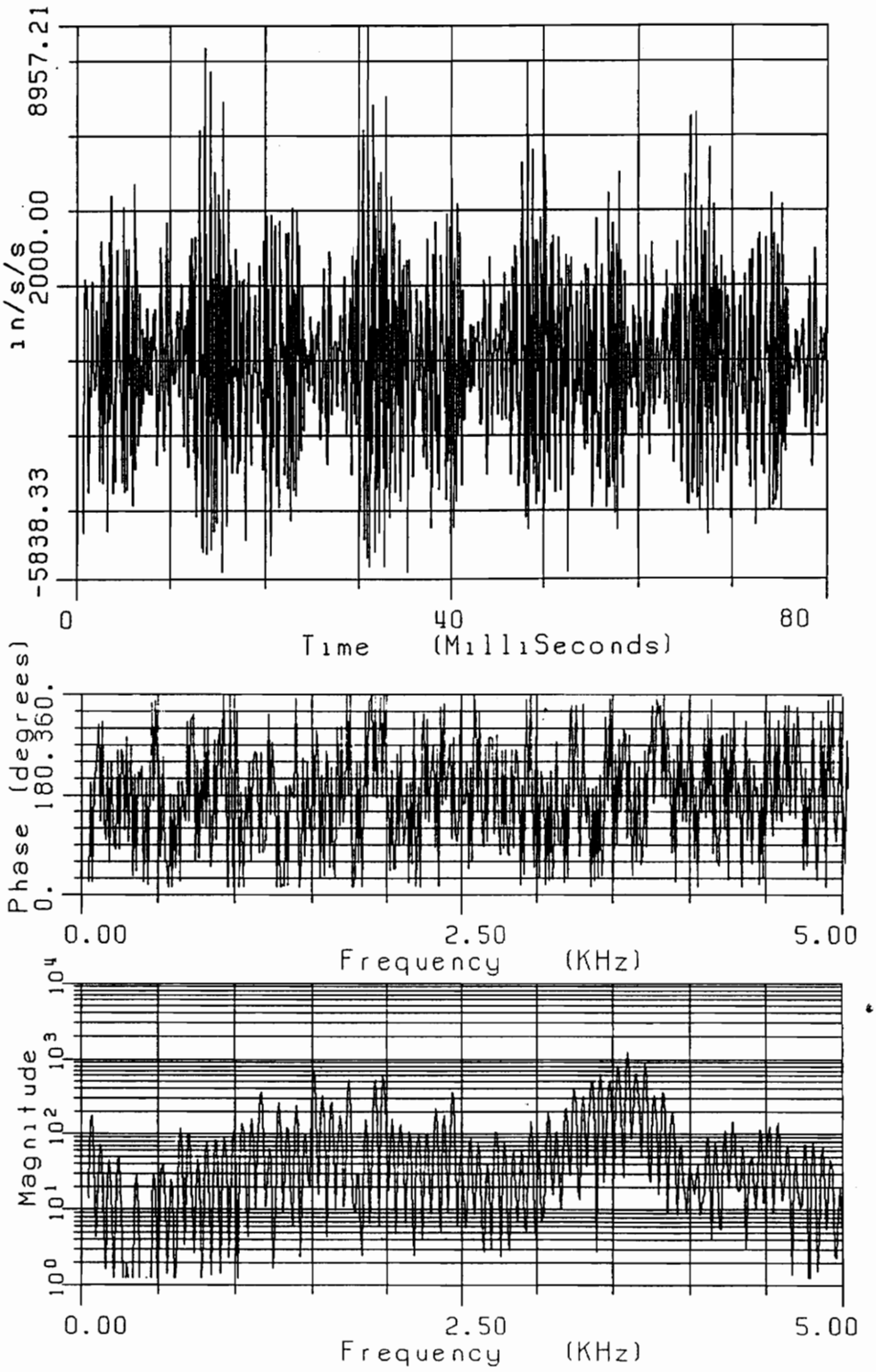

FIGURE A4.17. Time- and Frequency-Domain Motor Cap Accelerometer Data: Y-Axis (1 in/s/s = 25.4 mm/s/s)

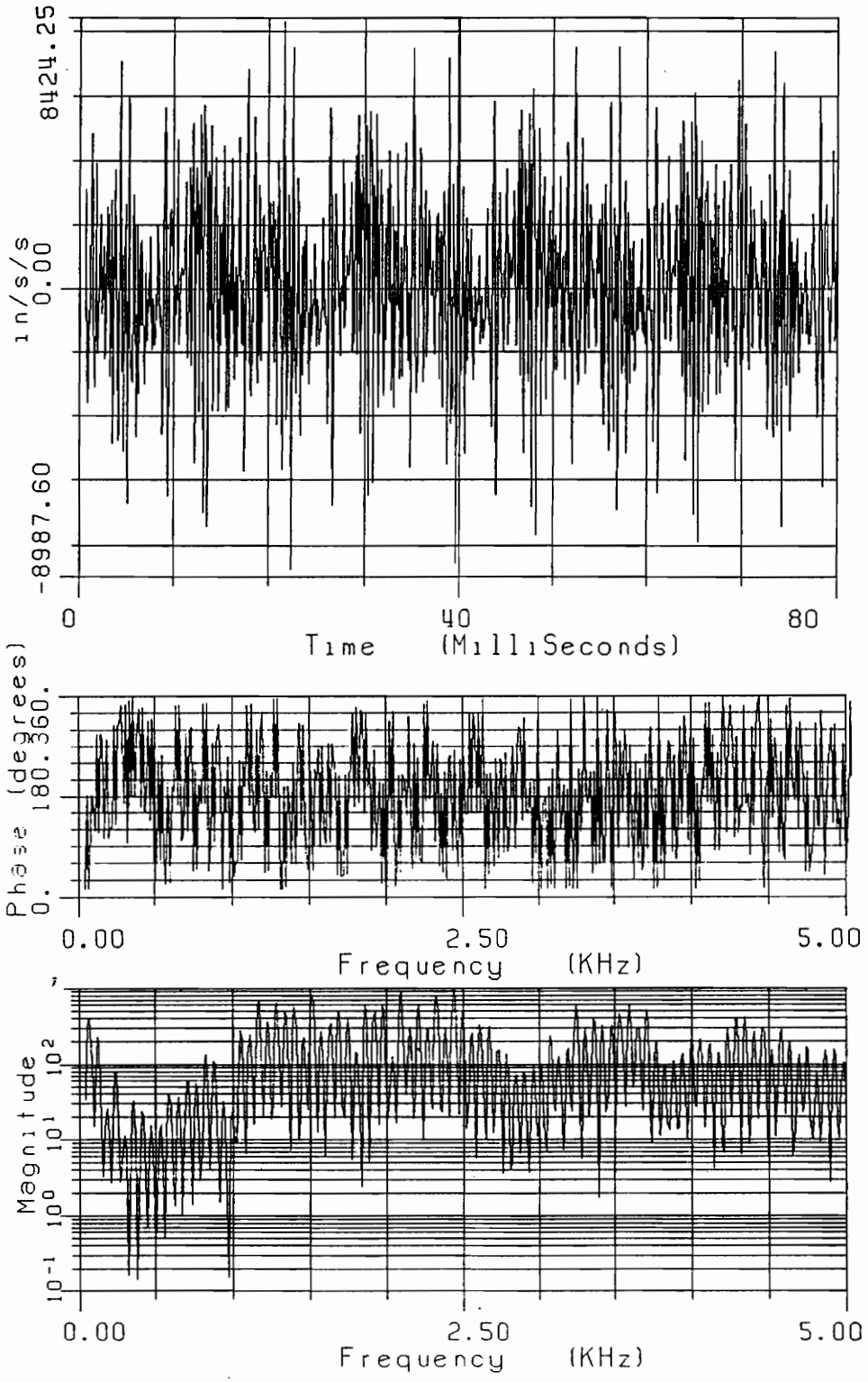

FIGURE A4.18. Time- and Frequency-Domain Motor Cap Accelerometer Data: Z-Axis (1 in/s/s = 25.4 mm/s/s)

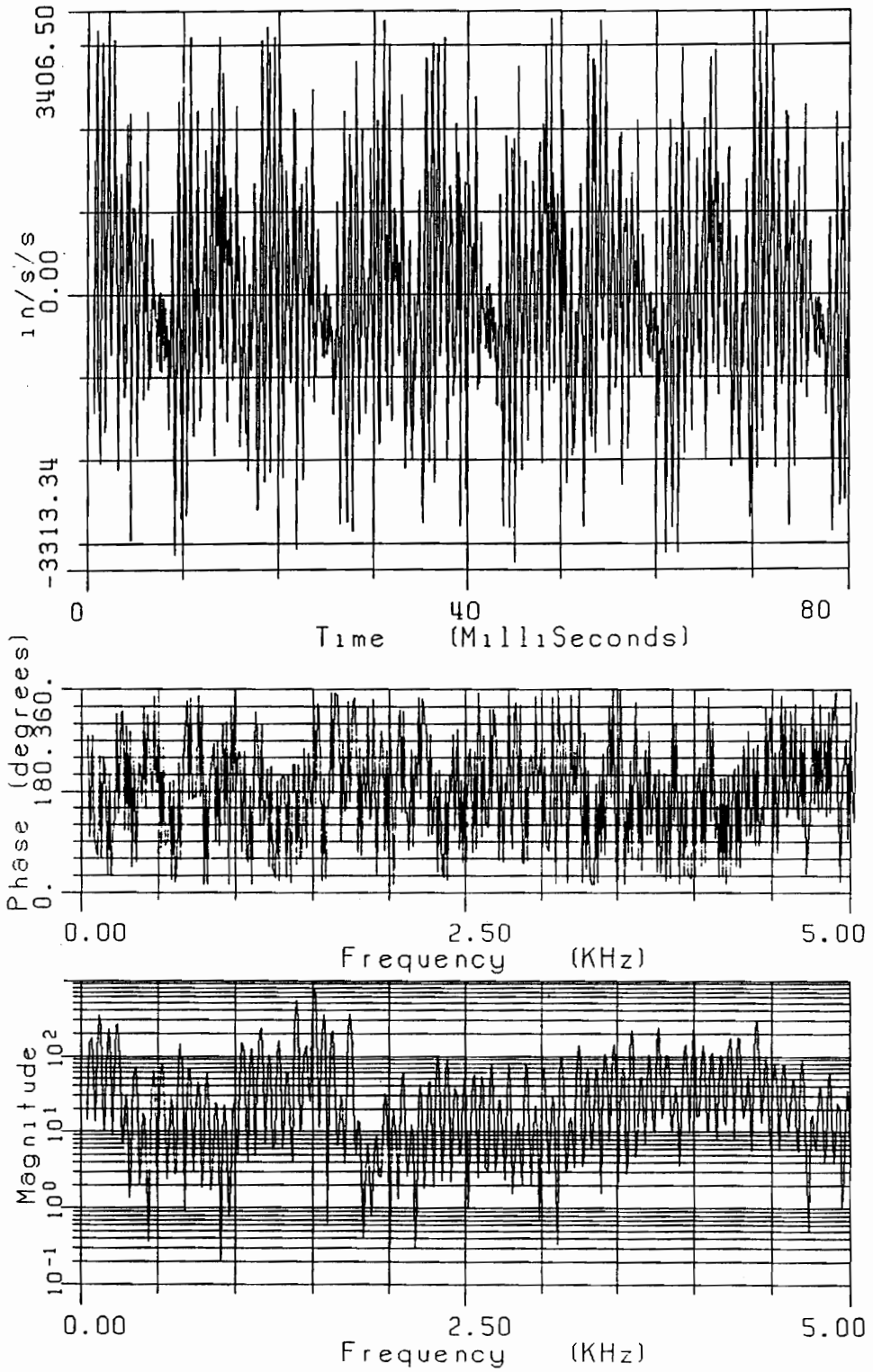

FIGURE A4.19. Time- and Frequency-Domain Crankcase Accelerometer Data: X-Axis (1 in/s/s = 25.4 mm/s/s)

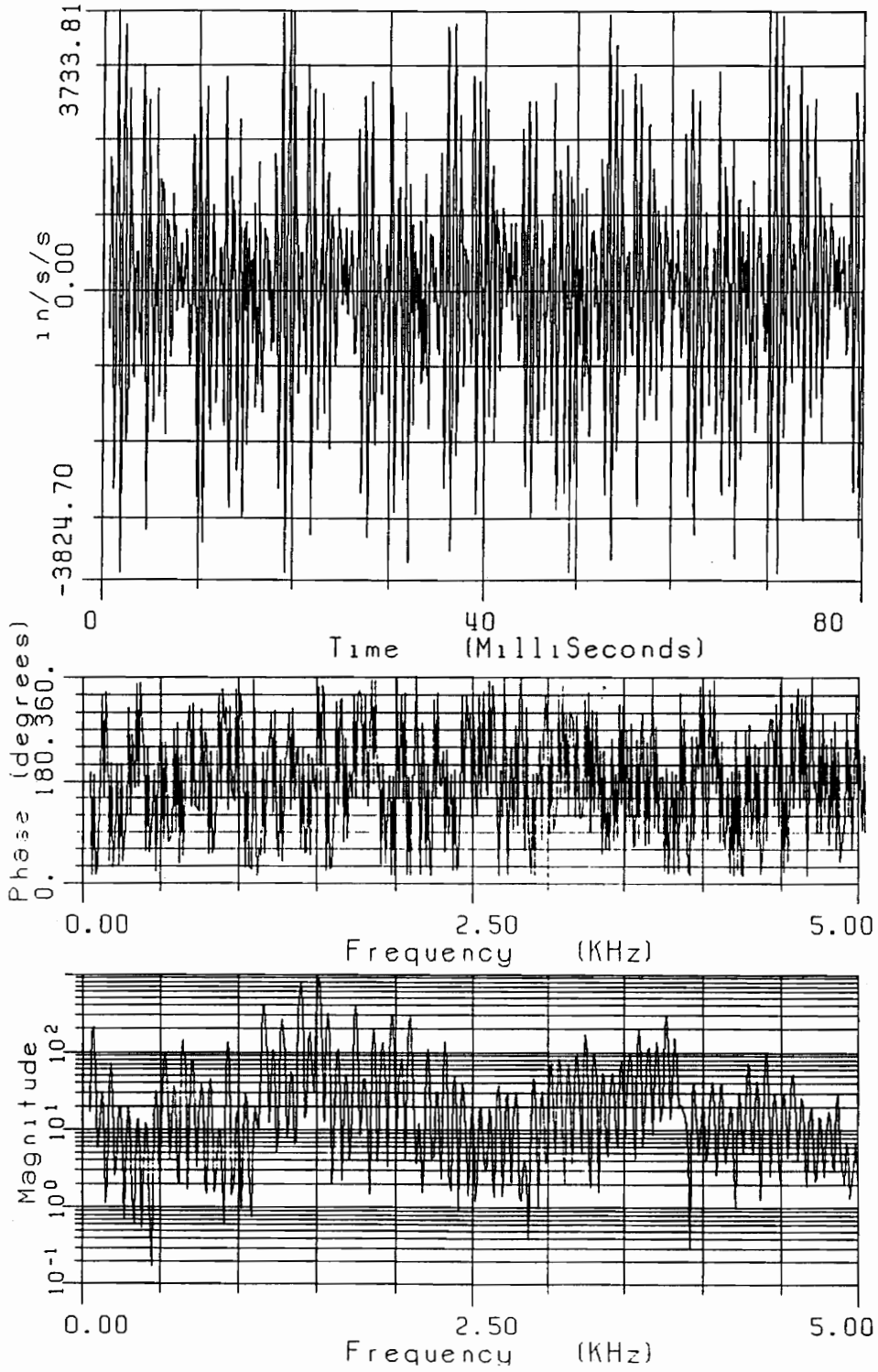

FIGURE A4.20. Time- and Frequency-Domain Crankcase Accelerometer Data: Y-Axis (1 in/s/s = 25.4 mm/s/s)

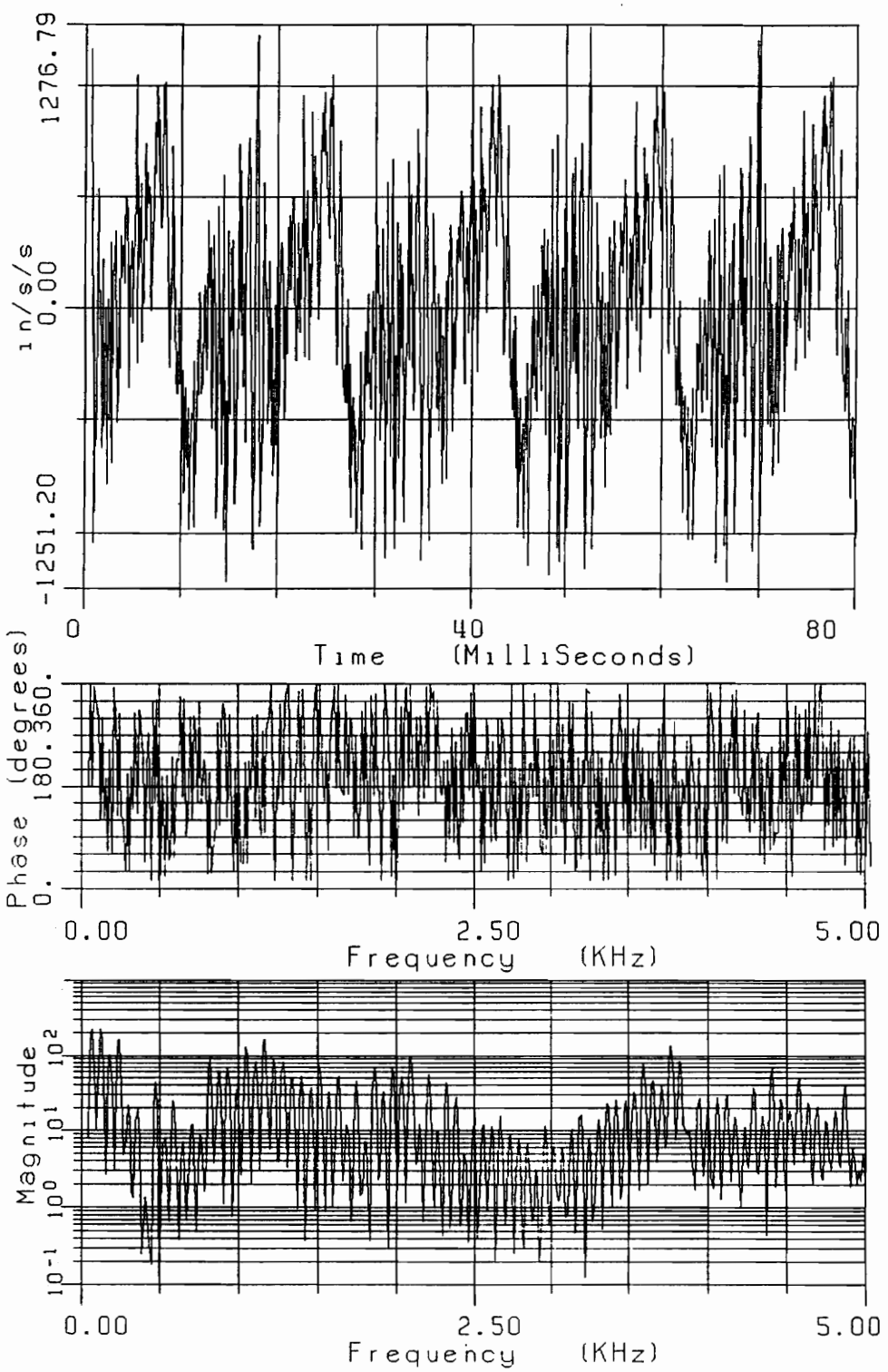

FIGURE A4.21. Time- and Frequency-Domain Crankcase Accelerometer Data: Z-Axis (1 in/s/s = 25.4 mm/s/s)

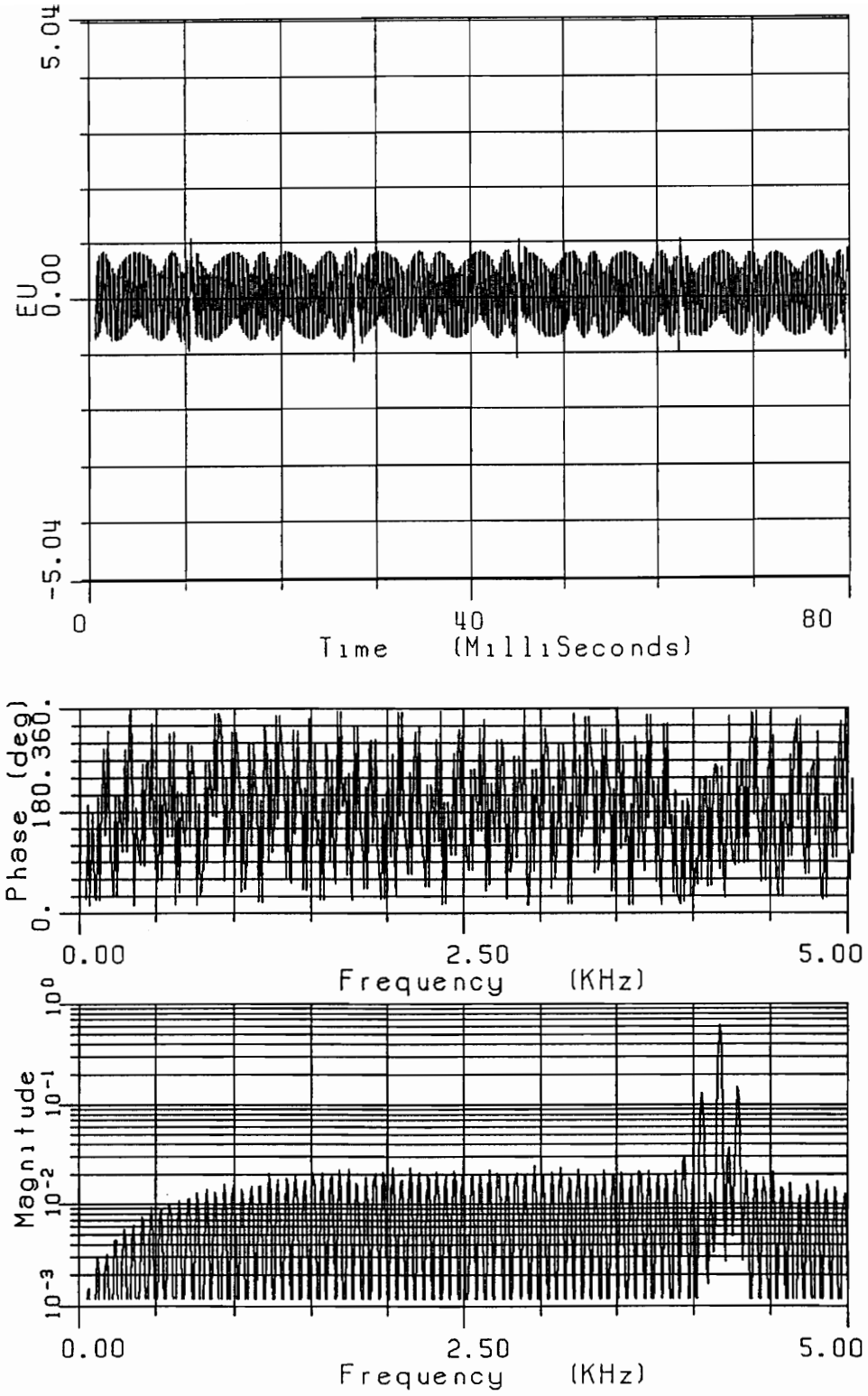

FIGURE A4.22. Time- and Frequency-Domain Crankshaft Gear Data

APPENDIX 5.
COMPRESSOR SOUND OUTPUT SPECTRA

Figure 5. 8 shows the compressor sound output spectra for the far-filed microphone test. The following figures present the spectra for the compressor long side, compressor short side, and compressor top microphone locations as shown in Figs. 4.15, 4.16. The plots display sound pressure level in un-weighted dB re 2.9×10^{-9} psi (20×10^{-6} Pa).

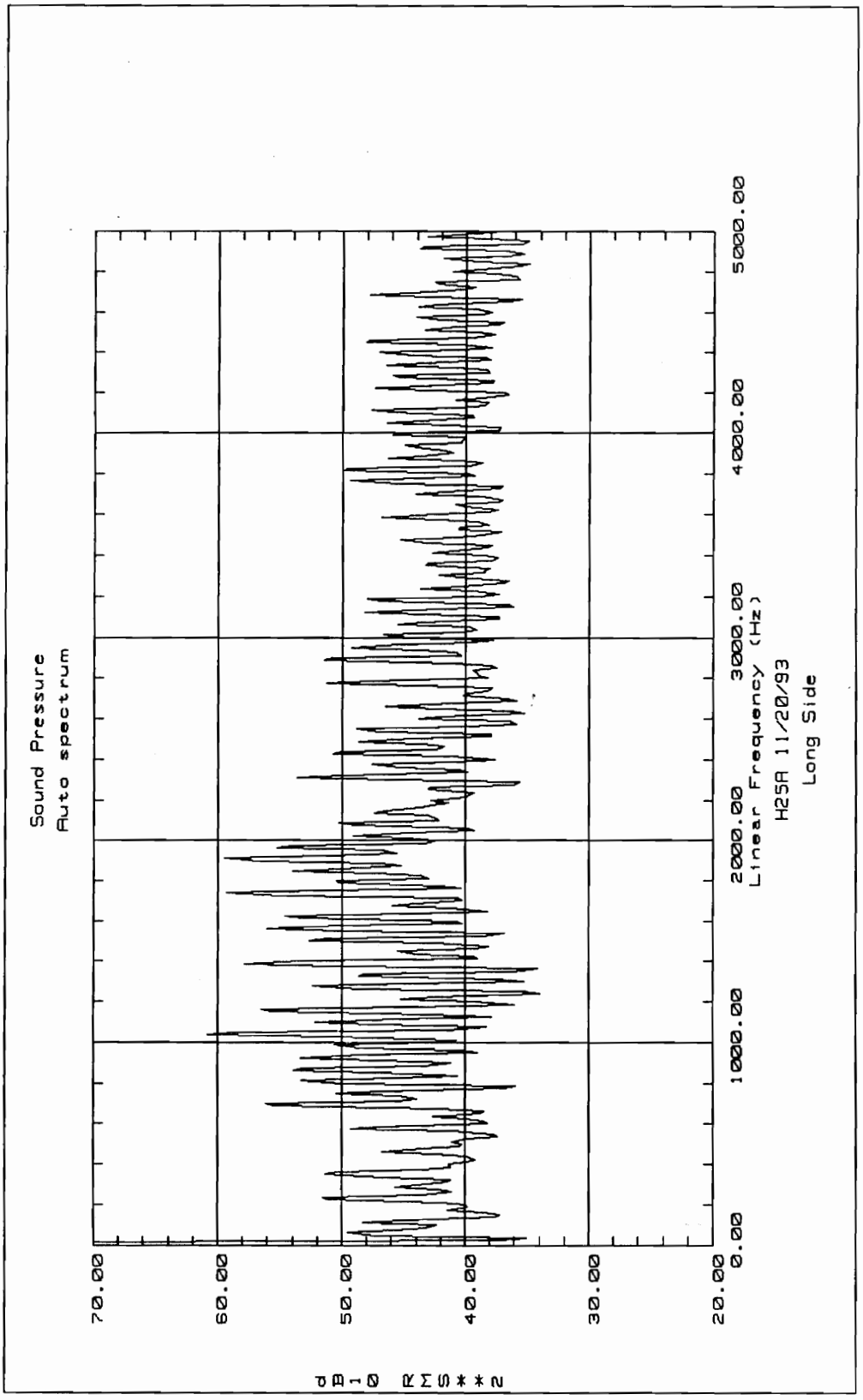

FIGURE A5.1. Compressor Long Side Sound Output Spectrum

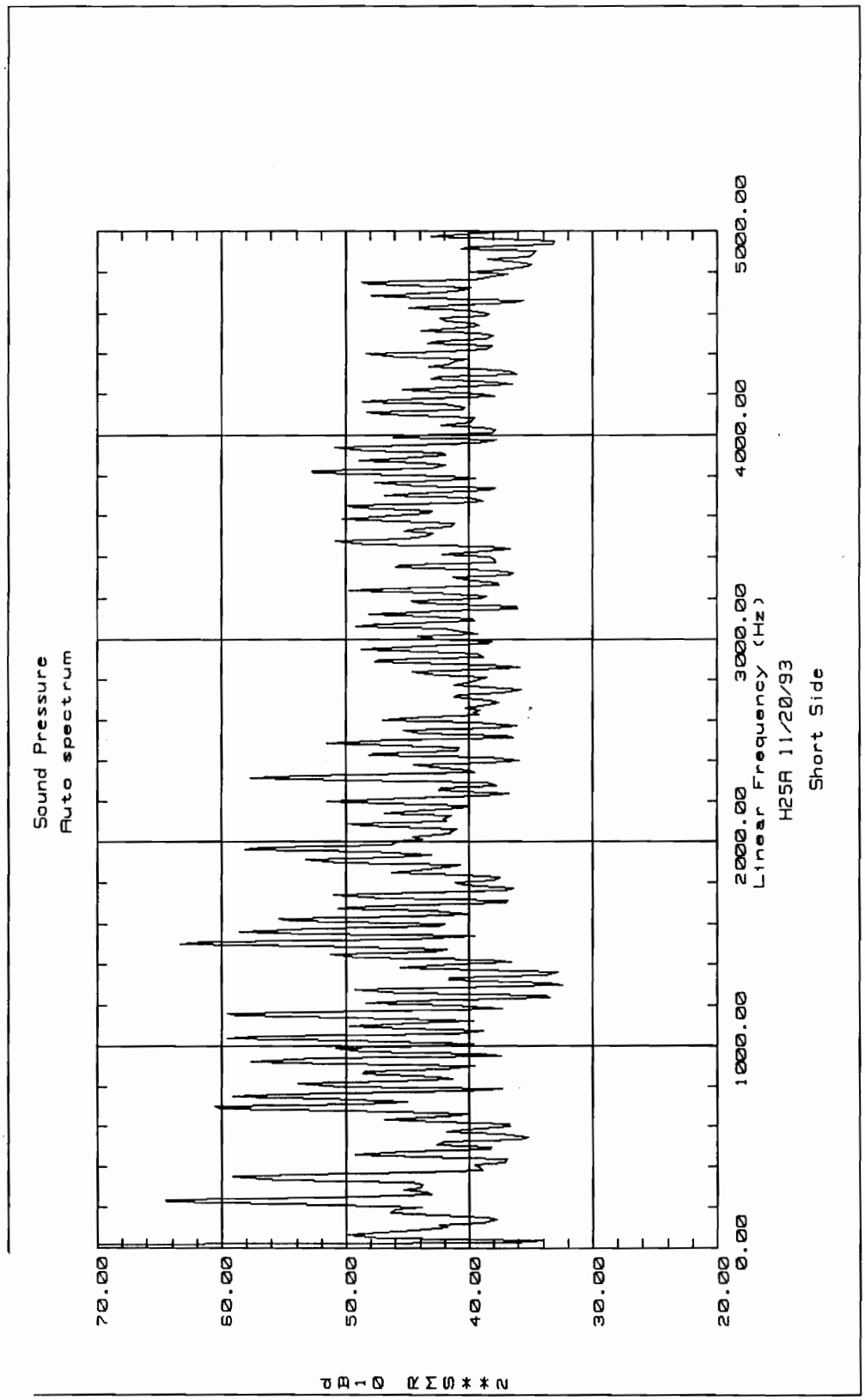

FIGURE A5.2. Compressor Short Side Sound Output Spectrum

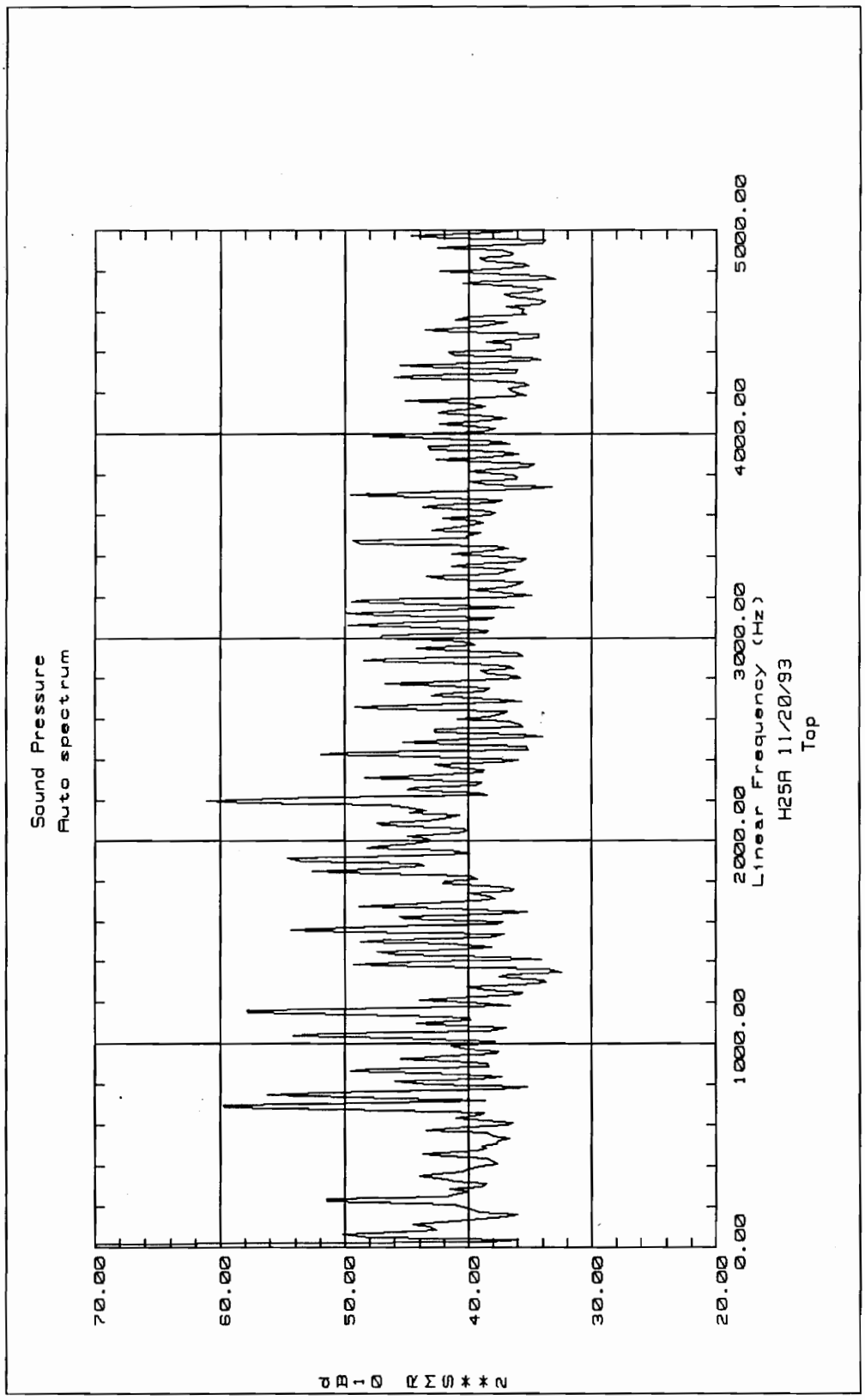

FIGURE A5.3. Compressor Top Sound Output Spectrum

APPENDIX 6.
ORDINARY COHERENCE FUNCTIONS BETWEEN MODEL INPUTS

The following figures illustrate the level of ordinary coherence present in the inputs to the MISO model used to predict the sound output of the H25A compressor. These supplement the examples shown in Fig. 5.10.

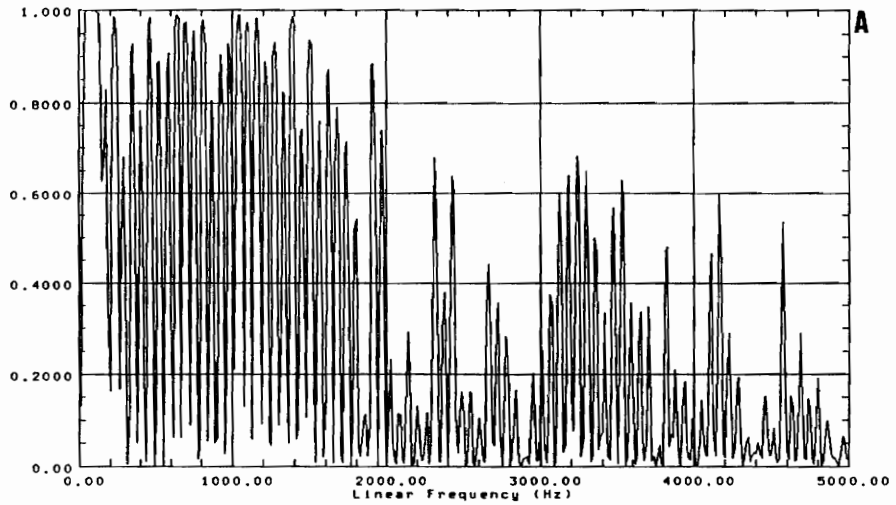

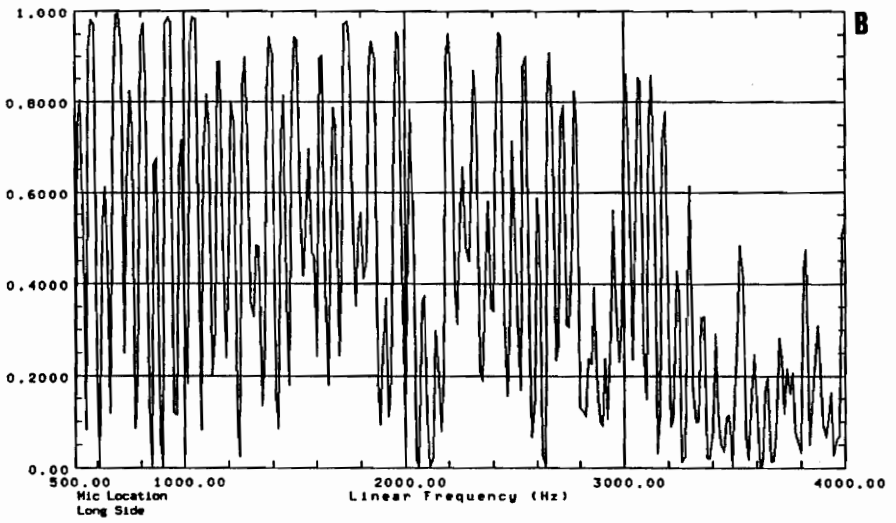

FIGURE A6.1. Ordinary Coherence Between Inputs (a) Left Spring X-Axis and Bottom Cylinder Pressure (b) Housing and Suction Pressure

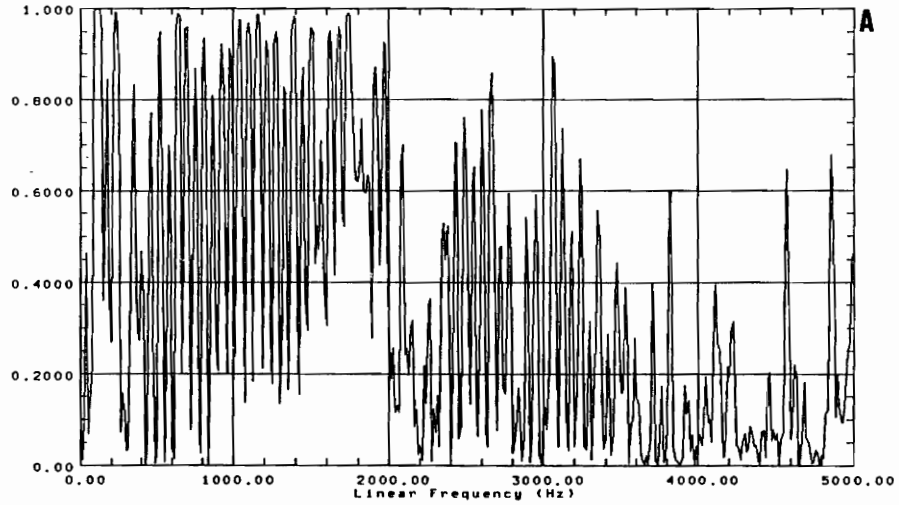

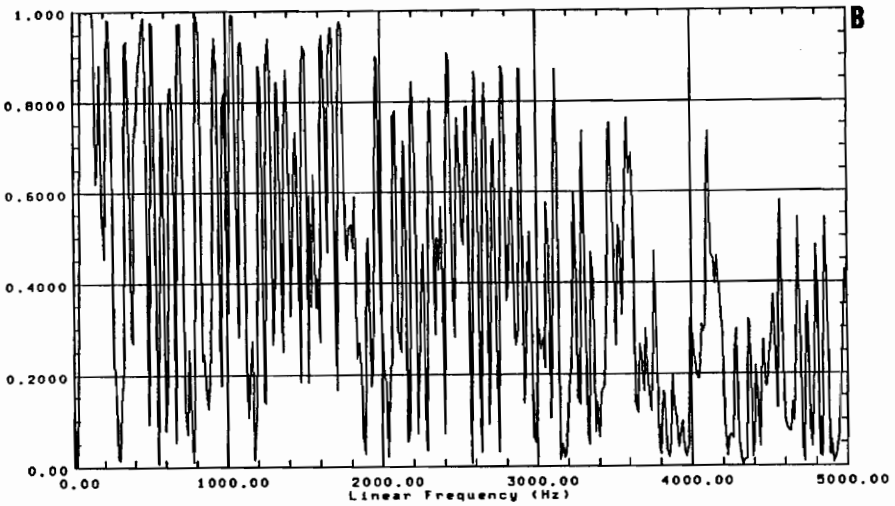

FIGURE A6.2. Ordinary Coherence Between Inputs (a) Left Spring X-Axis and Shock-Loop Accelerometer (b) Left Spring X-Axis and Right Spring X-Axis

APPENDIX 7.
RESULTS OF MISO MODELS: SPRING VS. PRESSURE TRANSMISSION PATH

The following figures supplement the examples of MISO results presented in Figs. 5.14 and 5.15, which presented results comparing the contributions of the spring transmission path and the pressure transmission path to the far-field sound output. Presented here are the same results from the compressor long side, compressor short side, and compressor top sound spectra. The plots display sound pressure level in un-weighted dB re 2.9 x 10^{-9} psi (20 x 10^{-6} Pa).

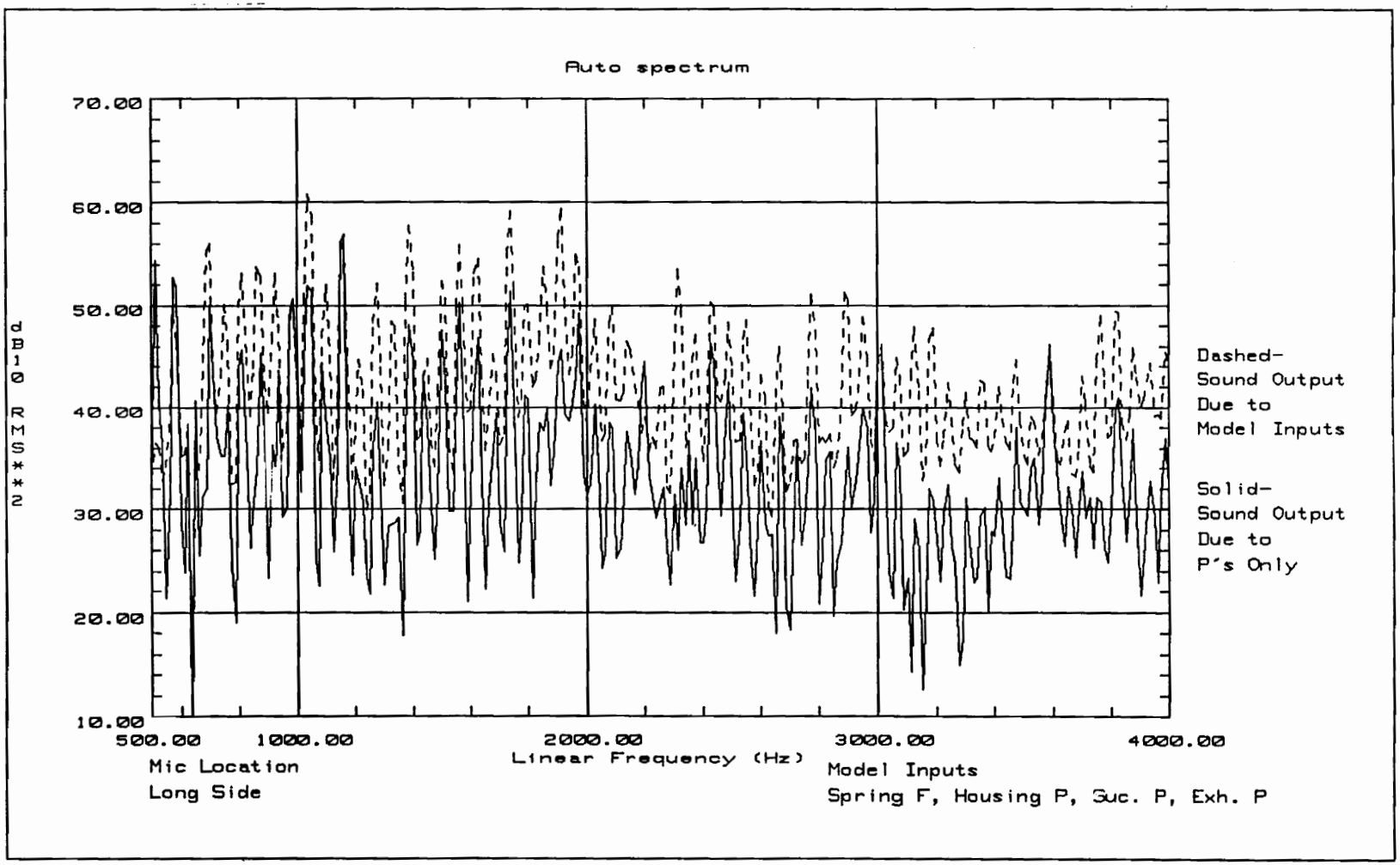

FIGURE A7.1. Prediction of Long Side Sound Output Due to Pressure Fluctuations

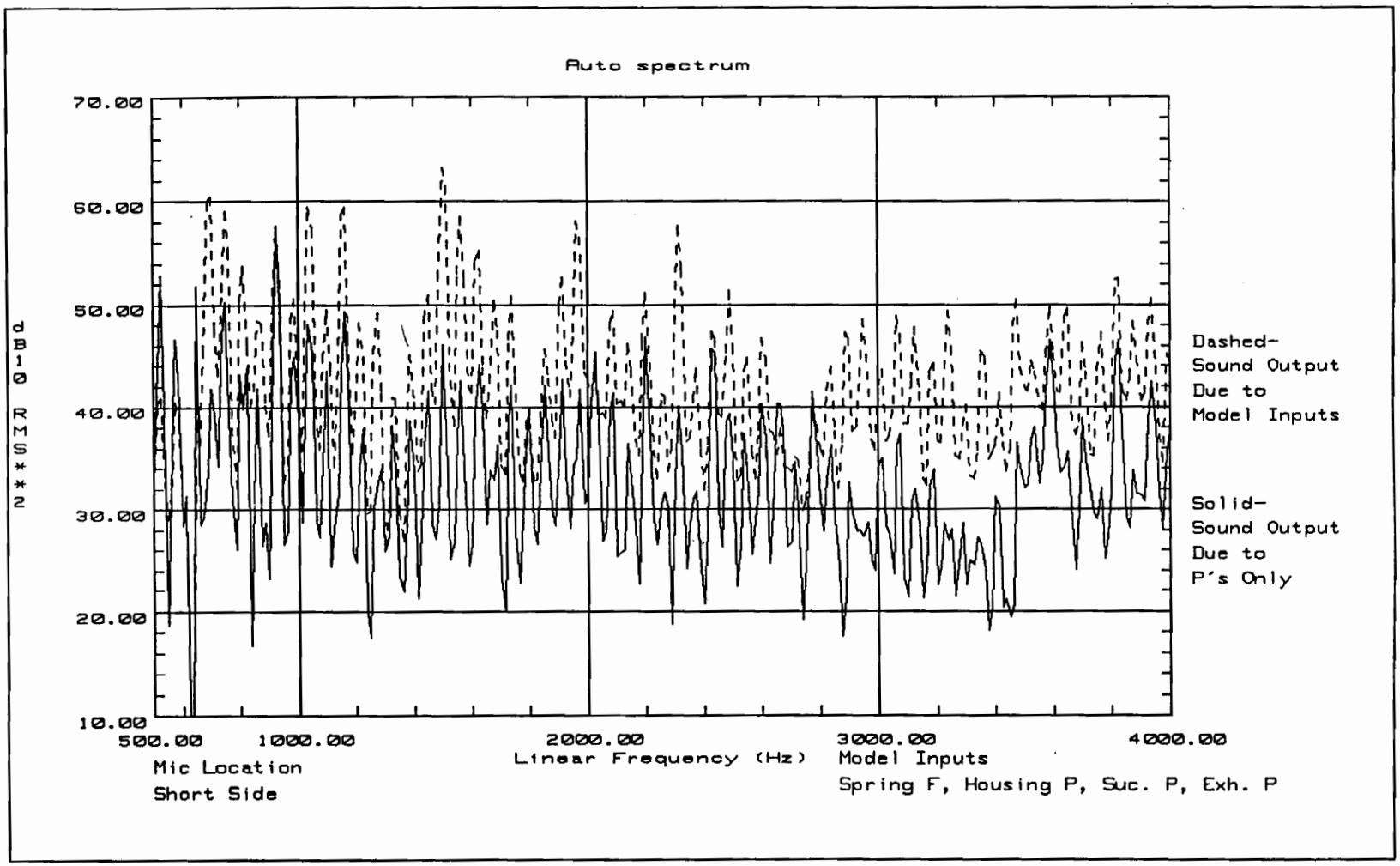

FIGURE A7.2. Prediction of Short Side Sound Output Due to Pressure Fluctuations

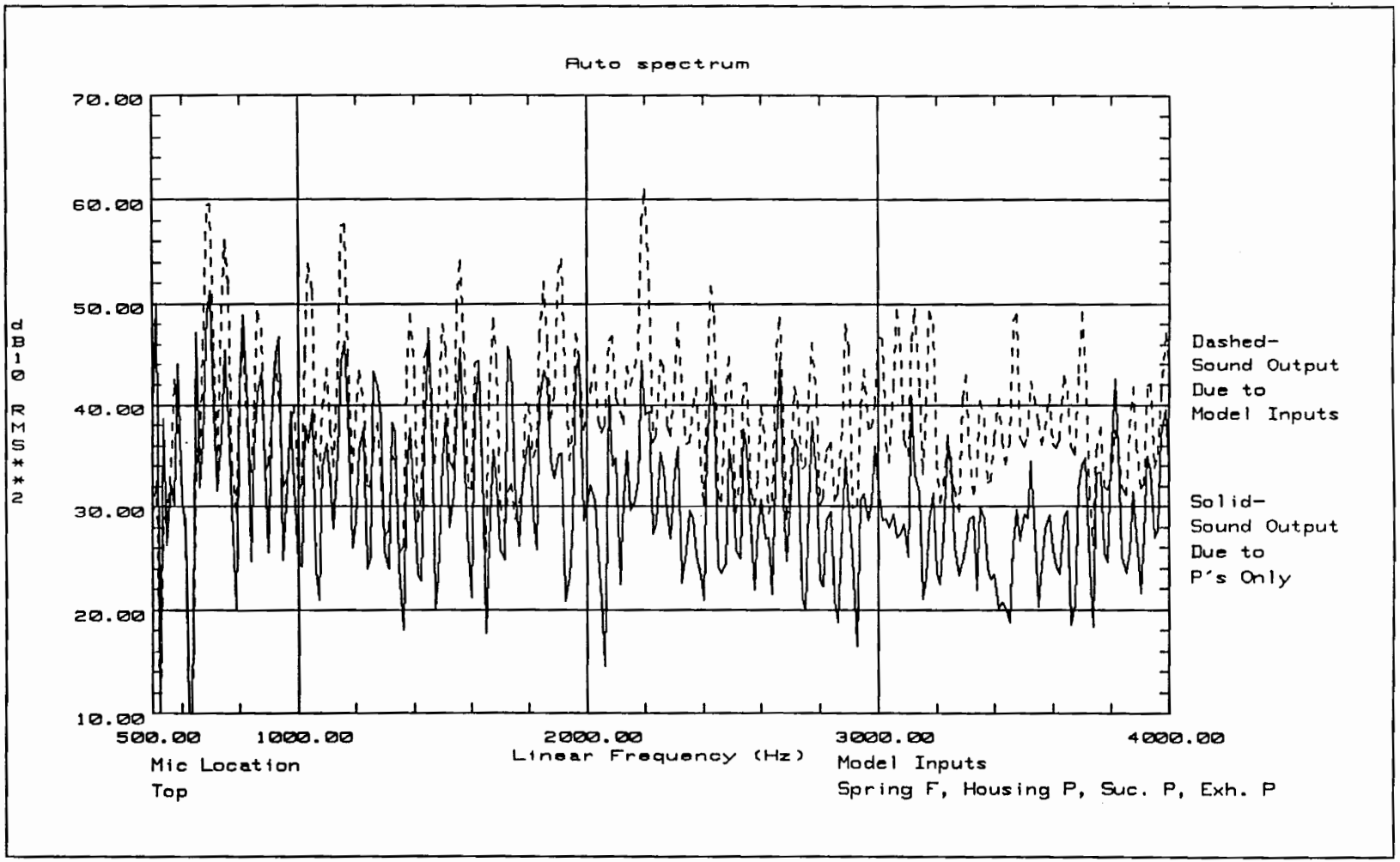

FIGURE A7.3. Prediction of Top Sound Output Due to Pressure Fluctuations

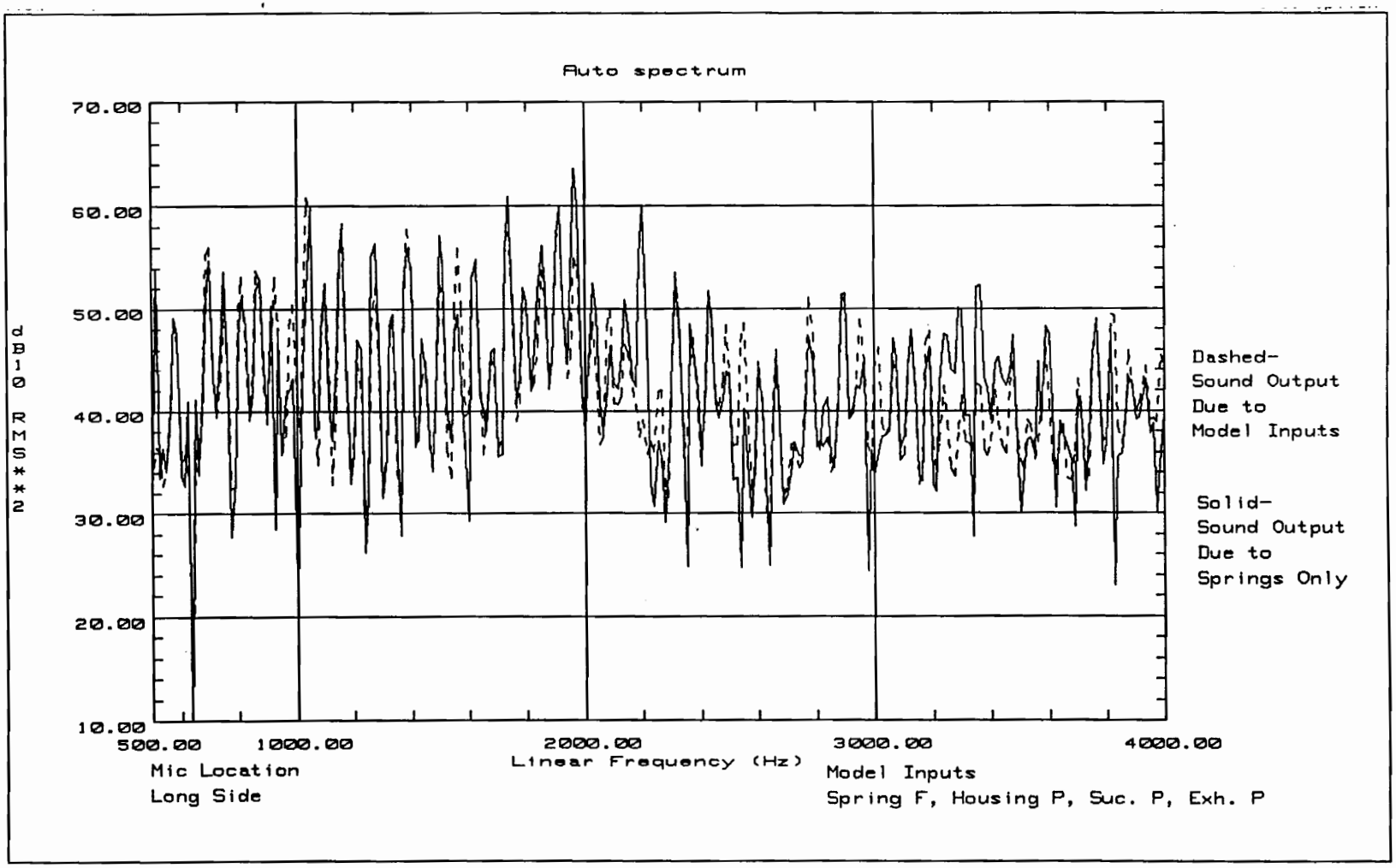

FIGURE A7.4. Prediction of Long Side Sound Output Due to Spring Forces

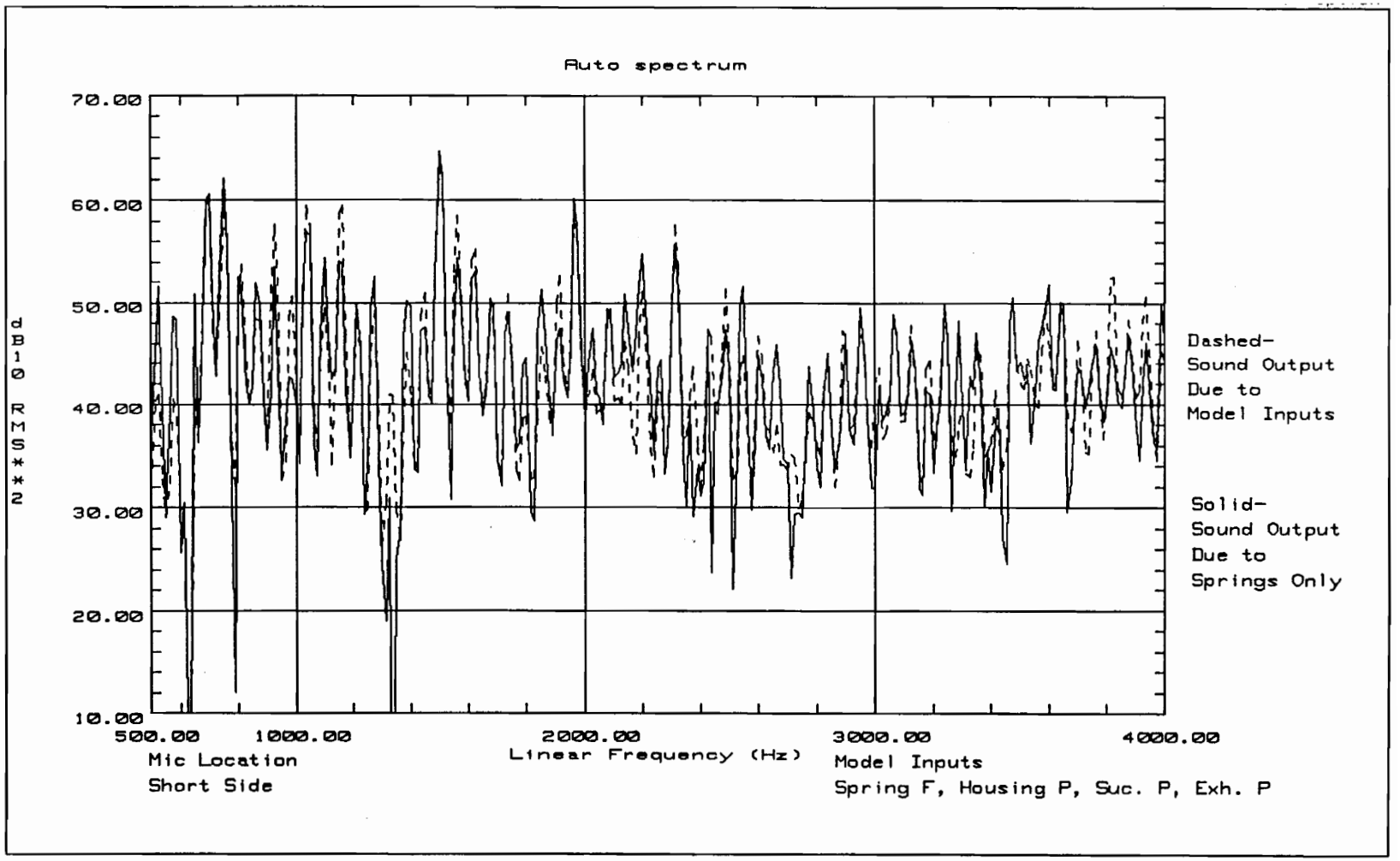

FIGURE A7.5. Prediction of Short Side Sound Output Due to Spring Forces

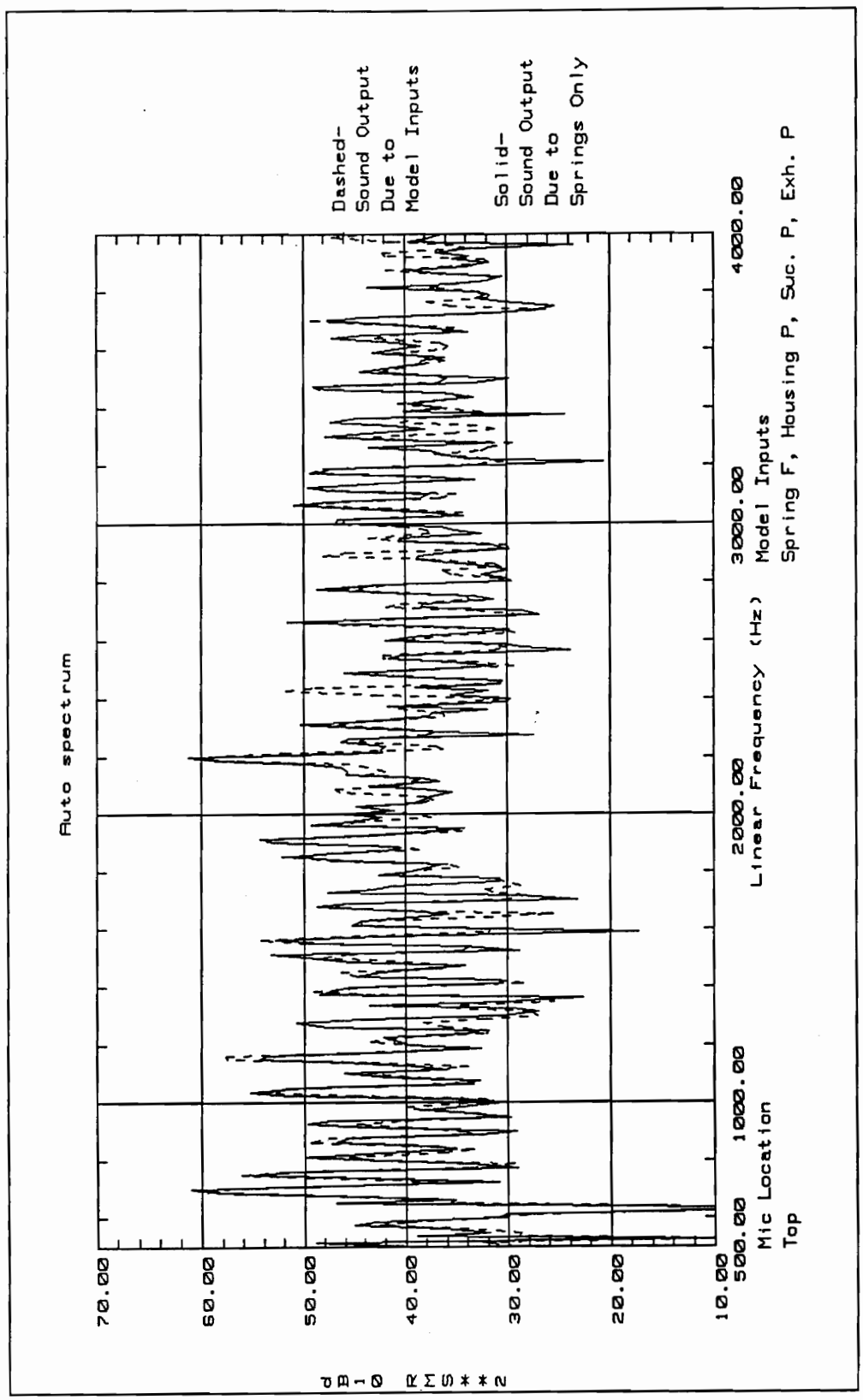

FIGURE A7.6. Prediction of Top Sound Output Due to Spring Forces

APPENDIX 8.
RESULTS OF MISO MODELS: TOP SPRING VERSUS SIDE SPRING TRANSMISSION PATH

The following plots present the results of models predicting the contribution of the top stabilizer spring transmission path and the right suspension spring transmission path. A discussion of these results is presented in section 5.4. The plots display sound pressure level in un-weighted dB re 2.9 x 10^{-9} psi (20 x 10^{-6} Pa).

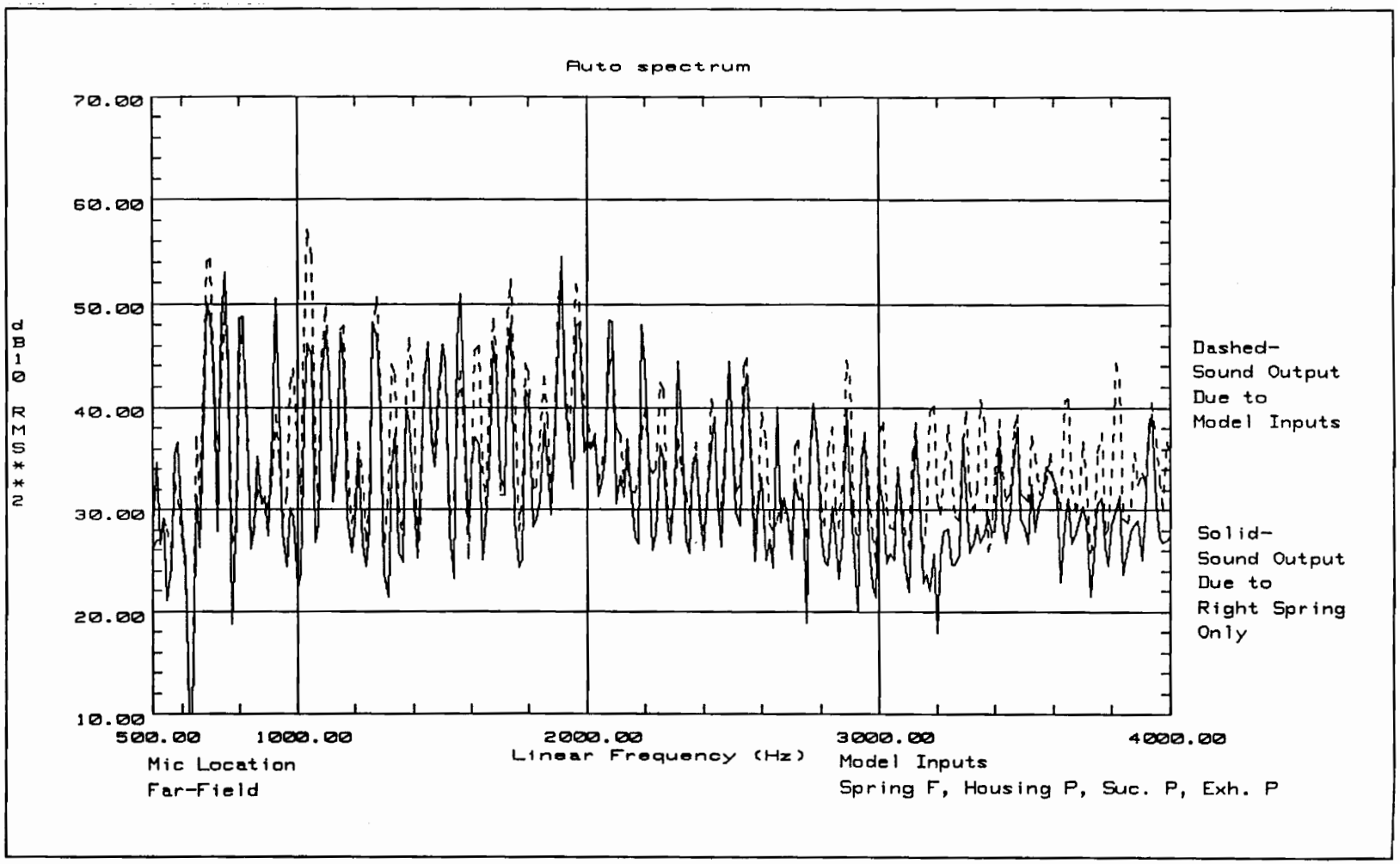

FIGURE A8.1. Prediction of Far-Field Sound Output Due to Right Spring

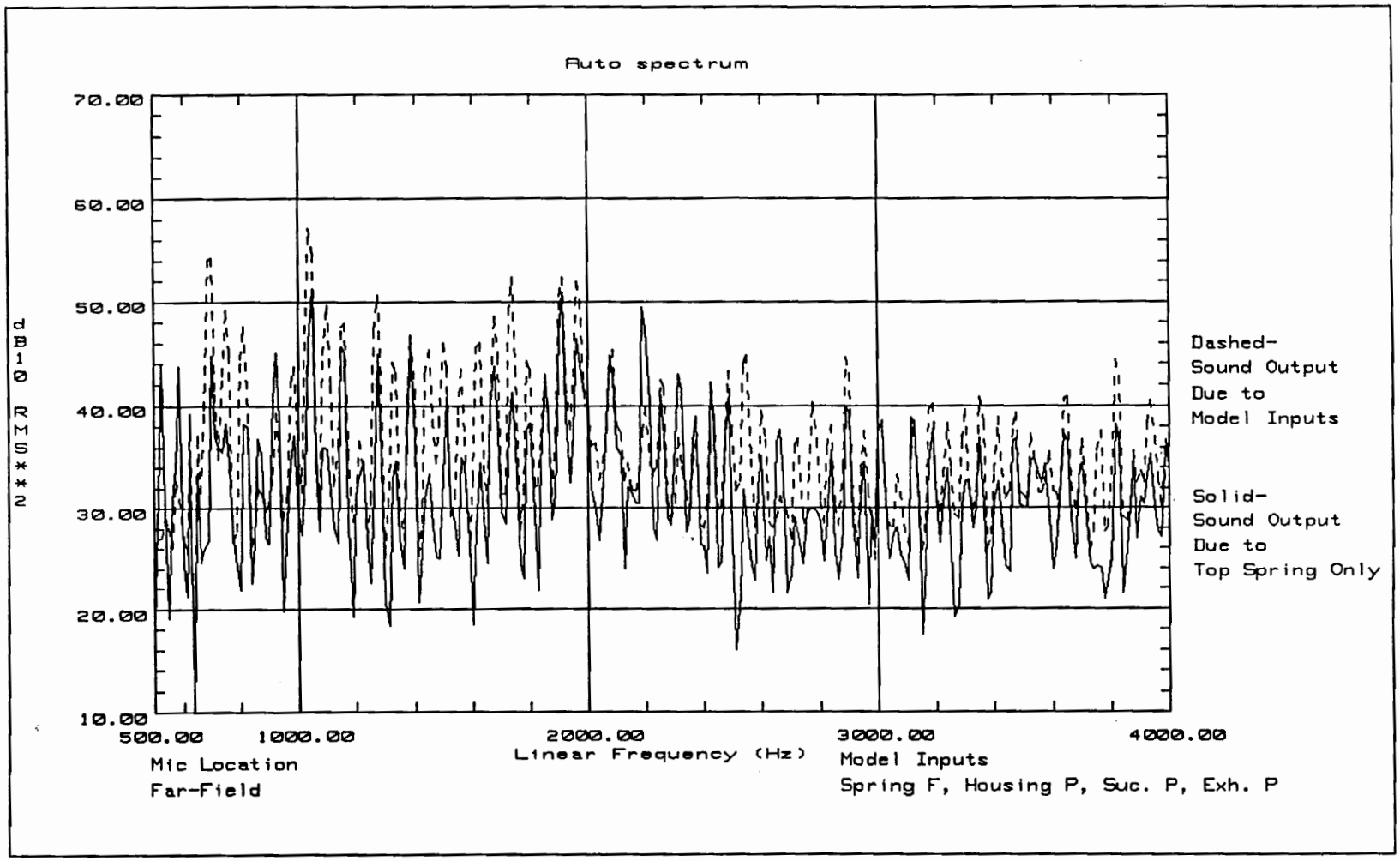

FIGURE A8.2. Prediction of Far-Field Sound Output Due to Top Spring

VITA

Matthew Craun was born in Radford, Virginia on February 27, 1970 and was raised in and around Cincinnati, Ohio. After graduating from Walnut Hills High School in Cincinnati, where Matthew received a National Merit Scholarship award, he attended the University of Cincinnati on the University Honors Scholarship and Karl Kiefer Scholarship. While attending the University of Cincinnati, Matthew worked as a co-op engineering student at Pratt & Whitney Government Engines and Space Propulsion facility in West Palm Beach, Florida. Matthew graduated Magna Cum Laude from the University of Cincinnati in 1992, and subsequently enrolled as a master's student at Virginia Polytechnic Institute and State University, where he is currently awaiting the completion of his master's requirements.

Matthew is a member of the Tau Beta Pi engineering honor society and the Pi Tau Sigma mechanical engineering honor society. He is currently an Engineer in Training in the state of Ohio.